UNIVERSITY OF SOUTHAMPTON

The Impact of the Galápagos Islands on the Dynamics of the Equatorial East Pacific

Stuart James Brentnall

Submitted for the degree of Doctor of Philosophy

School of Ocean and Earth Sciences

September 1999

UNIVERSITY OF SOUTHAMPTON

ABSTRACT

FACULTY OF SCIENCE
OCEAN AND EARTH SCIENCES

Doctor of Philosophy

THE IMPACT OF THE GALÁPAGOS ISLANDS ON THE DYNAMICS OF THE EQUATORIAL EAST PACIFIC

by

Stuart James Brentnall

Small changes in the sea-surface temperature (SST) distribution in the equatorial Pacific are known to have large consequences for the weather and climate on regional and even global scales. A detailed knowledge of the SST patterns is therefore necessary if we are to understand and predict these effects thoroughly. Effort has hitherto been concentrated on understanding the dynamics of the West Pacific Warm Pool, but attention is now shifting to the eastern Cold Tongue region. This thesis contributes to this programme by assessing the impact of one unique feature of the equatorial East Pacific; the presence on the equator of a medium-sized island group – the Galápagos Archipelago.

The project is carried through using a combination of: in situ oceanographic data from ships and moorings; satellite SST and colour images; and diagnostics from both a sophisticated ocean general circulation model and a simplified (reduced gravity) model. Each model was run both with and without a representation of the Galápagos.

It is found that under typical conditions the islands form the eastern boundary of the cold tongue; the lowest equatorial SSTs in the Pacific occur on the west coast of the main islands of the group. As well as preventing the cold tongue from extending any further east, the islands also cool the sea surface still further for a distance of some 1000 km to the west. For the first 100 km or so the cooling is of the order of 1°C; on the larger scale it is more like 0.1°C.

This cooling is a result of hydraulically enhanced upwelling of waters from the Equatorial Undercurrent (EUC), which is best explained by a Bernoulli-type (non-rotating, non-linear) theory. This theory also predicts that water parcels in the EUC will undergo vertical excursions on their passage around the north and south coasts of the islands; these excursions are observed in at least one numerical model. Downstream of the archipelago the EUC usually reunites and executes inertial oscillations, meandering about the equator. Transport in the EUC is also reduced because of the presence of the islands, by 30–50% to the east of the islands and by up to 20% to the west.

Enhanced SST variability north and south of the equator immediately to the west of the Galápagos indicates that tropical instability waves (TIWs) are more active here than they would be were the islands absent. This is due to a pair of barotropically unstable zonal jets originating at the northern and southern tips of the islands. These jets are consistent with the theory of low-frequency flow past equatorial islands on the beta plane (which predicts that the South Equatorial Current will split into two such jets on encountering such an island), although weaker jets are found in models with no representation of the Galápagos. As with the cold tongue, the islands form the eastern limit of the region where these jets are found.

Contents

List of Figures

List of Tables

Acknowledgements

This project was enabled by a grant from the UK Universities' Global Atmospheric Modelling Programme (UGAMP), under Alan O'Neill, supplemented by a CASE award from the James Rennell Division of the SOC. I was advised and encouraged by my supervisors, Kelvin Richards and David Webb.

Data and code converged on my PC from many different directions. The IRONEX data were supplied by Curtis Collins of the Naval Postgraduate School in Monterey. TAO mooring data and CZCS images are freely available over the web, and are released by the TAO Project Office and NASA's Goddard DAAC, respectively. Satellite SST data were provided by the JRD Satellite Team; Helen Snaith was particularly helpful. The project would obviously not have been possible without the results from the two integrations of OCCAM. The entire OCCAM team dealt patiently and effectively with my enquiries over the years, and I am grateful to them. Jay McCreary, now at SOEST in Hawaii, kindly let me have a copy of the source code for his $2\frac{1}{2}$-layer model.

Harry Bryden pointed me in the direction of some crucial references, reminded me not to forget about the EUC, and arranged for me to participate in the 1996 ACCE cruise of *R/V Knorr* which showed me what the "real" ocean looks like and made for one of the more enjoyable five weeks of the PhD.

The path of the research student is long and can be lonely. I'd never have made it without the company of my friends Simon Keogh and Steve Spall along part of the way. People at the salsa and at the session also contributed more to my well-being than they probably realise. Love and thanks to all of these.

Chapter 1

Introduction

1.1 Motivation

Small changes in tropical Pacific sea surface temperature (SST), not to mention the larger changes associated with the ENSO (see below) have profound implications for the weather and climate of the whole earth. This has been known at least since the seminal paper of Palmer and Mansfield (1984), who generated large anomalies in the mid-latitude atmospheric long waves associated with weather when they forced an atmospheric general circulation model (GCM) with SSTs that differed only slightly from those used in their control experiment (specifically by being about 1°C warmer in the western and 1°C cooler in the eastern equatorial Pacific). A detailed knowledge of equatorial SSTs and their patterns is thus crucial to the understanding of the global weather and climate. In particular, it is vital that the oceanic component of coupled models simulates the SST field correctly, in detail, in this region. Scientific programmes such as the recently-completed TOGA have hitherto focussed on understanding the detailed physics of the Warm Pool of the equatorial West Pacific, but the importance of the East Pacific is increasingly being recognised, for instance in the setting up of the EPIC[1] programme scheduled for the years 1998–2004. The purpose of this thesis is to assess the importance of one unique property of the East Pacific—the presence on the equator of a medium-sized island group, at or below the limit of resolution of most of the models used for operational forecasting or climatological

[1] Eastern Pacific Investigation of Climate.

research.

The surface of the sea in the equatorial East Pacific is markedly cooler than in the western equatorial Pacific, by about 5°C in the annual average and by more than 10°C at times. This temperature contrast both drives and is maintained by the Walker Circulation, a large-scale atmospheric circulation in the vertical/zonal plane above the equatorial Pacific connecting a region of ascent over the western Warm Pool to a region of descent over the eastern Cold Tongue by means of surface easterlies and westerlies aloft. Aperiodic disruption of this pattern—the El Niño/Southern Oscillation or ENSO—has a severe impact on the biology of the equatorial East Pacific and on the weather over a much larger area, possibly the whole globe. In general terms this coupled system is quite well understood, but many details remain to be filled in.

One aspect of the system which has received relatively little attention is the effect of the topography of the Galápagos Islands on the nearby oceanic flows and possible larger-scale consequences thereof. It has long been known that the islands have no significant effect on the large-scale oceanic Rossby and Kelvin waves that are believed to play a crucial role in the ENSO (see *e.g.* Cane and du Penhoat (1982)), but output from OCCAM, a high resolution global ocean GCM suggests that the islands do have a measurable impact on some other major features. Firstly, the tongue of cold water that lies along the equator seems at times to be enhanced for several hundred kilometres to the west of the islands. Secondly, the presence of the archipelago appears to generate two zonal (westward) jets, beginning at the northern and southern tips of the islands, in the top few tens of metres of the ocean. These jets are barotropically unstable and may thereby help to stimulate the growth of Tropical Instability Waves[2] (TIWs), two streets of large eddies to the north and south of the equator which are known to be important in mixing the cold tongue waters away from the equator (equatorward heat fluxes of around 180 W m^{-2} due to the waves have been reported (*Hansen and Paul*, 1984; *Bryden and Brady*, 1985; *Halpern*, 1987)).

The purpose of this thesis is to examine these possibilities in greater depth; to

[2]Also known, after their discoverer (*Legeckis*, 1977), as "Legeckis waves" or "Legeckis eddies"; or, occasionally, as "equatorial long waves", though I feel this is rather inappropriate as there are other, longer, waves in the equatorial oceans.

attempt to verify that the modelled phenomena are real, and to assess the magnitude of any effects that the Galápagos might have on the temperatures and currents of the equatorial East Pacific. This is of more than purely academic interest. Most of the models currently used to predict El Niño contain no representation of the Galápagos. If the islands were having a measurable effect then there would be a strong case for incorporating them into these models.

A synergetic approach is adopted; the hypotheses are tested and impacts assessed using a combination of GCMs, simplified or "process-oriented" numerical models, existing theory, satellite observations and *in situ* observations from both moored buoys and research vessels.

1.2 Background

A glance at any map of the world ocean shows that the Galápagos Archipelago occupies a unique position. It is the only medium-sized open ocean island group that lies astride the equator, where "medium-sized" means "having dimensions of the order of a Rossby radius". Low-order baroclinic equatorial Rossby radii are typically two or three hundred kilometres (*Philander*, 1990, page 163). Other equatorial land masses are either much smaller than this (*e.g.* Gan, St Peter and St Paul Rock), or much larger (Sumatra, Borneo, Africa, South America or, at depth, the Maldives), or they are not as isolated as the Galápagos.

In the first case (small islands) the effect of the islands on the flow might be expected to be essentially the same as if the Earth were not rotating, with, for instance, flow separation occurring at some critical Reynolds number (Re) and vortex streets being shed at higher Re, at a frequency determined by the Strouhal number for that Re (*Tritton*, 1988, pages 27–8). Such behaviour has indeed been observed in the wakes of small islands at low latitudes (*Barkley*, 1972; *Heywood et al.*, 1990; *Heywood et al.*, 1996). In fact similar flows have also been observed at higher latitudes (*Salusti and Santoleri*, 1984; *Pattiarachi et al.*, 1987, etc.), although these are more likely to be modified by rotational effects—Rossby radii are smaller at mid-latitudes, typically of order a few tens of kilometres for the gravest baroclinic mode (*Gill*, 1982). Flow

separation is inhibited on the left-hand side of the island (looking downstream in the northern hemisphere) because of the inward Coriolis force, and conversely, with the result that the right-hand attached eddy is larger than the left-hand one, and detaches at a lower Re.

In the second case (large islands or continents) there are also unequivocally "planetary-scale" effects. Rossby and Kelvin waves can be totally or partially reflected or deflected (*Cane and du Penhoat*, 1982; *Clarke*, 1991), and (another side of the same coin) the land masses can be sufficiently western-boundary-like for Godfrey's Island Rule (*Godfrey*, 1989) or variants thereon to be useful in estimating nearby currents; this crops up a lot in recent discussions of the Indonesian Throughflow (*Godfrey*, 1996; *Wajsowicz*, 1993; *Yamagata et al.*, 1996, etc.).

As mentioned above, the Galápagos are of intermediate size. It is about 120 km from the northern to the southern tip of the main island, Isabela (see Figure 1.1; one degree of latitude represents a distance of some 111 km).

From Pinta in the north (at 0.6°N) to Española in the south (at 1.3°S), the main island group covers a latitudinal distance of some 200km. The 250m isobath is continuous over a north-south extent of about 150km. (As pointed out by Clarke (1991), it is the north-south extent of continuous isobaths that is important to the low-frequency dynamics, and not their shape, essentially because low-frequency equatorial motions tend to have such large zonal extents that any islands will appear to them as thin barriers oriented north-south. For instance, a typical first baroclinic mode Kelvin wave with a period of one month has a (zonal) wavelength of about 7000km.) Thus the flow around the Galápagos may be expected to have characteristics of both rotating and non-rotating flow.

An example of this is furnished by White (1971a; 1971b; 1973), who observed meanders in the Equatorial Undercurrent (EUC) downstream (to the east) of the Galápagos but was unable to decide whether these represented a compound Kármán wake or a train of stationary lee Rossby waves; his scale analysis was consistent with both hypotheses. His data were quasi-synoptic. Sequential data would have enabled the stationary topographic wave, which would depend for its existence on the Earth's

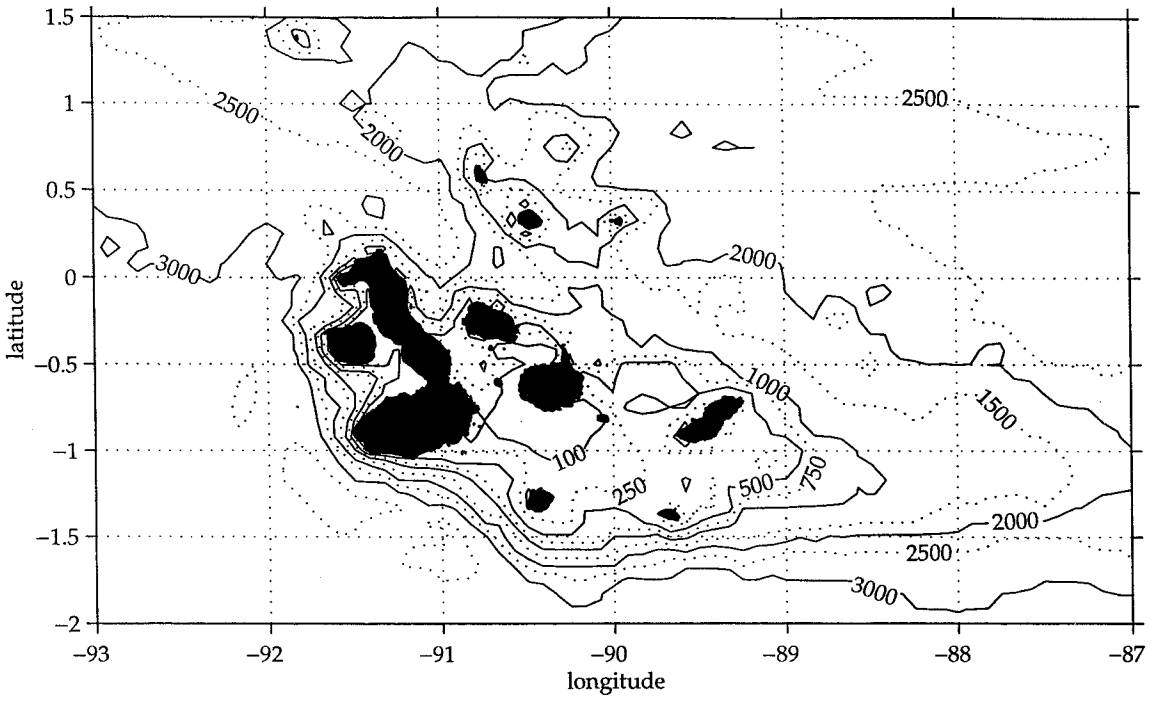

Figure 1.1: Galápagos bathymetry in metres (NGDC gridpoint data).

rotation, to be distinguished from the non-stationary wake, which would not. Note, however, that Hendry and Wunsch (1973), amongst others, deprecate at least the use of the "Kármán wake" terminology here, on the grounds that a vortex street is essentially a two-dimensional phenomenon, whereas his and their EUC wakes are strictly three-dimensional.

As another example, Yoon (1981) found the Galápagos (and other equatorial islands) to be relatively transparent to eastward-propagating Kelvin waves but opaque to westward-propagating long Rossby waves. The former were able to creep around the islands in coastally trapped form, a mode of propagation not available to the latter. Some of Yoon's findings have, however, been disputed (*Cane and du Penhoat*, 1982); as noted above and exemplified later in the thesis (see section 3.4 and Appendix B), Rossby waves seem in fact also to be largely unaffected by islands of this size.

A third example will be provided by the work reported here. On the one hand,

the cold tongue enhancement will be seen to be due essentially to hydraulic effects as the EUC strikes the islands. Such behaviour was observed by Hendry and Wunsch at a much smaller equatorial island[3] and is therefore not necessarily a rotational effect. On the other hand, it appears that the near-surface oceanic wake of the Galápagos is characterised by the two island tip jets referred to earlier (at all times in OCCAM, and at certain times in the real ocean). Whatever the explanation for these jets, they are sufficiently different from any of the wake patterns observed in flows past obstacles in non-rotating frames (*Tritton*, 1988, pages 21–34) for us to be sure that the Earth's rotation plays a part in their production.

1.3 Aims

The specific questions to be addressed are as follows.

First, what is the cause of the low SSTs to the west of the islands? It has entered the folklore of Galápagos oceanography that the cold patch is due to an upwelling that results when the EUC impinges on the islands (*Smith and Whitehead*, 1993; *Whitehead et al.*, 1989, etc.), and indeed it is quite intuitive that when the EUC strikes the Galápagos its waters will pile up against the topography, with upwelling above the EUC core (in the sense of upward displacement of isopycnals), downwelling below the core, and a blunting of the thermocline. But, for one thing, the details of this are not so simple; why or when, for example, does convergence of the EUC win out over a potential-like flow *around* the islands? This presumably depends on the stratification of the water. And, for another thing, there are other possible causes, such as a wake effect of the surface South Equatorial Current (SEC) which normally flows *west*wards around the Galápagos, or wind patterns modified locally by the presence of the islands[4].

A second question is: How far does the cold patch spread? Snapshots of near-surface temperature from OCCAM, such as that shown in Figure 1.2, and animations

[3] Jarvis Island (0°23′ S, 160°00′ W), which is some 2km in north-south extent.

[4] Such an explanation was considered for an oceanic wake behind Hawaii by Patzert (1969) (*Patzert*, 1969), though he considered the effect of a ravine wind between two islands on oceanic lee eddies.

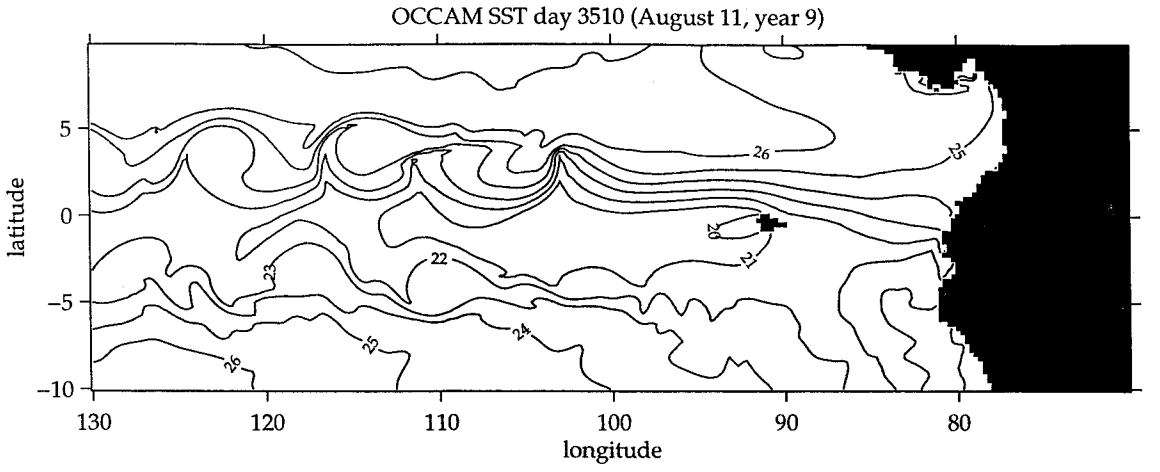

Figure 1.2: "Surface" temperature (actually at 10m depth) on day 3510 of the main run of OCCAM (11th August year 9). Contour interval 1°C.

of the same, suggest that at its peak the influence of the Galápagos is felt for many hundreds of kilometres to the west, constituting a significant enhancement to the Pacific cold tongue. Further diagnostics can be found in Chapter 3, and attempts to find similar features in historical and satellite observations are presented in Chapter 2.

Even if there *are* SST patterns suggestive of medium or large scale effects of the Galápagos topography, this does not prove that the topography is responsible for these patterns. There is a very strong tendency for easterly (westward) winds on the equator to produce Ekman divergence and hence upwelling, and hence a cold tongue in regions where there is a sharp vertical temperature gradient near the surface; so the contribution of the wind to the SST patterns needs to be separated out. Attempts to do this with observations and with OCCAM data appear in Chapters 2 and 3 respectively, and the influence of different wind patterns when the islands are or are not present is examined in Chapter 4.

Fourthly, what of the seasonality of the phenomenon? How and why does the cold patch spread westwards? Is it simply a westward extension of the Ekman upwelling region with the onset of the easterly winds, or do these winds cause westward advection of cold waters upwelled near the islands? Another possibility is that a localised increase in strength and thickness of the EUC core, identified in the historical record as striking the Galápagos each year shortly before the cold patch starts to ex-

tend (*Wyrtki*, 1964; *Lukas*, 1986), stimulates the growth. Lukas tentatively identifies this pulse as a Kelvin wave packet, although the precise nature thereof is somewhat obscure. This point is considered further in Chapter 2, where more recent *in situ* observational data are also examined for evidence of such wave packets.

The fifth and final question regarding the putative enhancement of the cold tongue is: How does it relate to the equatorial Pacific as a *coupled* system? If there really is a significant enhancement, the enhanced zonal temperature contrast can be expected to strengthen the Walker Cell (page 2). The enhanced surface easterlies would in turn make the cold tongue still colder; that is, the effect of the Galápagos would be to make the positive feedback mechanism of Bjerknes (1969), which plays the role of amplifier in all simple conceptual models of El Niño (*Jin*, 1996, and refs.), stronger than it would be in their absence. Furthermore, impulsively enhanced westerlies on the western flank of the convective region in the western Pacific, at the other end of the Walker Cell, can be expected to drive Kelvin waves. To a first approximation, a first baroclinic mode wave with downwelling of the thermocline is produced (*McPhaden et al.*, 1988), and this may lead to positive SST anomalies in the east Pacific, *i.e.* a damping down of the cold tongue, a month or two later, thus completing a coupled cycle[5]. Short of running a coupled ocean-atmosphere model of the entire Pacific with and without the Galápagos, it would be difficult to gauge this effect. However, the numerical experiments presented in Chapter 4 will indicate the magnitude of the uncoupled dynamical effect of the islands and hence the plausibility of the mechanism.

In view of the island-tip jets not having been remarked as such before, the goals of the study with respect to them are simpler: to verify their existence and to attempt to elucidate the conditions under which they may be produced; and to assess their possible impact on the formation of TIWs.

[5]This is reminiscent of the "delayed oscillator" mechanism for El Niño (*Battisti*, 1988; *Suarez and Schopf*, 1988; *Schopf and Suarez*, 1988), which however places more emphasis on *upwelling* Kelvin waves produced when upwelling Rossby waves due to the increased wind are reflected at the western boundary of the Pacific. The upwelling Kelvin waves reduce the SST and thereby help to bring an El Niño episode to an end.

In short, the core aim of this study is to identify and quantify the effects of the Galápagos on the dynamics and thermodynamics of the near-surface waters of the equatorial East Pacific, with particular reference to:

- effects on the values and spatial distribution of surface temperature in the equatorial cold tongue;
- the fate of the Equatorial Undercurrent; and
- the division of the South Equatorial Current into two branches at about the longitude of the islands, and possible consequences for the strength and location of tropical instability waves.

These aims are achieved using a variety of different methods, as reflected in the structure of the rest of the thesis. Chapter 2 presents the satellite and observational data that I have collated, together with a review of the relevant observational literature. Chapter 3 contains diagnostics from the main run of OCCAM. Chapter 4 reports on experiments that have been carried out using a simplified (reduced gravity) model of the equatorial Pacific. Data from an integration of OCCAM in which the Galápagos were removed are also analysed here. This structure is not rigid; some of the observational data are reassessed in the light of the model data of Chapter 3, for instance, and existing theory is used to shed light on some of the phenomena at various points. The principal findings of this project are summarised and their significance assessed in the concluding Chapter 5.

Chapter 2

Observations

In this chapter we begin our study of the impact of the Galápagos on the dynamics of the nearby ocean with a survey of relevant observational data from a variety of disparate sources. The emphasis is on seeking evidence that the islands *do* have an impact, but there is also a secondary theme which places the islands in the broader context of equatorial Pacific oceanography.

The historical hydrographic literature reviewed in section 2.1.1 reveals many interesting features but leaves several questions unanswered. The existence of a patch of low SST attached to the western edge of the islands, most probably due to zonal convergence as the EUC runs into the steep topography, is confirmed by upward-sloping isopleths of other hydrographic parameters as the islands are approached from the west. A thickening of the thermostad deeper in the water column also supports this interpretation. This cold patch spreads out to the west at the time of year when the cold tongue is forming, but the observations do not go far enough west to determine the contribution of the islands to this process. A seasonal cycle in the EUC which reflects that in the cold tongue suggests that remote forcing also plays an important role.

Rather sparse observations of the EUC east of the Galápagos present a confused picture of what happens to that current as it passes round the islands. Some light is shed on this issue by a set of ADCP velocity sections obtained at the islands in 1993 and presented in section 2.1.2. These observations show that the portion of the EUC

which is not recirculated into the SEC divides into two branches which pass north and south of the islands, and which seem rapidly to re-unite after passing round the archipelago. In contrast, the SEC divides into two branches but then continues as a pair of zonal jets for at least 200 km to the west.

Evidence for westward propagation of SST signals away from the Galápagos is then sought in the records for the equatorial TAO moorings at 95 and 110°W. An example is presented in which westward propagation is indicated at a speed consistent with an equatorial inertia-gravity wave. Data from these moorings are also used to examine the seasonality of the equatorial waves discerned in the earlier observational literature; a recent classification of westerly wind bursts is also used to test their status as a remotely forced phenomenon. This is part of the context-setting exercise, though an interaction of the waves with the topography may play a role in the seasonal cycle of SSTs to the west of the islands.

A timeseries of ATSR satellite SSTs is then used to assess patterns of SST variability in the eastern equatorial Pacific. The dominant mode is an annual cycle in which the amplitude decreases monotonically away from the Galápagos to both the east and the west. The cold tongue proper terminates abruptly at the islands; low SSTs associated with westward expansion of the region of cold water off the South American coast are clearly shown to be a separate phenomenon. In the final section 2.2.2 data from the CZCS ocean colour instrument are examined. Some of the images from this instrument show two westward streamers originating at the northern and southern tips of the islands. Considering the chlorophyll that gives rise to the colour as a (non-conservative) tracer, this provides further evidence for the two jets revealed by the ADCP data of section 2.1.2.

2.1 *In situ* observations

2.1.1 Historical hydrographic data

Given the intensive interest in the biology of the Galápagos and their surrounding waters, surprisingly little has been published on the small-scale hydrography of the

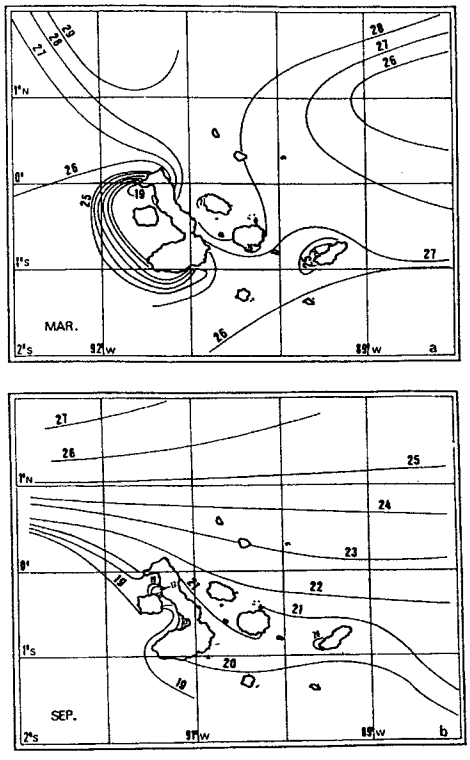

Figure 2.1: Monthly composite charts of surface temperature. Top: March. Bottom: September. From (*Houvenaghel*, 1978).

islands. Houvenaghel (1978) is the only reference that I am aware of which attempts a synopsis of the oceanographic conditions near the islands, including the annual cycle thereof. His "composite" annual cycle is based largely on survey work carried out between September 1967 and September 1968, when ENSO conditions were "normal" in the sense that the SOI (see below, section 2.1.3) was fluctuating about zero. Houvenaghel's composite SST charts for March and September, at the extremes of the annual cycle, are reproduced as Figure 2.1. The March composite shows a cold patch up to 8°C cooler than the surrounding waters, at a time when nearby SSTs are generally at their warmest. During the succeeding months this cold patch spreads out to the south west of the islands; this coincides with the onset of a cold season which is in turn associated with the northward migration of the intertropical convergence zone (ITCZ) in boreal summer, and consequent increase in strength of the south-east trades at the Galápagos. By September the cold waters occupy the whole of the south western part of the area covered by this survey. Transition back to the March pattern is effected mainly by a sudden general warming in December or January.

Houvenaghel's salinity, O_2 and temperature measurements all suggested that the cold patch consisted of EUC waters that had been upwelled (in the sense of vertical displacement of isopycnals) or up-mixed (turbulently). Smaller cold patches to the west of the smaller islands, some of which are apparent in Figure 2.1, suggested that locally the upwelling was topographic and not wind-driven—"local upwelling [is] due to the bottom topography, which introduces an obstacle along the path of the Equatorial Undercurrent [and] results ... in the piling up and rising of the waters upstream from the obstacles with upwelling at the surface" (*ibid.*, page 196).

Several other papers report individual sets of hydrographic and/or direct current measurements both east and west of the Galápagos (*Christensen*, 1971; *Pak and Zaneveld*, 1973; *Hayes et al.*, 1986; *Wilson and Leetmaa*, 1988; *Steger et al.*, 1998). The zonal current sections are discussed in Section 3.4, where they are compared to similar sections output from OCCAM; ADCP data from the IRONEX2 expedition of November 1993 are also presented in section 2.1.2 below. Measurements of other hydrographic parameters are discussed briefly at the end of the present section.

The larger-scale hydrography of the equatorial east Pacific has been more intensively surveyed, particularly during the 1980s—there were relatively few cruises before this, and more recently the satellite and TAO mooring data considered later in this chapter have received more attention. Research ships were particularly active in this region during the period spanning the spectacular El Niño of 1982–1983, so a wide range of typical and atypical conditions was sampled. Bearing in mind the questions raised in Chapter 1, the observations most relevant to the present study are those concerning the EUC, its annual cycle and what happens to it when it strikes or passes round the Galápagos; and those concerning the surface or near-surface conditions.

Lukas (1981; 1986) presents a conspectus of EUC observations in the region to 1975. A thickening of the thermostad (a region of small vertical temperature gradients found below the thermocline in the tropical east Pacific) as the islands are approached from the west he interprets as due to zonal convergence *inter alia* of the EUC as it strikes the topography. Such a convergence or piling up of water was suggested as the most plausible mechanism for the upwelling observed by Houvenaghel, and was also observed upstream of a small equatorial island by Hendry and Wunsch (1973).

Lukas's T-S data also support the idea that EUC waters are recirculated into the SEC. Observations taken during autumn 1982 suggest instead that SEC waters originate in the NECC (*Mangum et al.*, 1986), but this was during the onset of an El Niño and may be atypical.

Several investigators have addressed the question of whether the EUC can be found to the east of the Galápagos, and have come to various different conclusions. Lukas's opinion is that it can, and that it typically passes to the south of the islands, having first been deflected to the south as a result of the southerly (northward) component of the trade winds further west. (In the meridional as well as the zonal momentum equation, the principal balance at the equator is between the wind stress and the pressure gradient, (*Philander*, 1990, section 4.8.2).) When the EUC is strong, Lukas also detects a northern branch that goes along the equator and eventually forms or enhances the Peru-Chile Undercurrent. Simultaneous northern and southern branches have been observed by Stevenson and Taft (1971) and White (1973), whereas at other times an unbranched EUC (*Knauss*, 1966; *Stevenson and Taft*, 1971; *Leetmaa et al.*, 1987) or none at all (*Knauss*, 1960) has been detected. When present, the "downstream emerging" EUC (*Knauss*, 1966) tends to be deeper than the EUC to the west of the islands. This deepening is generally interpreted as an unspecified wake effect, though we may note that there is evidence that EUCs can be generated on quite small spatio-temporal scales. Although this phenomenon is not generally described in these terms, what is effectively a well developed *westward* EUC west of the Galápagos was reported during May 1983 (*Hayes et al.*, 1986), following a period of anomalous westerly winds during the El Niño. Hence it is possible that the eastern EUC is an entirely independent phenomenon, a relatively local response to the seasonally and interannually varying winds. Against this is the fact that the water mass characteristics of the eastern EUC are usually similar to those of the EUC proper; indeed these characteristics are sometimes the *only* evidence for an undercurrent to the east of the islands (*Pak and Zaneveld*, 1973).

Lukas also detected an annual cycle in the EUC. A relatively strong, shallow current in the northern spring was replaced quite suddenly by a weaker, deeper EUC, the change being accompanied by a temporary increase in the EUC transport and

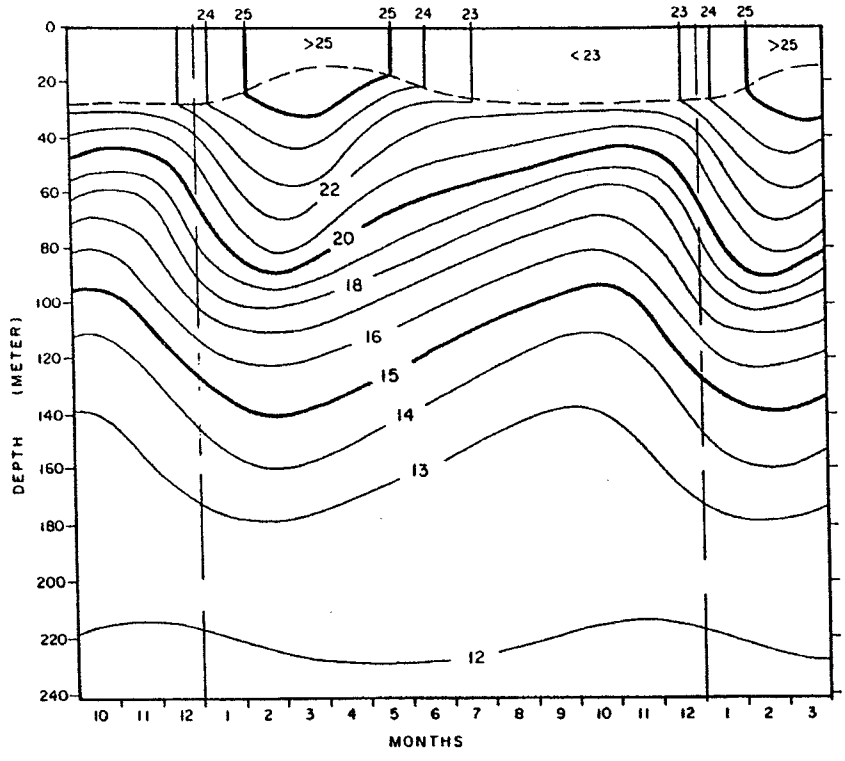

Figure 2.2: Time-depth diagram of temperature at 0°N, 115°W, representing a composite annual cycle as determined from the early historical hydrographic record (to 1964). From (*Lukas*, 1986), after (*Wyrtki*, 1964).

by the passage of a slug of high-salinity water. During the rest of the year the EUC relaxed gradually back to its spring condition. The EUC is generally found in the upper thermocline, so there is a corresponding annual cycle in the thermal structure, which is represented by Figure 2.2[1]. A shallow or even surfacing springtime EUC has been reported for instance by Schott (1943)—who, before the (re-)discovery of the EUC, noted eastward currents at about 100° to 105°W and just south of the equator in the ship drift data for March—and by other observers (*Jones*, 1969; *Halpern et al.*, 1983; *Wilson and Leetmaa*, 1988). Some of these authors observe or imply that near-surface eastward currents might be better described as a direct response to local wind forcing, rather than a surfacing of the EUC; the south-east trades which prevail on the equator west of the Galápagos are at their strongest in the late northern summer, when the ITCZ is most vigorous and furthest north, and at their weakest in the late

[1] Currents and temperatures in the top few hundred metres seem generally to be well correlated on timescales of more than about two weeks (*Hayes and Halpern*, 1984), so that the former may be used as a crude proxy for the latter

winter or spring, when they may even have a westerly component.

It is generally accepted that this annual cycle in the EUC and in the thermal structure may be characterised as the passage of a burst of downwelling first baroclinic mode Kelvin waves in the spring, these waves having been forced by westerly winds in the west or central Pacific a month or two earlier. Direct observational evidence for the existence of these waves in the east Pacific has been found (*Ripa and Hayes*, 1981; *Hayes and Halpern*, 1984), and there is a large literature on the waves and their connection to the winds, Kindle and Phoebus (1995) being a good recent entry point to this literature. The waves are also believed to be involved in the onset of El Niño (*Toole*, 1985; *Mangum et al.*, 1986), when there is also a temporary strengthening and deepening of the EUC before it weakens or vanishes in the face of the subsequent adverse pressure gradient (*Leetmaa et al.*, 1987).

The Kelvin waves also have a signature in the sea-surface height (SSH), observed *e.g.* by Ripa & Hayes (1981) and Hayes *et al.* (1986), and zonal velocity (u) fields. In each case the meridional structure of the anomaly associated with the wave is a Gaussian centred on the equator, and both anomalies are positive for the downwelling wave. Because SSTs decrease to the east along the equatorial Pacific, there is an eastward advection of relatively warm water associated with the waves. This, rather than meridional advection, is likely to be the reason for the anomalously warm temperatures in the east Pacific during El Niño and during the boreal spring of "normal" years (*Mangum et al.*, 1986; *Leetmaa et al.*, 1987)—the seasonal Kelvin wave is presumably part of the reason why the SST in this region is dominated by an annual cycle (cf. section 2.2.1 below) rather than the semi-annual cycle that might be expected given that the insolation at the top of the atmosphere is dominated by the semi-annual harmonic at the equator. The SST anomalies are larger over the cold tongue than they are further north or south, for two reasons. Firstly, the current anomalies and ambient SST gradients are larger on the equator. Secondly, even when the winds still have an easterly component, which might be expected to offset the warming via upwelling, the depression of the thermocline is such that it is the warmer, advected, waters that are upwelled (*Mangum et al.*, 1986; *Hayes et al.*, 1986). The effects of wind and waves need to be separated from those of the topography, though evidence

presented in this chapter and in Chapter 3 strongly suggest that the islands can have an impact on the cold tongue for some thousand kilometres or so to the west.

From one point of view, the decrease of SST from west to east along the equator is a strictly *coupled* phenomenon (*Dijkstra and Neelin*, 1995). From a more purely oceanographic perspective it is one aspect of the eastward shoaling of the thermocline, and it is here that the Galápagos might be having an effect. Large-scale oceanographic observations imply that the shoaling of the thermocline seems to stop, the zonal pressure gradient (ZPG) goes through zero, and the EUC sometimes surfaces, at between 95°W and 115°W (*Schott*, 1943; *Knauss*, 1960; *Knauss*, 1966; *Lukas*, 1981; *Lukas*, 1986; *Wilson and Leetmaa*, 1988), *i.e.* some distance to the west of the islands (although the shoaling of the iso*halines* appears to continue even beyond the Galápagos (*Knauss*, 1960; *Stevenson and Taft*, 1971)). This is often taken to imply that the islands play no part in the shoaling, with wind patterns suggested as an alternative cause. However, Knauss (1960) observed the EUC core sloping down and its speed decreasing as the Galápagos were approached, which is consistent with an erosion of the EUC from above by westward currents, either wind-generated or retroflected from the topography as suggested by Houvenaghel. Also, the November 1982 and May 1983 dynamic height sections of Hayes *et al.* (1986) show local maxima immediately to the west of the islands, albeit under El Niño conditions. Furthermore, climatological winds such as those used to force the OCCAM model and described briefly in section 3.1 do not seem to have any significant features at the longitudes in question (although the line separating westward from eastward wind stress does often meet the equator some 5 or 10 degrees to the east of the islands). Finally, observations within the four or five degrees of longitude immediately west of the islands have frequently revealed that the isotherms and isohalines continue to shoal all the way to the west coast of Isla Isabela (*Christensen*, 1971; *Pak and Zaneveld*, 1973; *Steger et al.*, 1998). So the observational evidence does point to a zonal convergence and upwelling of waters west of the Galápagos, but is equivocal concerning the zonal scale on which this effect is felt. This is one of the questions to be addressed by various means later in the thesis.

2.1.2 IRONEX2 ADCP data

R/V Iselin conducted a hydrographic survey and several ADCP transects in the vicinity of the Galápagos during the iron fertilization experiment IRONEX2 of November 1993, as described in Steger *et al.* (1998). The purpose of this cruise was to determine the origin of the fertile waters responsible for the plankton bloom of the "Galápagos Plume" that is frequently found immediately to the west of the islands; as noted elsewhere, the cruise produced unequivocal evidence that these waters originate in the EUC. However, the ADCP dataset also illuminates several other of the questions being discussed here, notably the fates of the EUC and SEC as they flow into and around the archipelago. The SOI (Figure 2.12) suggests that the cruise took place during a brief period of respite from ongoing El Niño conditions. The ATSR SST composite for November 1993 confirms that the ocean was in a "normal" state for this time of year, with a pronounced cold tongue terminating at the Galápagos and a large region of cool water off the South American coast which did not, however, extend as far west as the islands. So the dataset may be taken as typifying conditions which prevail at the Galápagos for much of the year, except during El Niño.

ASCII files containing the raw 150 kHz ADCP data were obtained and alignment and sensitivity corrections applied as described in Steger *et al.* (1998). Obviously spurious data (for instance where the ship velocity was recorded as 40 $\mathrm{m\,s^{-1}}$ or more) were excluded and the remaining data sorted on time. A set of zonal and meridional sections of u and v was extracted, averaged into longitudinal or latitudinal bins of 0.01° width where this did not produce data gaps, and 0.05° otherwise (Steger *et al.* used a bin size of 0.01°). In the vertical the bin size was 4m, as in the supplied data, the shallowest and deepest bins being at 9 and 405m respectively. This is an important dataset in the context of the present study, being the only readily available high-resolution current profiling dataset that contains measurements from both east and west of the islands at a time when the phenomena of interest here are likely to be present[2]. Many of the data have not been presented before[3], which is why

[2]The AVHRR satellite SST data (*Kidwell*, 1995) for this period also show a pronounced cold patch to the west of the islands, extending to at least 95°W

[3]Steger *et al.* display the north-south sections of u with selected v values superposed as arrows; and vector velocities at the surface and 75m (the approximate depth of the EUC).

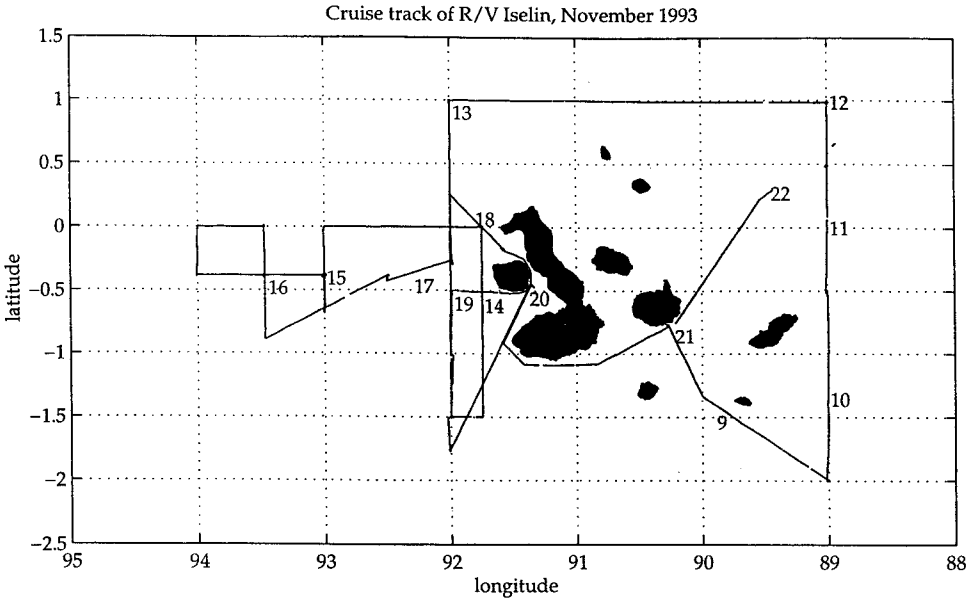

Figure 2.3: Cruise track of *R/V Iselin*, November 1993. There is one dot per ADCP sounding, although these cannot be made out separately because of the high density of soundings. The numbers are day numbers in November; the position of each number indicates the location of the ship at 00Z on the given day.

more sections are displayed here than are strictly necessary for the furtherment of the present argument. However, only data down to 150m depth are shown here, the main focus of this thesis being on the near-surface flows.

From Figure 2.3, which shows the location of each ADCP sounding, it can be seen that the following transects are available: north-south sections at 89°W and 92°W spanning the latitude range of the islands; a somewhat shorter north-south section at 91.75°W, very close to the western coast of the islands; three even shorter sections at 93°W, 93.5°W and 94°W; an east-west transect at 1°N spanning the longitude range of the islands; and an incomplete section along the equator from the islands westward to 94°W. A third east-west section has been constructed as a composite of the data west of the islands between 1°S and 0.1°S and is taken to represent the flow at about 0.5°S. These sections are presented as Figures 2.4, 2.5 and 2.7.

The section of u at 92°W (Figure 2.4) is very similar to that obtained nine years earlier by Wilson and Leetmaa (1988) (during a similarly quiescent phase of the

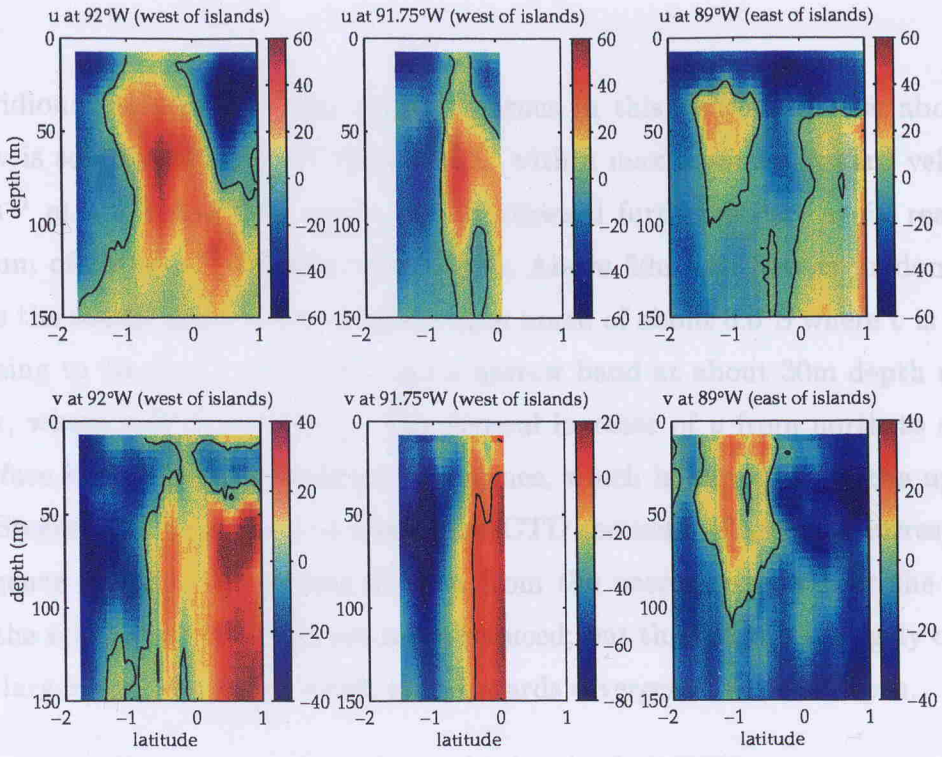

Figure 2.4: North-south transects of u and v ($\mathrm{cm\,s^{-1}}$) obtained using a shipboard ADCP on the *R/V Iselin* during the IRONEX2 expedition of 8th–22nd November 1993. Sections are at 92°W and 91.75°W (west of the islands) and 89°W (east of the islands). Data have been composited into 0.05° bins and smoothed in the horizontal with a 5-point rectangular filter. The black lines are contours of zero velocity component.

ENSO[4]) and reproduced in Figure 3.18 (page 78). Both sections show an EUC with a core of about 60 $\mathrm{cm\,s^{-1}}$ located just south of the equator (at about 0.5°S) and at a depth of about 70m. In both cases the eastward currents extend weakly to the surface and are flanked by westward jets of maximum speed exceeding 80 $\mathrm{cm\,s^{-1}}$ centred at 0.5 to 1°N and (apparently) somewhere just south of 2°S. Detailed differences are that the northern jet has its core at the surface in 1984 but at a depth of about 30m in 1993; and that in 1993 there was a secondary core of eastward velocities to the north of and slightly deeper than the EUC. This feature may be a remnant of the Northern Subsurface Counter-Current (NSCC) that is commonly observed in the western equatorial Pacific (see *e.g.* Brentnall (1995)), but it is absent from the 1984

[4]Except that in November 1993 the region was just recovering from an extended, though not particularly severe, El Niño.

section.

Meridional currents are also rather vigorous in this section. Below about 50m the flow is southward south of about 0.7°S, with a maximum southward velocity of 50 $\mathrm{cm\,s^{-1}}$ at 1.5°S and 80m depth, and northward further north, again reaching a maximum of 50 $\mathrm{cm\,s^{-1}}$ (at 65m and 0.4°N). Above 50m the flow is predominantly towards the south, apart from a shallow layer north of about 0.6°S where v is positive (increasing to 10 $\mathrm{cm\,s^{-1}}$ at 0.5°N), and a narrow band at about 30m depth near the equator, where v is close to zero. The general increase of v from north to south in the surface layer implies meridional divergence, which in turn implies the upwelling which Steger *et al.* also inferred from their CTD sections. There is a corresponding convergence lower down, as can be seen from the narrow region near the equator where the northward velocities are much reduced; but this feature is largely obscured by the larger-scale patterns, which tend towards divergence even at depth.

Comparing the sections of u and v at this longitude (92°W), we can summarise the flow here as follows. In the top 30m or so there is a pair of jets toward the south-west; deeper down there is an eastward EUC which is moving towards the north, perhaps before being steered around the Galápagos. The lower part of the northern surface jet is also embedded in this northward flow, producing large vertical shears in this region[5]. Directly to the south of the EUC is a zone of strong southward flow.

By the time it reaches 91.75°W, just 25 km further east (middle two frames of Figure 2.4), the EUC core speed has reduced from 62 to 49 $\mathrm{cm\,s^{-1}}$, and the EUC transport (defined as the total eastward transport above 150m and in the latitude range covered by the 91.75°W section) has reduced from 4.1 to 1.8 Sv. Part of the decrease in speed can be explained by a zonal convergence corresponding to the vertical spreading of isopycnals, with shoaling near the surface, which Steger *et al.* observed in their CTD section at 0.25°S as the islands were approached. This is confirmed by the fact that the surface flows are westward over a greater proportion

[5]Richardson number calculations in Steger *et al.* do not, however, indicate vertical mixing at this location—the northern jet is within the warm, fresh water north of the Galápagos Front, so the water column is gravitationally very stable here. A small patch of enhanced, but still much less pronounced, vertical shear at 100m at 0.5°S (*i.e.* at the base of the EUC, where there is no such stabilising influence) is sufficient to push the Richardson number below 0.25, indicating turbulent mixing.

of this section than they are at 92°W, as if the upwelled waters are being advected downwind as suggested by Houvenaghel. The remainder of the decrease in the EUC transport can probably be attributed to the current being diverted around the islands. The remarkably large southward velocities south of the equator, exceeding 120 cm s^{-1} in places (note the different colour axis used in this frame), suggest that a branch of the current is being steered around the southern edge of the archipelago, though the fact that the currents are to the west, albeit weakly, in the same region might rather indicate a retroflection or recirculation of these waters. Otherwise, the surface currents are similar to those at 92°W, a two-jet structure being apparent here as well.

At 89°W, immediately east of the islands, the two surface jets are still discernible, though they are not as clearly separated as they are further west. In particular, there is no band of eastward velocity between them. It is possible that this represents an early phase of the splitting of the SEC into two branches by the topography—the bathymetry suddenly rises to about 250m at this longitude and at precisely the latitude (1°S) of minimum westward velocity (see Figure 1.1). This is corroborated by the fact that the jets are closer together in the eastern section, the northern jet being centred a few tenths of a degree *south* of the equator. On the other hand, there is what appears to be a "downstream emerging" southern branch of the EUC (in the terminology of Knauss (1966)) at this latitude (and about 50m depth), and this may be responsible for the division, as is conventionally suggested. A northern branch of the EUC seems also to be present at about 1°N and 50m (*i.e.* at least 20m shallower than the incident EUC), though unfortunately this is on the edge of the transect. The section of v at this longitude is dominated by the converging northward and southward velocity components centred at about 40 or 50m, which suggests that these two branches are moving together and may merge at some point further east[6]. There is also a "downstream emerging" version of what we tentatively identified earlier as the NSCC. All of these currents seem to have been enfeebled by passing round the islands, though the 89°W sections do not extend far enough north to compare the transports east and west of the islands.

[6]The theory outlined in Appendix A predicts that this will happen, *i.e.* that the flow to the east of the islands will eventually be essentially the same as that to the west, give or take the effects of friction and non-linearity.

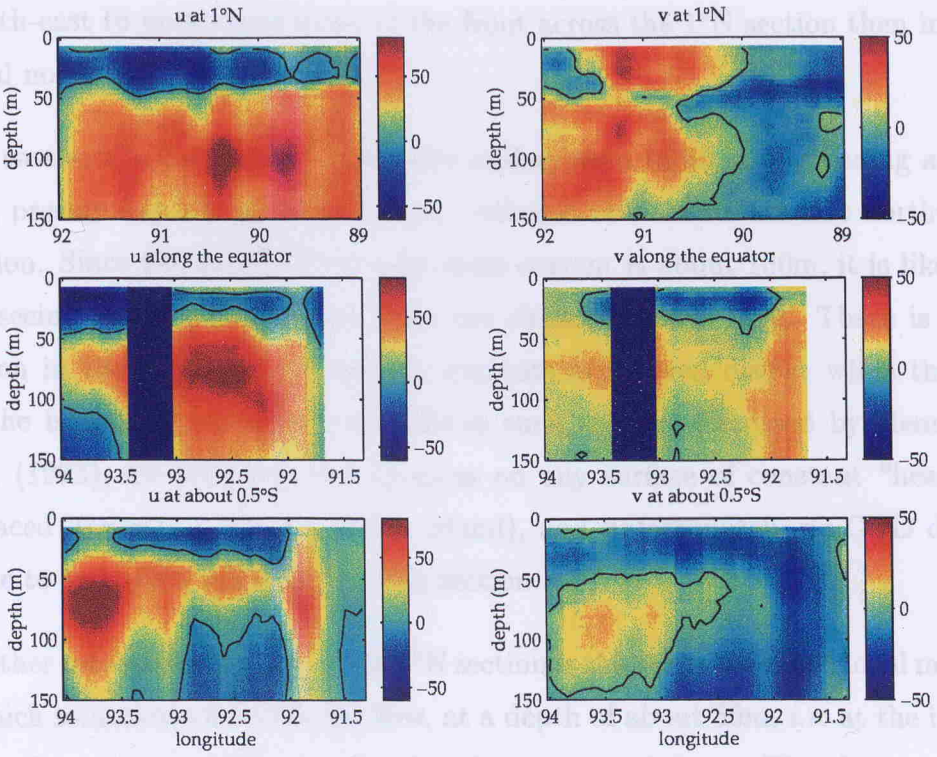

Figure 2.5: As Figure 2.4 but for east-west transects at 1°N, 0°N and nominally (see text) 0.5°S. As in the previous figure, the black lines are zero isotachs.

Further clues to the effect of the islands on the currents are provided by the east-west sections of Figure 2.5. The section at 1°N, which spans the longitude range of the island group, shows a simple pattern of surface westward flow overlying deeper flows to the east. The surface flow, representing the northern branch of the SEC, suddenly becomes stronger at about 90.5°W. Referring to Figure 1.1, this would appear to be due to northward deflection of this current by the three small northern islands (Islas Pinta, Marchena and Genovesa), bringing the core of the jet to this latitude from the more southerly location we noted at 89°W; and indeed, in the v section at this latitude, northward currents commence at 90°W, the longitude of Isla Genovesa, the furthest east of the three islands. Interesting confirmation of this interpretation is provided by Figure 2.6, which shows the cruise track superimposed on a contemporaneous SST image from the AVHRR satellite instrument (*Kidwell*, 1995). Despite surface heating and vertical and horizontal mixing, SST can to a certain extent be used as a tracer on short timescales; in this region, the large meridional SST gradients associated with the Galápagos Front roughly indicate the location of the northern branch of the SEC.

The south-east to north-west slope of the front across the 1°N section then indicates a general northward motion.

The eastward zonal flow at depth also undergoes a rapid strengthening at about 90.5°W, presumably for the same reason—subsurface currents are also northward in this region. Since the depth of the maximum current is about 100m, it is likely that we are seeing the "NSCC" rather than the shallower EUC here. There is no real indication in the ADCP data that the currents are driven deeper while they pass round the islands (for Bernoulli-type flows such as that discussed by Hendry and Wunsch (1973), for instance, this happens on any surface of constant "head" that is displaced upwards upstream of the island), and unfortunately no CTD data are available to test this possibility for this section.

Another interesting feature of the 1°N section is the sharply defined local minimum of v, which sometimes reverses the flow, at a depth of about 50m, *i.e.* at the interface between the surface westward and subsurface eastward flows. This feature extends across the whole section. Sections at 89°W presented by Steger *et al.* show that there is a very sharp pycnocline, with large vertical gradients of both salinity and temperature, at this depth, and sloping up towards the south. It is reasonable to assume that this pycnocline also extends across the whole of the 1°N section. The southward flow can then be characterised as an isopycnal flow down the pressure gradient induced by the increasing depth of (warm, fresh) water above the pycnocline as one moves towards the north, thus resembling a meridional version of the EUC, on a much smaller scale[7]. Both currents provide examples of near-equatorial flows which are not much affected by the Coriolis force.

The SST image of Figure 2.6 also suggests a meander in the northern branch of the SEC immediately to the west of the islands, reaching its furthest south at 93°W and furthest north at 92.3°W and 94.7°W. Interpreted as a wave, this would imply a wavelength of about 270 km, so this is not a TIW precursor (TIW wavelengths being more like 1000 km). It is more likely to be a smaller scale instability—we shall

[7]As noted in section 3.1, the winds in this region are usually southerly (to the north), as required to set up this pattern. Steger *et al.* report southerly winds for the time of this survey, although the TAO wind data at 95°W (see section 2.1.3) reveal a period of anomalously easterly wind during the latter stages of the cruise (from about the 17th onwards).

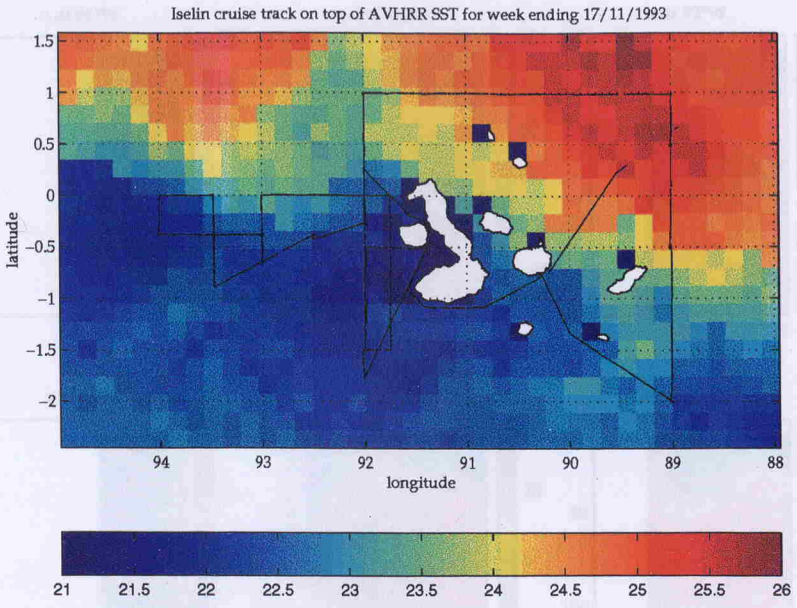

Figure 2.6: Cruise track as in Figure 2.3, superimposed on the AVHRR SST image (°C) for the week ending 17th November 1993. This covers the period when the east-west transects west of the Islands were undertaken.

see in section 3.4 that the flow in this region is sufficiently sheared to be inertially unstable. The existence of this meander is confirmed by the equatorial section of v in Figure 2.5, in which the surface currents are southward between 92 and 93.7°W, and northward elsewhere. The zonal velocity sections at the equator and 0.5°S also appear to indicate that the core of the northern SEC branch moves to the south between 92 and 93.5°W, and then northwards again further west.

Deeper down, these two sections again tell a consistent story about the fate of the EUC as it approaches the islands. From 94 to 93.4°W the EUC core is at about 75m depth and located close to 0.5°S, but northward currents in this region, discernible in both sections, are advecting it towards the equator, where it can be found between 93 and 92°W. Finally, in the last half degree or so before the islands are encountered, we see northward currents at the equator and southward currents at 0.5°S as the EUC divides into the two branches that will pass around the islands; eastward currents accordingly disappear at the equator and reappear at 0.5°S. In these longitudes both current components, especially the meridional ones, have spread out from the depth of the incident EUC to occupy at least the top 150m of the water column; this provides

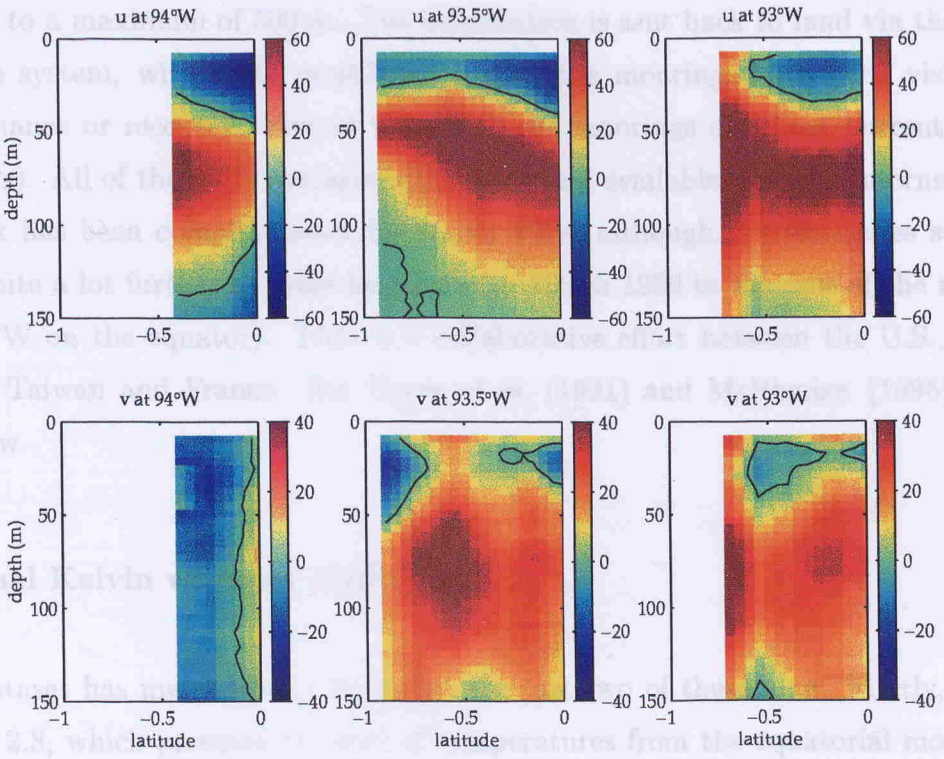

Figure 2.7: As Figure 2.4 but for north-south transects at 93, 93.5 and 94°W.

further evidence of a "piling up" of the EUC waters as they strike the islands.

Further details are provided by the short sections south of the equator at 93, 93.5 and 94°W presented in Figure 2.7. The SEC core is indeed furthest south (at 0.2°S) at 93°W, and moves northward further west; and the EUC core moves from south to north as we step through these sections from west to east (the strong north-eastward currents on the southern edge of the 93°W section are anomalous in this respect).

2.1.3 TAO mooring data

The TAO (Tropical Atmosphere-Ocean) array is a set of some 69 moored buoys in the tropical Pacific, covering an area from 8°N to 8°S and from 137°E to 95°W at an average longitudinal spacing of about 13°. There are typically seven moorings at each longitude, at 0, ±2, ±5 and ±8 degrees of latitude. Automatic weather observations are taken at each buoy, and sea temperatures are measured at several (usually ten)

depths, to a maximum of 500 m. The information is sent back to land via the Argos satellite system, with some recalibration after the moorings have been visited for maintenance or recovery. Five of the equatorial moorings also have current meters (ADCPs). All of the daily averaged data are freely available over the Internet[8]. The network has been complete since December 1994, although the timeseries stretches back quite a lot further at some locations (to March 1980 in the case of the mooring at 110°W on the equator). TAO is a collaborative effort between the U.S., Japan, Korea, Taiwan and France. See Hayes *et al.* (1991) and McPhaden (1995) for an overview.

Seasonal Kelvin waves at 110°W

The dataset has many uses; I shall describe just two of these here. Firstly, look at Figure 2.8, which presents 15 years of temperatures from the equatorial mooring at 100°W (the closest mooring to the Galápagos for which there is a long and reasonably continuous dataset). The data have been filtered to remove high-frequency variability. How do these observations compare to the composite annual cycle at 115°W discerned in the (limited number of) historical hydrographic observations by Lukas (1981; 1986) and Wyrtki (1964)? Recall that the picture they presented (Figure 2.2) had the thermocline plunging and to a certain extent weakening in the northern winter, reaching a maximum depth in February or March, and relaxing back more slowly over the rest of the year. Considering the thermocline to be represented by the 15°C and/or 20°C isotherms, we see that this picture is only arguably representative of "typical" conditions, and that there is a large amount of interannual variability. The pattern of the paradigm can be seen in the data for 1980–81, but the timing is quite different; the rapid isotherm depression takes place in October 1980, and the relaxation lasts only until March 1981, when another, slower, plunging event begins. The event of August 1981 is not followed by much of a relaxation—one might speculate that this conditioned the east Pacific to be receptive to the massive deepening event of late 1982 (apparent in data for 95°W, which are not shown here) that marked the onset of the exceptionally strong El Niño of 1982–83. Throughout 1983 the isotherms are

[8] ftp://ftp.pmel.noaa.gov/taodata

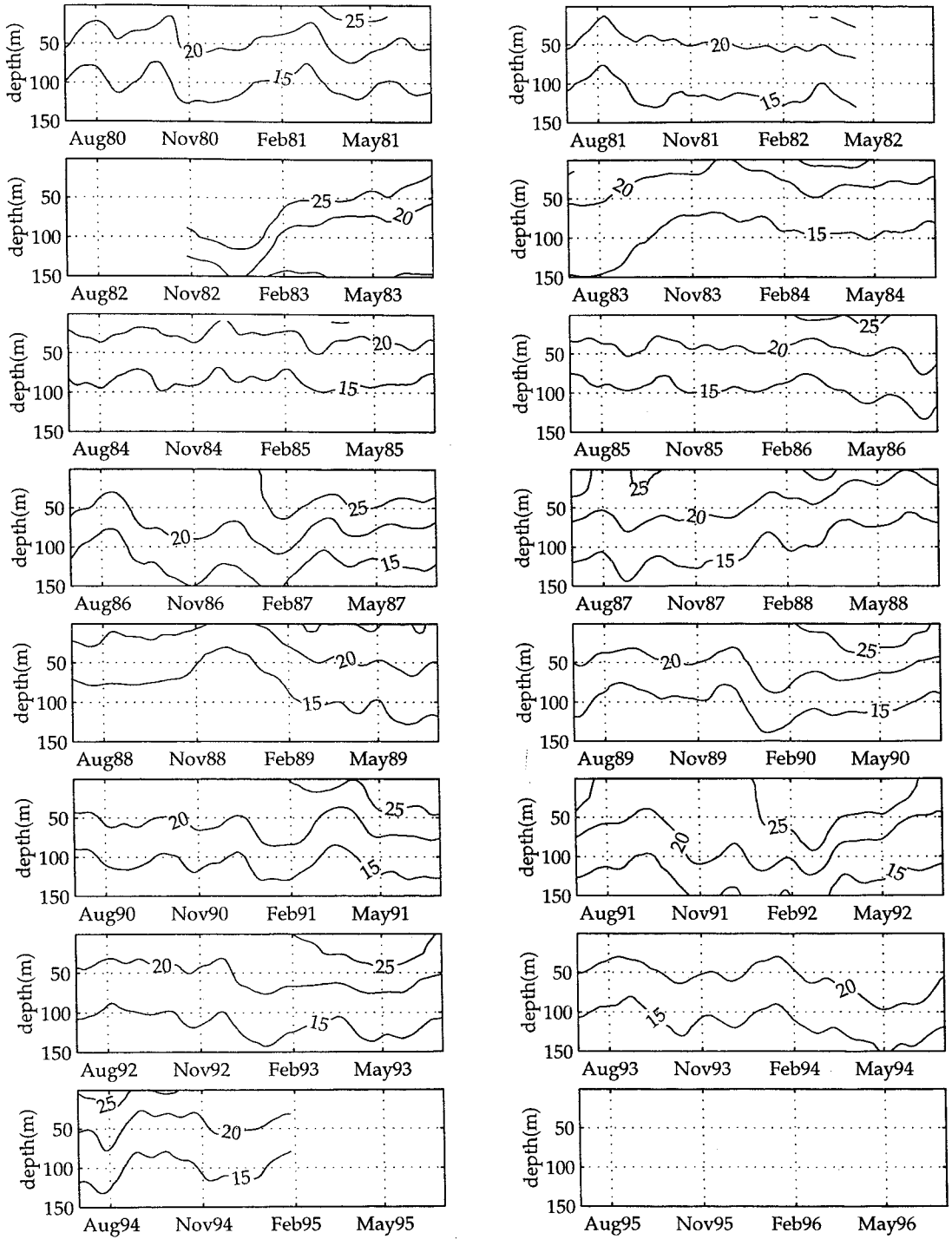

Figure 2.8: Time-depth diagram of temperatures at 0°N, 110°W for the period July 1980–February 1995, as measured by the TAO mooring at that location. Data have been linearly interpolated in the vertical, and data gaps of up to 5 days have been filled in using linear interpolation. Finally, the data have been filtered in time by convolution with a 31-point (31-day baseline) triangular window. Contours are at 15, 20 and 25°C.

gradually returning to a state characteristic of the quiescent conditions, with neither a strong El Niño nor a strong La Niña, which prevailed from the middle of 1983 until the boreal spring of 1986. During this period there is little evidence of seasonal Kelvin wave activity in the mooring data, but there is a downwelling event in June 1986 and another beginning in late August, this being associated with the beginning of the 1986–88 El Niño. Weaker events take place in January, April and August 1987, during the El Niño, but it is noticeable that such events are either absent or much less pronounced during the subsequent La Niña (mid-1988–mid-1989), apart perhaps from the slow descent of isotherms in late 1988/early 1989, which is, however, more likely to be connected to the annual cycle of surface temperatures. The next major downwelling event begins late in 1989 and is yet again associated with the onset of an El Niño, although this one turned out to be weak and short-lived. A similar event one year later did not lead to an El Niño—the isotherms quickly reverted to their "normal" positions—but after the two subsequent events of March–April and September–October 1991 there were again anomalously warm SSTs in the east Pacific. And so on.

One way of making the analysis more objective is to apply some *criterion* for a plunging event to the timeseries of depths of a given isotherm. The criterion adopted here is as follows: an event is taken to be in progress when the isotherm is some vertical distance d, or more, deeper than its shallowest position in the preceding n days. The smaller the value of d used, or the larger the value of n, the less stringent is the criterion, so that more and weaker events will be classified as such. This procedure was applied with various values of d and n to the data presented in Figure 2.8 (which has been smoothed with a 31-day triangular filter to remove variability on irrelevantly short timescales). In fact the results proved to be insensitive to the choice of n, and a value of 40 days has been used for all the results presented here. Events are taken to be separate only when there is a gap of 7 or more days for which this criterion is not satisfied.

Results are summarised in Table 2.1, which lists the number of events reaching maturity in each month according to different criteria. That is, a month is counted if the first day, during an event, on which the criterion is satisfied falls during that

	20°C			15°C		
$d =$	20	30	40	20	30	40
Jan	1	2	2	1	2	1
Feb	4	3		4	2	
Mar	1	1	1	4	1	
Apr	3	2		5	3	1
May	1			1	2	
Jun	1	1		1	1	
Jul	2			2		
Aug	5			4	5	
Sep	1	2	1	4	1	2
Oct	2	2	2	5	3	3
Nov	1				1	
Dec	6	3	1	7	4	2

Table 2.1: Number of plunging events reaching maturity in each month, for TAO data from 1980–1995 at 0°N, 110°W, using various criteria. Data for the 20°C and 15°C isotherms are presented. Referring to the text, d takes the values 20, 30 and 40 m, as indicated in the second row of the heading, and n is always 40 days. Only non-zero values are entered.

month. Data for the 20 and 15°C isotherms are presented for comparison; it will be seen that the results are quite similar for the two cases (the two isotherms follow each other closely in Figure 2.8 and especially in Figure 2.2), except that rather more events appear when the movements of the deeper isotherm are analysed. I shall concentrate on the 15° data. The three columns for each isotherm are for $d = 20$, 30 and 40 m, which may be classified as defining "weak", "moderate" and "strong" events respectively; for comparison, in the "seasonal Kelvin wave" of the composite annual cycle in Figure 2.2, the isotherms become about 40m deeper over a somewhat longer period of time. The results for the strong and weak events are presented in Figure 2.9.

The most noticeable thing about the strong events is that they tend to occur during the autumn or early winter, when isotherm depths and SSTs are at a *minimum* in the composite annual cycle of Lukas and Wyrtki. A second cluster of strong events in December–January is more in line with the traditional picture. For this cluster, the shallower 20°C isotherm tends to deepen later than the 15°C isotherm (cf. Table 2.1), which is consistent with the upward phase propagation (downward group

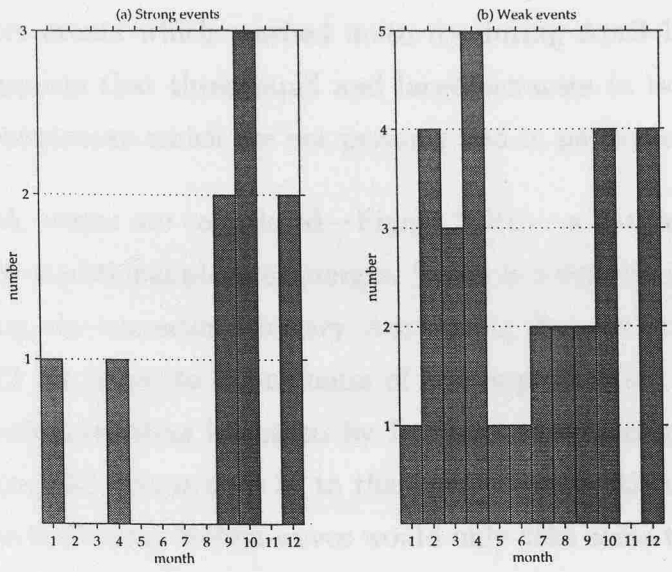

Figure 2.9: Bar chart showing the number of (a) "strong" and (b) "weak" deepening events of the 15°C isotherm at 110°W on the equator, from TAO data for March 1980 through February 1995. "Strong" events are those from column 6 of Table 2.1, *i.e.* those during which the 15°C isotherm deepened by at least 40 m. "Weak" events are those from column 3, except that those events which were merely the early stages of strong events have been excluded.

velocity) that would be expected of wind-generated waves, as noted by Lukas and other authors. Note, however, that current data obtained at 110°W during October 1980 by Hayes *et al.* (1984), when one of these events occurred, suggested a *modal* rather than a vertically propagating disturbance—the authors found only a small phase lag between zonal velocity and vertical displacement of isotherms, whereas for vertically propagating waves this lag would have been ±90°. This is consistent with the fact that none of the September–October cluster of strong deepening events shows a significant lag between the two isotherms. The data of Hayes *et al.* displayed pulse-like increases in the zonal current, consistent with the event being due to the passage of a Kelvin wave packet.

All but two of these strong deepening events are associated with nascent or ongoing El Niños. The one in October 1980 was followed by a weak El Niño (as defined using the Southern Oscillation Index (see below)), and the events of September 1986 and especially September 1981 marked the onset of severe El Niño episodes. The January 1989 event occurred during a long transition from La Niña to El Niño conditions. The

only exceptions are events which reached maturity during April 1981 and October 1993. Hence it appears that these rapid and large increases in isotherm depth are associated with phenomena which are not periodic and in particular not annual.

When the weak events are considered—Figure 2.9(b)—a pattern which is rather more similar to the traditional picture emerges. There is a definite peak in activity in the northern spring, the trimester February–April being that with the largest number of these events (12 compared to a maximum of 9 in any other set of three months). That this is slightly later than indicated by Lukas and Wyrtki may be partly due to the fact that the TAO mooring is 5° to the east of the location of their diagram, although low baroclinic mode Kelvin waves would only take some two to five days to cover this distance. Even with those events excluded which were classified as weak but were in fact the early stages of strong events, there is still a substantial amount of activity at other times of the year. These non-seasonal Kelvin waves seem to be quite randomly distributed through the year; the secondary peak in the northern autumn–winter suggested by the bar chart is not borne out when three-monthly aggregates are calculated, and no marked seasonal cycles appear when an annual composite over the entire TAO record is plotted.

Several theoretical, modelling and observational studies (see Kindle and Phoebus (1995) and refs.) have produced firm evidence that these Kelvin waves are generally driven by westerly wind bursts (WWBs), episodes of anomalously westerly (eastward) wind in the central and western equatorial Pacific. The specific connection between WWBs and the downwelling events identified at 110°W has been examined using the WWB classification of Hartten (1996), which covers the period from 1st January 1980 until 31st December 1989. Hartten examined the ECMWF wind archive for the 1980s and produced a list of the start and end dates of all the WWBs that occurred during this period (according to some criterion[9]), together with their east- and west-most limits.

The following criterion was adopted: a given downwelling event is taken to have been caused by a WWB if the start of the event (defined as 40 days before the event

[9]Namely the persistence for at least two days of winds with a westerly component of 5 m s^{-1} or more over at least 10° of longitude on the equator.

reaches maturity, for reasons which will be obvious from the above) occurs at a time t consistent with its being due to a first or second baroclinic mode Kelvin wave initiated at the time and location of some WWB. That is, if the start and end times of a WWB are t_1 and t_2, and the distance from the western and eastern limits of the burst to the mooring location at 110°W are respectively Δx_1 and Δx_2, the wind burst is taken to have contributed to the event if

$$1 < \frac{\Delta x_1}{t - t_1} \text{ or } \frac{\Delta x_2}{t - t_2} < 3 \text{ m s}^{-1}, \tag{2.1}$$

where distances are in metres and time intervals in seconds. Here the assumption has been made that a signal propagating at between 1 and 3 m s^{-1} could be due to a first or second baroclinic mode wave. Typical wave speeds are respectively about 2.5 and 1.3 m s^{-1}, so these bounds are rather permissive. However, the method does seem to give meaningful results.

These results are presented in Figure 2.10, which shows the temporal distribution of Hartten's WWBs in relation to the downwelling events at 110°W, and indicates which of them could or could not have caused downwelling events, according to the above criterion. In the lower panel is shown the Southern Oscillation Index (SOI) of normalised atmospheric pressure difference between Tahiti and Darwin. When this is negative, the pressure in the west (at Darwin) is anomalously high compared to that in the central Pacific, indicating El Niño conditions, and conversely when the SOI is positive La Niña conditions can be expected. The SOI is well correlated with other measures of the ENSO (*Philander*, 1990).

Perhaps the most striking aspect of this figure is the temporal distribution of the WWBs with respect to the ENSO. Bursts are frequent before and during the 1982–83 El Niño, and again during the 1986–87 and 1989–90 events, and are generally absent during periods of quiescence (1983–86), La Niña (1988–89) or recovery from El Niño. This confirms the point, made by Hartten himself and others, that WWB activity plays a large part in producing and maintaining El Niño conditions. The cluster of WWBs in 1984–85, which seem to have produced some downwelling but did not lead to an El Niño, shows that other factors are also important, perhaps a pre-conditioning of the east Pacific; but that is another story.

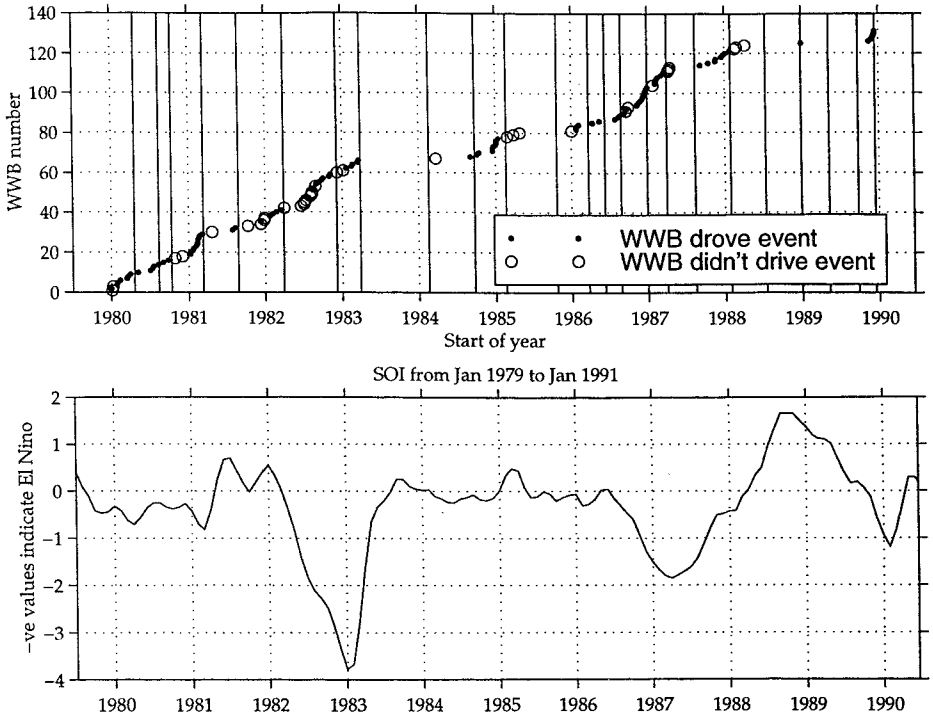

Figure 2.10: Top: Shows which of the westerly wind bursts classified as such by Hartten (1996) could have driven downwelling events at 110°W, assuming these to have been first or second baroclinic mode Kelvin waves, according to the criteria discussed in the text. The solid vertical lines represent the times at which the downwelling events occurred. Bottom: Monthly Southern Oscillation Index for this period, smoothed with a 5-month triangular filter.

The downwelling events themselves, indicated by the vertical lines in the upper panel of Figure 2.10, are more evenly distributed in time, though a certain amount of clustering is discernible before and during the two large El Niños of the decade, particularly the later one. According to our criteria, all six of the strong events, and all but 7 of the 24 weak events, could have been caused by wind bursts. Of these 7, six[10] occurred during quiescent or La Niña conditions when the isotherms will have been near the surface and especially susceptible to local and other influences. The seventh (August 1987) was during the early stages of recovery from El Niño. To reiterate, these are in any case *weak* events which may be pushing our detection criteria to the limit.

[10]February 1984, October 1985, July 1988, December 1988, May 1989 and September 1989.

So far we have been considering the probability of an event being caused by one or more wind bursts. We now turn briefly to the complementary question of the likelihood of a given WWB producing a downwelling event. All but 34 of the wind bursts occurred at times consistent with their having produced downwelling events at 110°W. Of these 34, 22 occurred during El Niño events, when the isotherms will have been maximally depressed anyway, and two more were at the start of the decade, before the TAO data began to be recorded.

When the first two modes were considered separately, by using ranges of respectively 2 to 3 and 1.16 to 1.44 m s^{-1} in (2.1)[11], it was found that they were approximately equally likely to have produced downwelling events[12]. Other workers (*e.g.* Giese and Harrison (1990)) have implicated higher as well as first mode waves in the transmission of WWB energy, and further motivation for examining the higher modes appears in section 3.5.

The conclusions of this subsection are:

1. Many downwelling events are observed in the eastern equatorial Pacific. A seasonal cycle somewhat similar to that found long ago by Wyrtki and Lukas, and ascribed to Kelvin wave activity, is present, but there is a significant aperiodic component superposed on this, particularly in the more pronounced waves often associated with the onset of El Niño.

2. A large proportion of the downwelling events occur at times consistent with their being caused by westerly wind bursts in the central and west Pacific. From the point of view of timing, first and second baroclinic mode waves are approximately equally likely to have transmitted the energy from the region of the WWBs to the point of detection at 110°W.

Intraseasonal variability in the vicinity of the Galápagos is hence partly determined by these remotely forced events. A related question, to be considered elsewhere

[11]The second range here is chosen so that the spread of arrival times at 110°W is the same for each mode.

[12]Mode 1 waves were able to explain 13 of the 24 weak events in the period covered by Hartten's study, and 5 of the 6 strong events. 33 of the 131 WWBs could have been responsible for deepening events. For mode 2, the figures were respectively 13, 3 and 33.

in the thesis, is the extent to which this local intraseasonal variability is a product of an interaction between these waves and the islands' topography; in particular, how do the waves relate to the seasonal spreading out of the cold patch to enhance the cold tongue?

Westward propagating SST signals in the cold tongue

As a second application of the TAO data, westward propagating signals in the SST have been sought by means of calculating correlations between the timeseries from the neighbouring moorings at 95°W and 110°W on the equator. These are the two moorings closest to the Galápagos, so that if any westward expansion of the cold tongue away from the islands were to show up in the TAO record, it would be in the series from these two moorings. A significant correlation between the two series, with the 95°W data leading the 110°W data by an amount consistent with some physically possible means of propagation, can be taken as evidence for such westward propagation.

An example of such a correlation is presented as Figure 2.11, which shows the lagged correlation coefficients between the two moorings' SST series for the period from 18th November to 11th December 1992. This period was identified by plotting trajectories of the (T_{95}, T_{110}) pairs; with T_{95} on the horizontal axis, a cooling propagating from east to west appears as an anticlockwise trajectory segment in the second quadrant[13]. The cluster of three correlation coefficients at lags of 9, 10 and 11 days, significant at the 95% level[14], with a maximum at 10 days, correspond to a signal propagating westwards at a speed of about 2 m s^{-1}. This is rather fast for purely oceanic (unforced/uncoupled) processes, although a first baroclinic mode inertia-gravity wave of small wavelength could have such a group velocity—the short-wave limit for the group velocity is the speed c of Kelvin waves, which is about 2.5

[13] If T_{95} begins to decrease while T_{110} stays the same, the trajectory moves to the left; if T_{110} then begins to decrease also, the trajectory has a downward component and executes an anticlockwise arc.

[14] *Caveat*: This assumes that the number of degrees of freedom is $n - 1$ where n is the number of overlapping days used to calculate the correlation at that lag. This may be optimistic since autocorrelations of the individual series can reduce the effective number of degrees of freedom as explained *e.g.* in Davis (1976). Calculations of the integral timescales of the series, however, proved inconclusive.

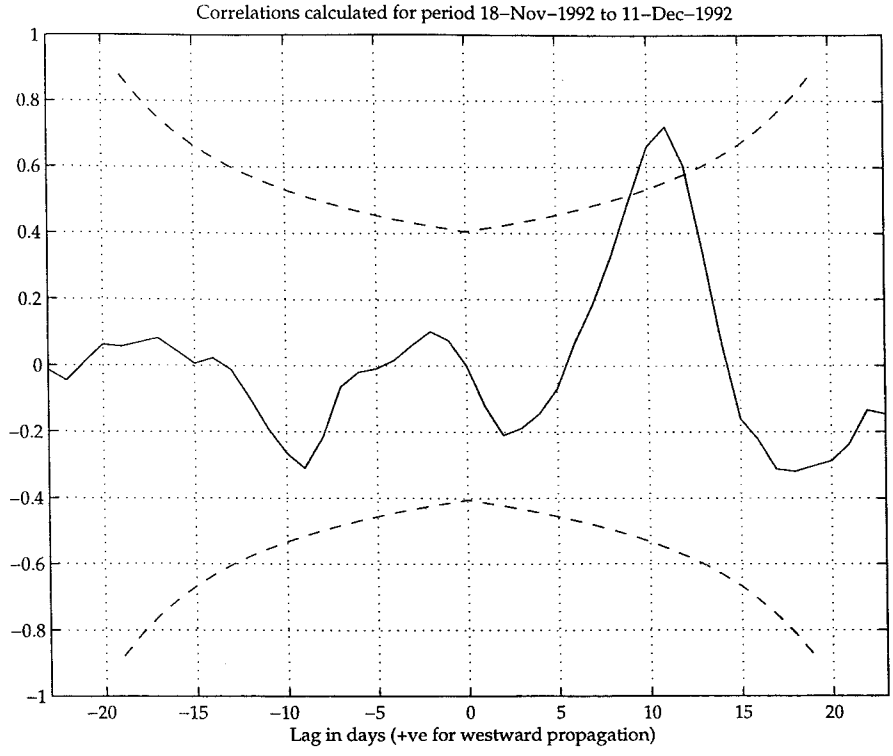

Figure 2.11: Lagged correlation coefficients between temperatures at a nominal depth of 1 m at 0°N, 110°W and 0°N, 95°W, for the period 18th November 1992 to 11th December 1992. Positive lags are where the signal at 95°W leads that at 110°W, *i.e.* correspond to westward propagation. The dashed lines are the 95% significance limits.

m s^{-1} for this mode in this region. Furthermore, a smaller group velocity would be required if the wave were propagating relative to (*i.e.* were Doppler-shifted by) the SEC. It is also interesting that this, the most plausible example of westward propagation that I have been able to find, coincides in time with the best monthly mean composite of apparent cold tongue enhancement west of the Galápagos in the ATSR record (Figure 3.4, lower panel).

In fact, there are at least three reasons why such evidence may be difficult to find. Firstly, El Niño conditions prevailed for most of the period for which data from both moorings are available. This means that the cold tongue will have been generally weak and that eastward propagating signals such as those associated with equatorial Kelvin waves will have been more common. Secondly, 110°W is towards the western limit of the postulated influence of the islands on the cold tongue (cf. Figure 3.4),

so that we might expect signals to penetrate this far west only rarely and perhaps weakly. And finally, as noted in section 3.2.1, the expansion of the cold tongue away from the islands appears to take place most vigorously at about 1°S, rather than along the equator, at least in the OCCAM output, and there are no moorings at this latitude.

2.2 Satellite observations

2.2.1 ATSR SSTs

The Along Track Scanning Radiometer (ATSR) is a multi-channel infrared radiometer flown on board the European Space Agency's ERS platforms. It achieves an improved atmospheric correction, as compared to earlier such instruments, by viewing each point on the Earth's surface twice: once at nadir (directly below the satellite), and once obliquely at a slightly earlier time (about three minutes earlier) when the point lies ahead of the satellite along its track, whence the name. Sensor noise is minimised by cooling the sensor to 80K. By these and other means, it is claimed that the skin temperature can be measured to within 0.3K of radiometric temperatures measured *in situ* (*Mutlow et al.*, 1994; *Barton et al.*, 1995).

Global daily SSTs (of varying spatial coverage due to the finite track width and to the repeat cycle in operation at any time) are available on CD-ROM from the Rutherford Appleton Laboratory (*Murray*, 1995) or, with an improved cloud identification algorithm (*Jones et al.*, 1996a; *Jones et al.*, 1996b), on-line at the SOC. "Daytime" and "night-time" fields, as defined from a visible-wavelength sensor on the satellite, are kept separately; between three and eight daytime SSTs per month are typically found at each gridpoint and similarly for the night-time data. The former dataset (CD-ROM) covers the period from 1st August 1991 to 31st July 1995; the latter, 1st January 1992 to 31st August 1995. Both are on a half-degree grid (although higher resolution data, down to about 1km, are in principle obtainable) and thus provide a readily available timeseries of SST showing mesoscale or larger features effectively smoothed over a period of a week or two. (The utility of this dataset for equato-

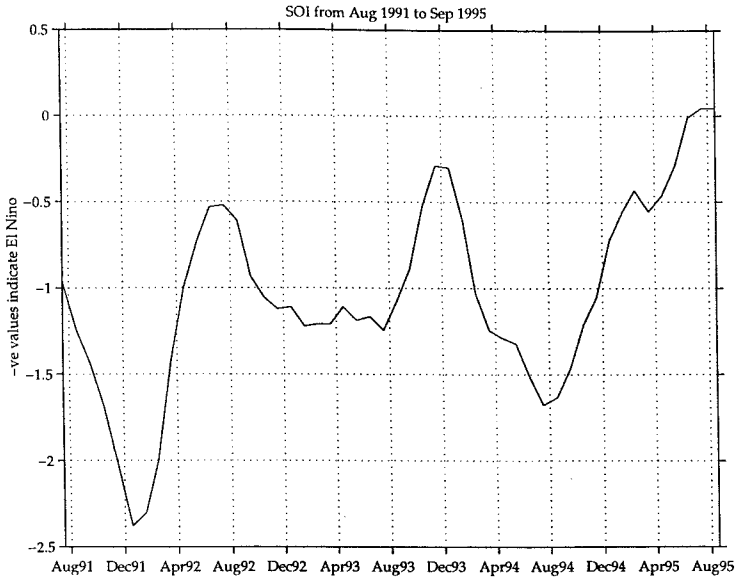

Figure 2.12: Monthly SOI (see section 2.1.3) for the period covered by the ATSR record. Data have been smoothed with a 5-month triangular filter.

rial studies has been demonstrated *e.g.* by the work of Allen *et al.* (1995) on phase propagation of tropical instability waves.)

More or less permanent El Niño conditions prevailed during the period of this dataset (Figure 2.12). An increase in SST, deepening of the thermocline, weakening or even reversal of the SEC, and disruption of the EUC are therefore all likely (see *e.g.* Firing *et al.* (1983)), and all tell against the Galápagos affecting the cold tongue noticeably during this period (recalling the possible mechanisms outlined in Chapter 1). Nevertheless, monthly composites can still be found in which the effect can be made out, for instance that for December 1992 (Figure 3.4, page 54), where the equatorial cold tongue is clearly strengthened to the west of the Galápagos. The region of lowest equatorial temperatures is not continuous with the coastal upwelling region off Peru and Ecuador, as is sometimes assumed on the basis of relatively low-resolution datasets (such as the 2° resolution Comprehensive Ocean-Atmosphere Data Set (*Woodruff et al.*, 1987)) typically used for GCM verification.

Principal component analysis (PCA), *i.e.* the calculation of "empirical orthogonal functions" (EOFs), has been applied to the series of monthly mean SST fields as a means of identifying objectively, and quantifying, any enhanced SST variability to

the west of the Galápagos. Figure 2.13 shows the first five EOFs calculated from the series for the indicated region (*i.e.* the whole equatorial east Pacific) over the period April 1992 until December 1993, this being the longest continuous period for which reasonably complete coverage of this region was obtained.

EOF 1 (*i.e.* the first eigenvector of the covariance matrix), which explains 86.5% of the total variance, is of the same sign over almost all of the region, the only exception being a small region off the Central American coast where the variance is in any case small, showing that the variability is dominated by patterns which are in phase over the region. The time series of the expansion coefficient associated with this EOF is close to a sinusoid having a 12 month period, so that the variability is concentrated in the annual cycle. The largest variances and pattern value magnitudes are found in a tongue extending from the Peruvian coast at about 5°S north-westwards towards the Galápagos. Examination of a timeseries of the monthly SST fields shows that this is associated with periodic and aperiodic extensions in this direction of the cold waters of the Peru-Chile coastal upwelling zone (which is due to equatorward winds along the coast). A similar but weaker feature can sometimes be seen extending south-westwards from the Colombian/Central American coast[15]. The dipole-like structures along the coast in EOFs 1 and 2 show that the extensions from the north are out of phase with those from the south. This phenomenon is probably associated with north- and southward migrations of the ITCZ; in the northern summer, the ITCZ is at its furthest north and the Peruvian coastal winds at their strongest, so the southern cold patch has its greatest extent, and conversely.

Away from the South/Central American coast the variance and the magnitude of the elements of the eigenvector decrease monotonically away from the equator; there is a large annual cycle in the cold tongue and not much of one elsewhere. This is confirmed by a map of the amplitude of the annual cycle—not shown here—obtained from a least squares fit to an annual sinusoid; the pattern of amplitudes is to the eye indistinguishable from that of the first EOF. Along the equator, the variance and the pattern values both have a maximum at about 93°W, just to the west of the Galápagos, and drop off steadily to the west (Figure 2.14). These statistics clearly

[15] The band of warm water just north of the equator often extends right to the coast, and sometimes southwards from here to separate the extended Peruvian coastal cold patch from the coast.

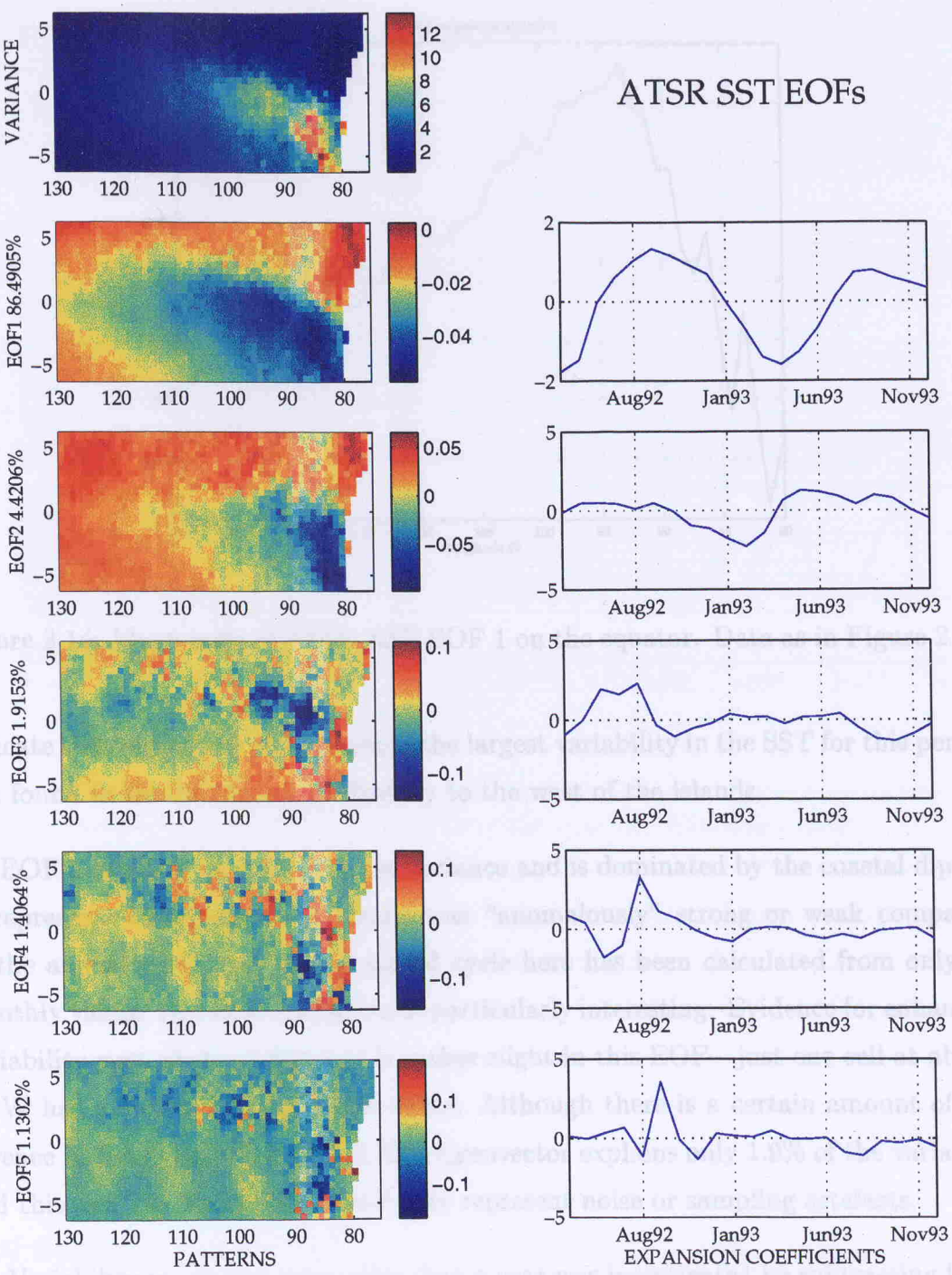

Figure 2.13: Variance and first five EOFs of the series of monthly composite ATSR SST maps of the equatorial east Pacific, April 1992–December 1993 inclusive. Percentage of variance explained by each EOF is shown on the vertical axis of each pattern. The timeseries in the right-hand column are the expansion coefficients (*i.e.*, for any month, the coefficients in an expansion of the original SST field in terms of the EOFs), normalized to unit variance (which is standard practice, see *e.g.* Bretherton *et al.* (1992)).

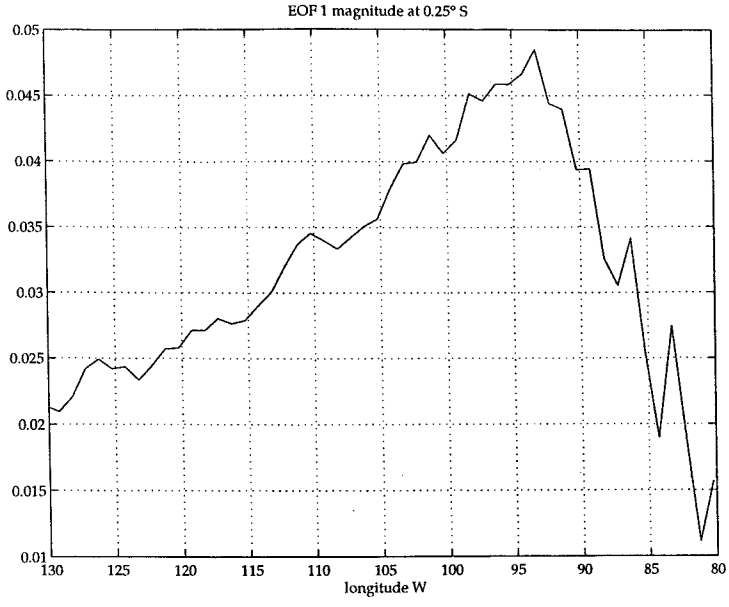

Figure 2.14: Magnitude of ATSR SST EOF 1 on the equator. Data as in Figure 2.13.

indicate that away from the mainland the largest variability in the SST for this period was found in the 1000km or so directly to the west of the islands.

EOF 2 explains only 4.4% of the variance and is dominated by the coastal dipole. It represents times when the dipole was "anomalously" strong or weak compared to the annual cycle, but as the annual cycle here has been calculated from only 21 monthly values, this observation is not particularly interesting. Evidence for enhanced variability west of the Galápagos is rather slight in this EOF—just one cell at about 91°W has a locally large absolute value. Although there is a certain amount of coherence in the pattern for EOF 3, this eigenvector explains only 1.9% of the variance, and this and the higher EOFs probably represent noise or sampling artefacts.

Variability on shorter timescales than a year was investigated by subtracting from the timeseries at each point a best-fit annual cycle obtained using least squares, and then calculating EOFs. As shown in Figure 2.15, the leading eigenvector corresponds to an approximate *semi*-annual cycle superposed on a general downward trend in the coefficients (upward trend in SSTs, given that the pattern values are negative) which probably reflects the transition from "normal" to weak El Niño conditions during the late summer of 1992. This signal is largely coherent across the entire eastern cold

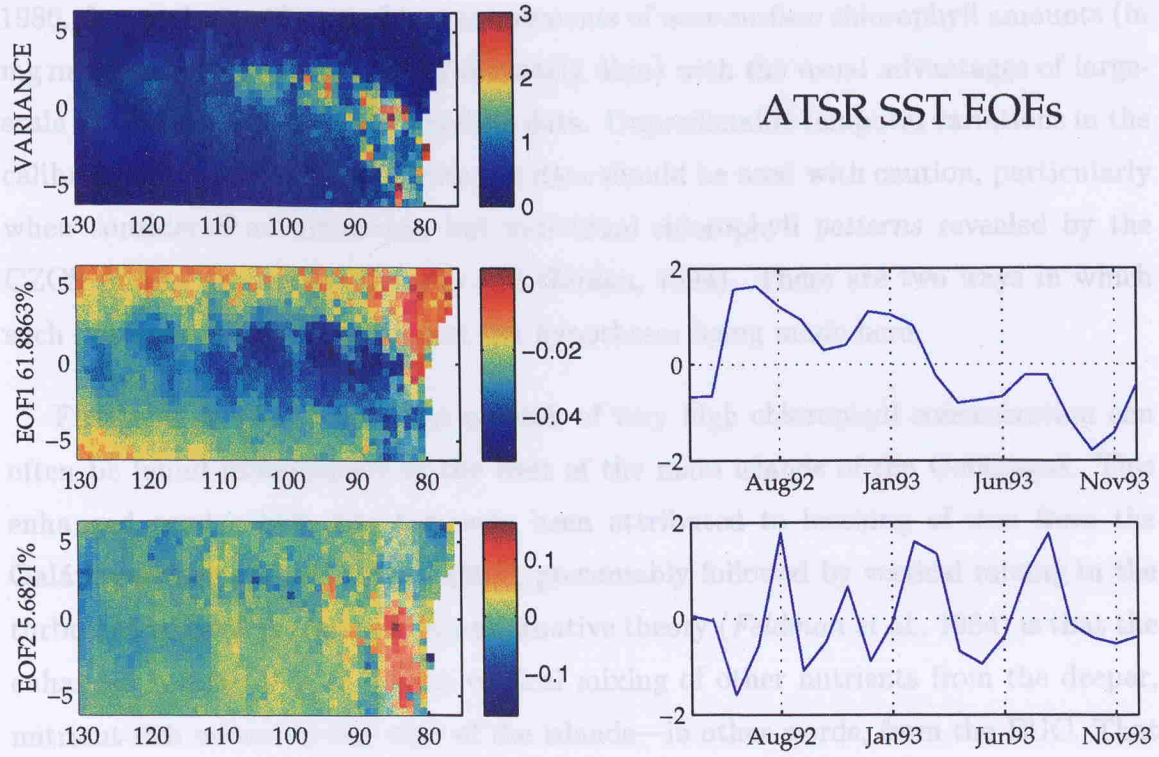

Figure 2.15: As per Figure 2.13 except that (i) a best-fit annual harmonic was removed prior to calculating the EOFs, and (ii) only the first two EOFs are shown.

tongue region to about 83°W, and does not show any sharp change at the longitude of the Galápagos. A semi-annual cycle is what would be produced if the SSTs in the region responded solely to the local solar forcing (since the Sun crosses the equator twice during the year); there is also a small peak at a period of 6 months in the Fourier spectrum of the entire 44-month timeseries of SSTs averaged over the cold tongue (92°–100°W, 2°S–2°N; spectrum not shown). EOF 2 reflects the variability off the Ecuador/Peru coast noted earlier, though in this diagnostic there appears to be a 3- or 6-month periodicity. Again the higher order EOFs show no coherent structures and are probably associated with noise.

2.2.2 CZCS chlorophyll images

The Coastal Zone Color Scanner (CZCS) was a multi-channel visible sensor flown on board the NASA Nimbus 7 satellite and operational from November 1978 until June

1986. It was designed to enable measurements of near-surface chlorophyll amounts (in $\mathrm{mg\,m^{-3}}$) at high resolution (approximately 4km) with the usual advantages of large-scale synopticity possessed by satellite data. Unpredictable temporal variations in the calibration mean that the quantitative data should be used with caution, particularly when considered as timeseries, but individual chlorophyll *patterns* revealed by the CZCS images are reliable (*Evans and Gordon*, 1994). There are two ways in which such patterns may be used to test the hypotheses being made here.

Firstly, it is well known that a patch of very high chlorophyll concentration can often be found immediately to the west of the main islands of the Galápagos. This enhanced productivity has famously been attributed to leaching of iron from the Galápagos shelf (*Martin et al.*, 1994), presumably followed by vertical mixing in the turbulent wake of the islands. An alternative theory (*Feldman et al.*, 1984) is that the enhanced productivity is due to vertical mixing of other nutrients from the deeper, nutrient-rich waters to the west of the islands—in other words, from the EUC. That vertical mixing is produced near islands is intuitively plausible and evidence for it has been observed *e.g.* by Hogg (1972), near Bermuda, and by Houvenaghel (1978) and Steger *et al.* (1998) near the Galápagos themselves. These authors have all observed either low Richardson numbers, or the "staircase" patterns in high-resolution vertical profiles (of temperature or other parameters) which are characteristic of the aftermath of Kelvin-Helmholtz (shear) instability, or both, associated with topographic features of the islands.

However, both observations—especially Houvenaghel's—and the model output presented in Chapter 3 suggest that the EUC waters reach the surface by upwelling, in the sense of upward displacement of isopycnals, rather than purely by mixing as such. Hence the presence of high chlorophyll concentrations to the west of the islands can be taken as evidence of such topographically induced upwelling.

The second way in which CZCS images may be used in the present context is by considering the phytoplankton as a passive tracer, albeit a highly non-conservative one. In particular, if phytoplankton generated in the upwelling region is diffused or advected beyond the north and south tips of Isla Isabela, and if the island tip jets exist, then two streamers of high chlorophyll to the west of the islands can be

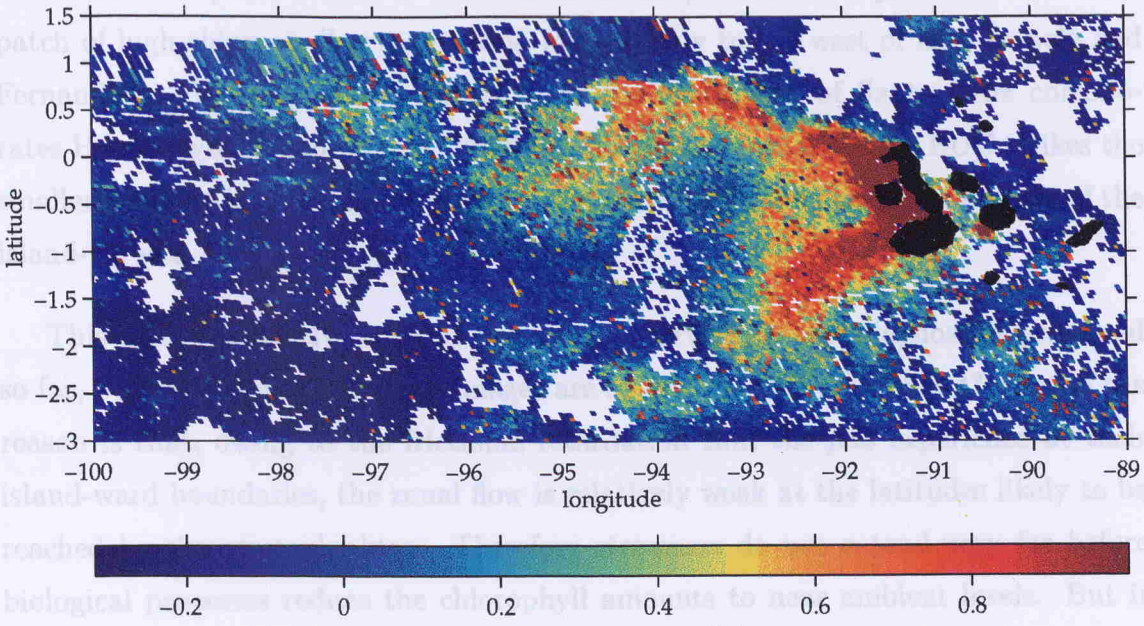

Figure 2.16: CZCS image for 2 November 1979. Colour scale is $\tanh(c - c_m)$ where c is the chlorophyll amount in $\mathrm{mg\,m^{-3}}$ and c_m is the mean of c over the non-blank pixels in the image. Note that this may not be perfectly navigated. The images in the level 2 browse products, of which this is one, are somewhat distorted. An attempt to correct for this has been made here by applying an affine transformation of the underlying grid such that three points on the island of Isabela, which can be identified from the pattern of blank pixels when the island is cloud-free, are correctly located.

expected. Conversely, the existence of such streamers provides confirmation of the presence of the jets.

The entire sequence of CZCS images including the Galápagos, which is freely available over the internet[16], has been examined. A single plume of high chlorophyll to the west or south-west of Isabela is often found, as in the classic image presented by Feldman *et al.* (1984) and Martin *et al.* (1994). Occasionally, however, a divided plume or pair of streamers can be observed. The best example I have found is shown as Figure 2.16, which is the image for November 2nd 1979. As argued earlier, this is the time of year when both upwelling and jets are likely to be most pronounced, except during El Niño; conditions were "normal" or weak El Niño at the time of this image.

[16]http://daac.gsfc.nasa.gov/data/dataset/CZCS/index.html

All of the expected features can be seen in this picture. Firstly, there is the usual patch of high chlorophyll concentration immediately to the west of Islas Isabela and Fernandina. Secondly, a smaller patch to the south-west of Santa Cruz corroborates Houvenaghel's finding that upwelling also takes place when the EUC strikes the smaller islands. And thirdly we have the two streamers indicating the presence of the island-tip jets.

This image evidently confirms the other observations and diagnostics presented so far, but we may ask why such images are so rare in the CZCS record? Part of the reason is that, owing to the frictional retardation that the jets experience at their island-ward boundaries, the zonal flow is relatively weak at the latitudes likely to be reached by the phytoplankton. Therefore streamers do not extend very far before biological processes reduce the chlorophyll amounts to near ambient levels. But it is more likely that the patch of water fertilised by the upwelling of the EUC only rarely extends beyond the latitudes of Isla Isabela. Such an extension presumably occurs only when the EUC is particularly strong and shallow, so that its impact on the islands causes a particularly marked horizontal as well as vertical spreading near the surface. Unfortunately the TAO record does not go back far enough to test this assertion for the case of the image presented here.

Nevertheless, the existence of such images lends further support to the island jet hypothesis.

Chapter 3

Diagnostics from the Main Run of OCCAM

3.1 The model and how it was driven

OCCAM ("Ocean Circulation and Climate Advanced Model") (*Webb et al.*, 1998a) is a global, primitive equation[1] Eulerian ocean general circulation model of the Bryan-Cox-Semtner type[2]. In the horizontal it uses the Arakawa B grid (*Mesinger and Arakawa*, 1976) in which tracer and velocity grid points are staggered, with coastlines passing through velocity points. The main numerical innovations in OCCAM are in the advection scheme (*Webb et al.*, 1998b) and in the treatment of the free surface (after Killworth *et al.* (1991); traditional Bryan-Cox-Semtner models use a rigid lid). The major logistic innovations are the use of a rotated grid for the North Atlantic and Arctic Oceans (*Coward et al.*, 1994; *Webb et al.*, 1998a) (to avoid the problem of vanishing zonal grid length at the North Pole which a regular latitude-longitude grid has), and the division of the ocean into a number of domains to enable the model to be run efficiently on high performance array processor computers (*Webb*, 1996; *Webb et al.*, 1997). The model's resolution is 0.25° in both latitude and longitude on the unrotated grid which covers the Pacific, and similar on the rotated grid; that is, the grid spacing is about 28 km in each direction at the equator. This is fine enough

[1] That is, based on the full Navier-Stokes equations simplified by the hydrostatic, Boussinesq and incompressibility assumptions.

[2] *I.e.* depth z rather than density ρ is used as the vertical co-ordinate; OCCAM is a "level" rather than a "layer" model.

to resolve equatorial dynamics—28 km is considerably less than a typical equatorial Rossby radius (cf. p.3 or Table 3.1), and at the surface the Galápagos, as represented in the model, have a north-south extent of four tracer grid points or five velocity grid points.

The model was initialised to a state of rest, with potential temperature and salinity derived from the Levitus 82 annual average dataset. It was then spun up for a period of eight $365\frac{1}{4}$-day years. During the first four years salinity and temperature at all levels were relaxed towards the annual mean Levitus values (with Levitus 94 values being used from day 180 onwards); thereafter the surface values only were relaxed to monthly mean Levitus 94 values, linearly interpolated in time, with a time scale of 30 days. Dynamical forcing was provided by monthly composite wind stresses from the years 1986–1988 inclusive, again linearly interpolated in time, derived from the ECMWF climatology. These wind stresses were ramped up linearly from zero over the first 60 days. A further $6\frac{1}{2}$ years of "production run" were then carried out, finishing at May 29th of model year 14 (day 5262). Instantaneous fields of SST and surface salinity are available for every two model days throughout the run. Global three-dimensional fields are available every 15 days, with a subset for the equatorial Pacific being available every three days for the year 8th January year 10 (day 3660) to 8th January year 11 (day 4026) inclusive.

In this chapter are presented some of the diagnostics from this main run of OCCAM which first led me to suspect that the Galápagos were having medium-to-large scale effects on the near-surface properties of the equatorial east Pacific, plus some further diagnostics extracted in response to these preliminary observations. Some of these diagnostics pertain to the question of how far the apparent effects are due to or implicit in the forcing applied to the model, but it is worth taking a look at the forcing fields to get an *a priori* feel for this.

Figure 3.1 presents anomalies of the u-component of the wind at the TAO mooring at 110°W on the equator[3] from the long-term mean annual cycle at that location[4].

[3]This is the mooring closest to the Galápagos that has wind data at this time.

[4]These *in situ* winds are presented, rather than the wind stresses as used in OCCAM, because it is easier to calculate the anomalies for this variable (Figure 3.2 shows the spatial distribution of the ECMWF winds used in OCCAM). The composite annual cycle of the TAO winds is similar to

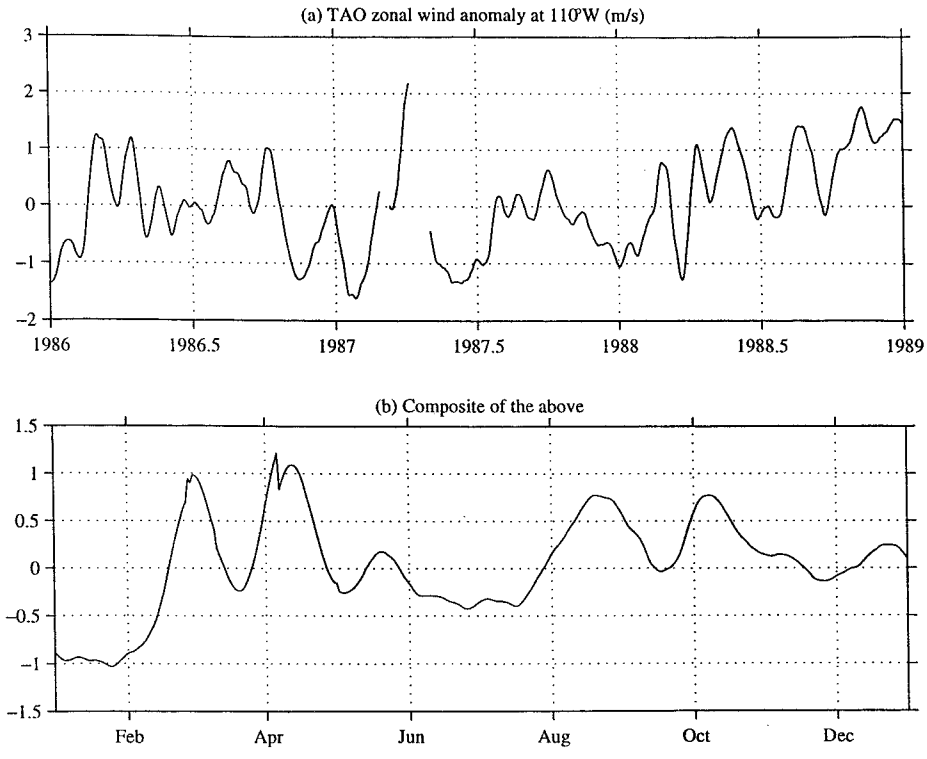

Figure 3.1: Zonal component of TAO wind at 0°N, 110°W for years 1986–1988 inclusive (the period from which the winds used to force OCCAM were obtained). (a) Anomaly of zonal wind in m s^{-1}, smoothed with a 31-day triangular filter, from a best-fit annual harmonic of the smoothed record for the entire period covered at that mooring. (b) Composite annual cycle of the series in (a).

The more positive the anomaly in this figure, the more westerly (eastward) is the wind with respect to this cycle, and conversely. Climatological winds at this location are south-east Trades which undergo an annual cycle in response to the meridional excursions of the ITCZ. The u-component in the smoothed annual composite TAO winds is always towards the west, with a maximum magnitude of about 5 m s^{-1} in September and a minimum of about 2 m s^{-1} in April, when the ITCZ is at its furthest south. The v-component is always to the north, and is of magnitude between 2.5 and 3 m s^{-1} except during February–June, when it dips to a minimum of about 0.5 m s^{-1} in late March. SSTs follow the zonal wind closely, in keeping with the naïve theory that the stronger the easterly component of the wind, the more Ekman divergence and upwelling occur at the equator, and the lower will be the equatorial SST. Thus

that of the OCCAM stresses—this being unsurprising since the TAO winds will have been given a large weight in the computation of the ECMWF analysed winds.

the smoothed annual composite TAO SST at this mooring reaches a maximum of 26.5°C in April, and a minimum of 22.5°C in August–September, with the Levitus SSTs used to force the model undergoing a similar cycle at this location (maximum 27.1°C in April, minimum 22.6°C in August).

Referring back to Figure 3.1, the easterly winds used to drive OCCAM were broadly speaking weaker than the climatology during March and April, and again during August through October. Hence the local wind forcing can be expected to produce a less pronounced autumnal cold tongue than normal, making any effect of the Galápagos more likely to show up against the climatology. Equally, the spring extinction of the cold tongue can be expected to be more complete. Likewise the stronger-than-normal easterlies during June–July and January–February may be predicted respectively to initiate the cold tongue earlier, and to maintain it for longer, than normal. As an aside we may note that there is no very strong signal in Figure 3.1 of the 1986–87 El Niño or the subsequent La Niña. Naïvely we might expect a weaker Walker cell, and weaker trades, during El Niño, and stronger ones during La Niña. If anything the opposite is the case in the data of Figure 3.1(a). Hence, and because of the composite (non-El Niño) SST forcing used (see below), we can expect a cold tongue to be maintained despite the integration nominally covering a period containing an El Niño.

Equatorial currents also respond to the seasonal cycle in the trade winds (*Philander*, 1990, pp.74–5). Both the directly driven Yoshida-type South Equatorial Current (SEC) and return flows such as the North Equatorial Countercurrent (NECC) intensify during the northern summer. Shear between these currents increases correspondingly, with the result that the TIW season is at its peak during the northern autumn. During the period of weak trades, the SEC likewise weakens and may even reverse, though this is partly due to the effects of the (remotely driven) seasonal Kelvin wave mentioned in Section 2.1.1. So, with reference to the previous paragraph, we might predict that in the annual cycle of OCCAM the SEC will strengthen earlier and last longer, but not become as intense, as in the climatology of the real ocean[5]; and similarly for TIWs.

[5]Subject, that is, to the fact that the speed of an accelerating jet is eventually limited by nonlinearity and/or instability (*Philander*, 1990, Section 3.3).

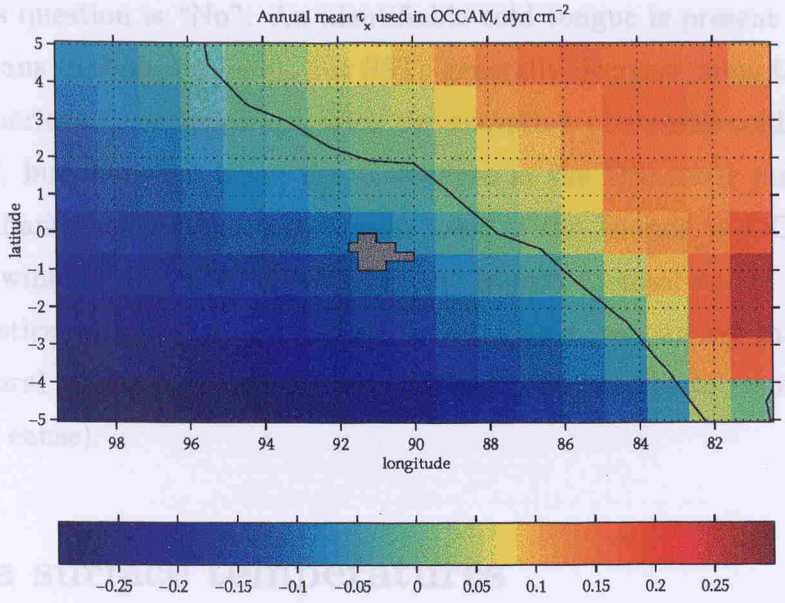

Figure 3.2: Annual mean of zonal component of wind stress (τ_x) from ECMWF winds used to drive OCCAM. Units: dyn cm^{-2}. A zero contour has been plotted; the winds are westerly to the east of this line, and easterly to the west. The grey polygon is the model's representation of the Galápagos.

Figure 3.2 gives an indication of the spatial distribution of the wind forcing. In the present context, the important thing to note is that the contour of zero zonal wind in this annual mean passes to the east of the Galápagos. This is also true for all but one of the twelve monthly fields used to represent the time variation of the forcing. In the 1.125° resolution uninterpolated ECMWF data, the western limit of westerly winds on the equator varies between 85.5°W in January, May and March, and 88.875°W in November. Only in February are westerly winds found to the west of the islands (the limit being 97.875°W for this month). Hence, for most of the year, if the eastern limit of the cold tongue in OCCAM were determined by the wind, then this limit would be to the east of the Galápagos. Conversely, if there is a sharp cutoff of the cold tongue at the islands, we can be sure that the islands themselves are exerting an influence. We shall see the latter to be the case, and further confirmation will be supplied by the numerical experiments of Chapter 4.

The main issue concerning the *thermal* forcing of the model is whether the putative effect of the Islands is already present in the Levitus 94 SST climatology. The short

answer to this question is "No". An identifiable cold tongue is present in the June–December means (not shown here), but SSTs generally decrease monotonically from the South American coast westward, with the exception of a small cold patch to the south-west of, but detached from, the Galápagos in the December mean[6]. So any pattern of enhancement of the cold tongue west of the Islands in OCCAM is due either to the wind forcing or to an effect of the Islands themselves. In view of some of the diagnostics presented in this chapter and the next, we can say that the spatial and/or temporal resolution of the Levitus dataset is too coarse to resolve this effect (whatever its cause).

3.2 Sea surface temperatures

3.2.1 Snapshots and Sequences

The best way to get a qualitative idea of the temporal development of the SST field near the Galápagos is to view an animation thereof. An MPEG file with one year's worth of SST pictures, taken at 2-day intervals between 30th December year 8 and 17th December year 9 of the main OCCAM run, has been created. Apart from the TIW observations noted in section 3.4 below, this animation also clearly shows the cold patch west of the islands extending westwards, thereby apparently enhancing the cold tongue. In fact, it was in this animation that I first noticed this feature. The sequence of three successive SST fields presented as Figure 3.3 gives some impression of the kind of thing that can be seen. The westward extension of the 20°C isotherm over the 40 days spanned by this diagram is clear, and typical of periods when the cold tongue is strengthening. The tip of the 20°C isotherm moves westward at an average speed of 12 cm s^{-1} over the period covered by this diagram. This is slow for both wave processes (typical westward-propagating planetary waves having a group velocity of about 30 cm s^{-1} (*Philander*, 1990)[7]) and advection (u being typically 20 or 30 cm s^{-1} in this region at this time); whichever is responsible, it seems that the cooling is modulated by other processes such as lateral diffusion or vertical mixing/upwelling.

[6]Isolated equatorial cold patches also occur during the decaying and warm phases of the cold tongue, *i.e.* the months January–May.

[7]Though in principle the group velocity can vary from this value down to zero.

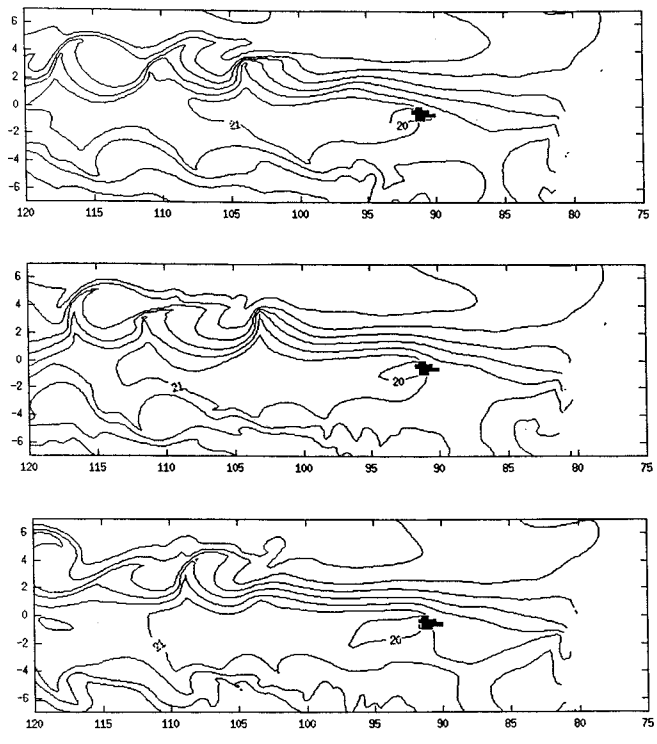

Figure 3.3: SST fields for OCCAM days 3490 (22 July year 9) (top), 3510 (11 August year 9) (middle) and 3530 (31 August year 9) (bottom). Contour interval is 1°C, and the 20°C and 21°C isotherms have been labelled. The black polygon is the model's representation of the Galápagos.

It is also noteworthy that the westward extension takes place mainly *between* the equator and 2°S, the latitudes at which the TAO moorings are situated. This might help to explain why it is difficult, though not impossible, to find evidence for westward propagation of the cold tongue in the TAO record (cf. section 2.1.3). We might predict that moorings at, say, 1°S (and perhaps closer to the Galápagos) would more readily yield evidence of westward propagation in the SST record.

The apparent southward displacement as the cooling propagates away from the Galápagos is presumably due to the northward wind stress (cf. Philander (1990, section 4.8)).

Figure 3.4 presents a snapshot of the OCCAM SST for comparison with a compos-

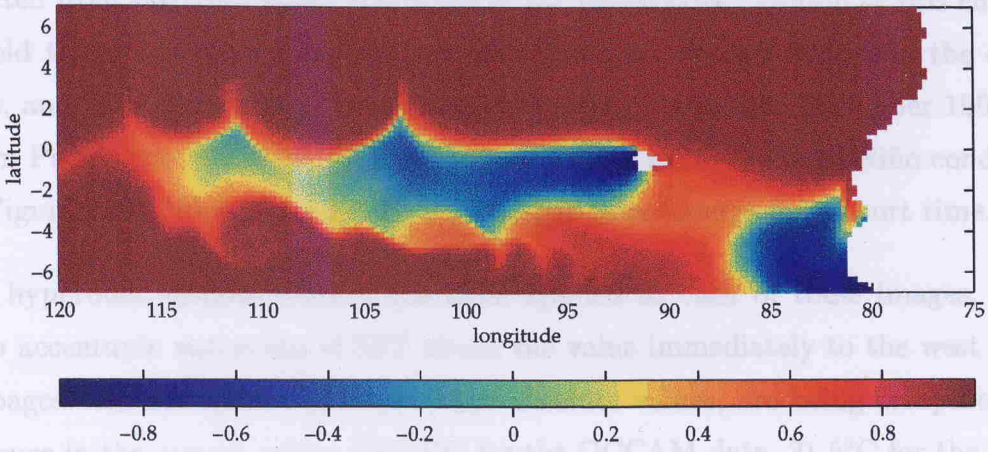

(a)

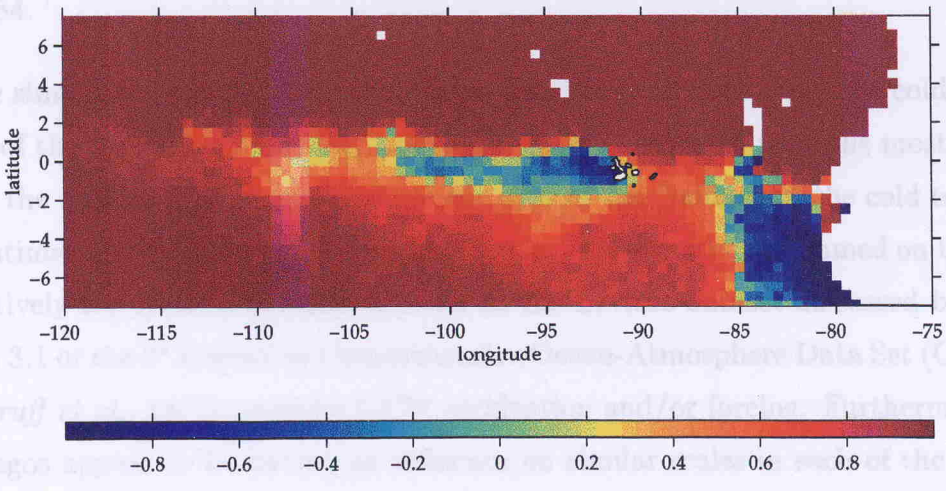

(b)

Figure 3.4: (a) OCCAM surface layer temperature for day 3510 (11th August, year 9). Colour axis is tanh(SST−20.75°C). (b) Composite ATSR image for December 1992. Colour axis is tanh(SST−21.5°C).

ite SST image from the ATSR satellite (see Section 2.2.1). Although the pictures are from different times of the year—August in the case of the model output, December for the satellite image—the pictures are comparable because they represent similar stages in the development of the cold tongue, namely an early mature phase. As predicted from the wind stress anomalies in the introductory section of this chapter, the cold tongue develops somewhat earlier in the model than it does in the climatology, and is in fact quite well established by early August. In December 1992, the eastern Pacific was experiencing a temporary respite from strong El Niño conditions (see Figure 2.12), which allowed the cold tongue to re-emerge for a short time.

A hyperbolic tangent stretch has been applied to each of these images, in order to accentuate variations of SST about the value immediately to the west of the Galápagos. As SST *patterns*, rather than absolute values, are being compared, the difference in the central values (20.75°C for the OCCAM data, 21.5°C for the ATSR data) is not important and indeed may be considered to be rather small given that the temperatures at the depths from which the water is (*ex hypothesi*) upwelled can vary by substantially more than this—for instance the temperature at 15 m in the TAO record for 95°W on the equator varies between 18.2°C and 29.5°C between 1981 and 1984.

The similarity between the two pictures is striking. In both cases the cold coastal waters of the Peru-Chile upwelling region are clearly separated from the most intense part of the cold tongue, immediately to the west of the Galápagos; the cold tongue is not continuous with the coastal upwelling region, as is sometimes assumed on the basis of relatively low-resolution datasets, such as the Levitus dataset discussed briefly in section 3.1 or the 2° resolution Comprehensive Ocean-Atmosphere Data Set (COADS) (*Woodruff et al.*, 1987), used for GCM verification and/or forcing. Furthermore, the Galápagos appear to be having an influence on similar scales in each of the images. In both cases one has to go at least 10 degrees of longitude (some 1100 km) west of the islands before encountering SSTs as low as those found immediately to the east thereof.

3.2.2 Statistics

EOFs from monthly mean OCCAM SST data have been calculated for comparison with the satellite data in Figures 2.13 and 2.15. The first four EOFs, explaining over 96% of the variance, represent a combination of the annual and semi-annual harmonics, with the annual cycle dominant (though not as strongly as in the ATSR data). Instead of presenting these EOFs, it is clearer to show the amplitudes A and phases ϕ of the harmonics in question. These are determined from a least-squares fit of the detrended series at each gridpoint to the function

$$A_1 \cos(\omega_1 t + \phi_1) + A_2 \cos(\omega_2 t + \phi_2),$$

in an obvious notation. This has been done at Figure 3.5.

That periodic variability is more pronounced in the model than in the satellite observations is unsurprising, because the model is being forced with a repeat annual cycle of surface fluxes interpolated from monthly mean climatologies[8]. The patterns of variability, however, are quite similar in the two datasets. In neither case does the large variability associated with the Peru-Chile upwelling region reach as far north as the equator, and in both cases it is separated from the Ecuadorian coast by a narrow tongue of lower variability where the sea surface tends always to be cool. Examination of individual monthly SST maps confirms that in both cases the region of cold water attains its maximum extent in the northern autumn and its minimum extent in the spring; in fact, the two datasets generally agree in having the annual cycle in phase over the whole region, apart from the area to the north of the equator where the variance is very small anyway.

The model also agrees with the observations in showing enhanced variability in the cold tongue west of the Galápagos, though this is clearer in the semi-annual cycle than it is in the annual cycle (because the largest amplitudes in the latter are in the coastal upwelling zone). Perhaps the most significant feature of the phase plot for the annual harmonic is that the phase decreases westwards from the Galápagos. SSTs reach their minimum later in the year the further west you go, indicating a signal propagating to the west in the cold tongue region. At 92°W the equatorial

[8] An integration with 6-hourly winds has since been performed, but is not considered here.

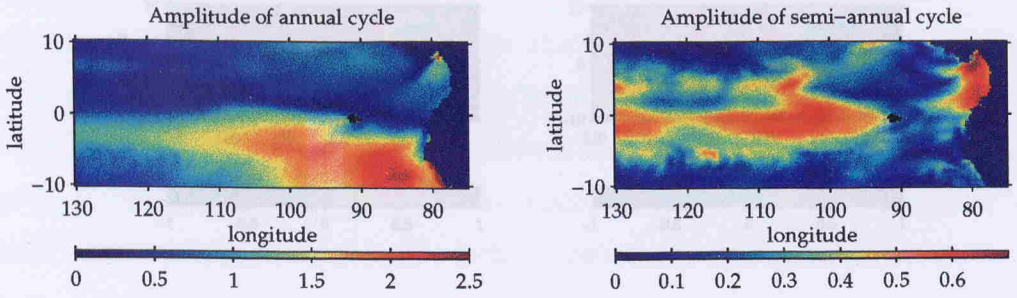

(a) Amplitudes in degrees C.

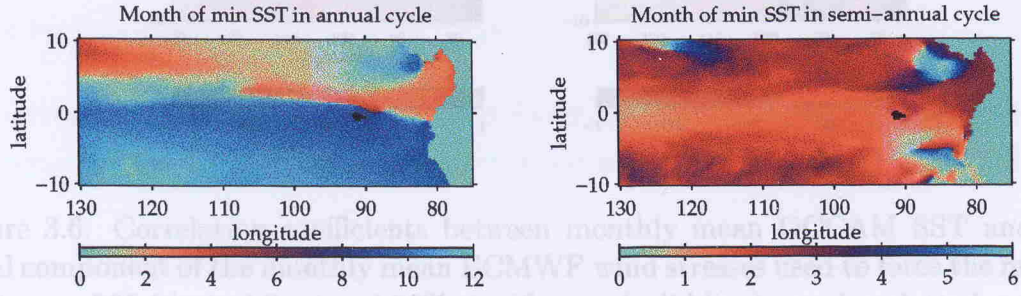

(b) Phases expressed as month of minimum SST.

Figure 3.5: (a) Amplitude and (b) phase of annual and semi-annual SST harmonics in OCCAM, from monthly mean data for January, year 8, to December, year 11, inclusive. Amplitudes are in degrees C. Phases are presented as time of minimum SST (so that, for instance, a value of 1 indicates the end of January), and a cyclic colour map has been used so that large changes in colour correspond to large changes in phase.

SST has its minimum on the 19th of October, whereas at 105°W this occurs 20 days later on the 8th of November (with an approximately linear decrease in phase in between), implying a propagation speed of about 82 cm s^{-1}. This is faster than the westward migration of the 20°C isotherm noted in the previous subsection, but within the bounds of possibility for an equatorial inertia-gravity ("Poincaré") wave, cf. section 2.1.3. An unexpected feature of this diagram is that the phase of the annual cycle also decreases to the *east* of the Galápagos, the minimum occurring on the 17th of September at 89°W and the 21st of December at 86°W. This makes the implied propagation speed much slower, about 4 cm s^{-1}.

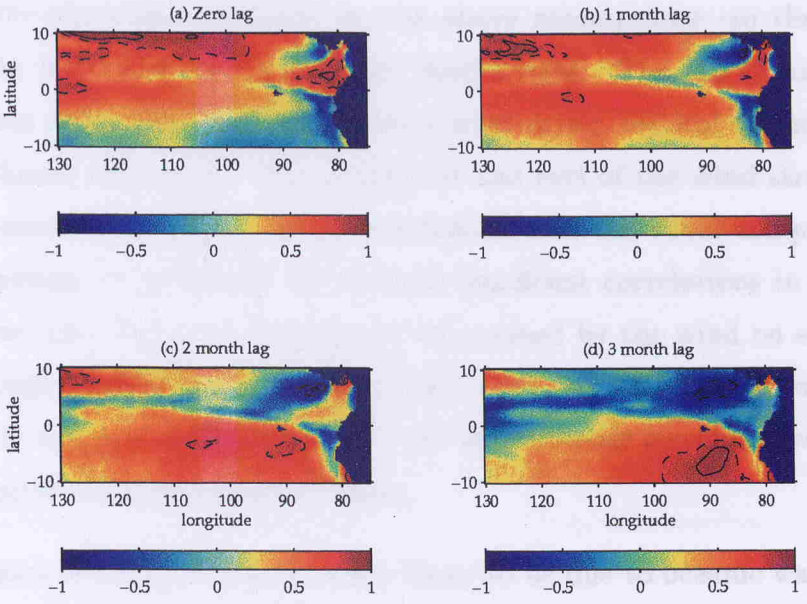

Figure 3.6: Correlation coefficients between monthly mean OCCAM SST and the zonal component of the monthly mean ECMWF wind stresses used to force the model. Contours of 95 (dashed line) and 99% significance (solid line) are also plotted, assuming 4 degrees of freedom (for reasons explained in the text).

3.2.3 Correlations with forcing

The suggestion that SSTs in the cold tongue are significantly modified by the presence of the Galápagos has to be defended against the hypothesis that the cold tongue is produced purely by the wind and consequent Ekman divergence at the equator. To this end I have calculated correlations between the SSTs in the equatorial east Pacific of OCCAM and zonal component of the wind stresses used to force the model.

Figure 3.6 displays the correlation coefficients with the wind leading the SST by 0, 1, 2 and 3 months. A typical integral time scale for this calculation was 5 months, as calculated by the method of Davis (1976). This implies that the relevant number of degrees of freedom is only 2 or 3. The figure indicates the regions where the correlation is significant at the 95% and 99% levels assuming 4 degrees of freedom; this errs on the pessimistic side given that we are trying to establish a *lack* of correlation here. A positive correlation is expected in the cold tongue region, where eastward (negative) winds lead to cooling, and this is what we see at zero lag. However, the correlation

is not perfect—not even *significant* on the above assumptions—so there is plenty of variance to be accounted for by other mechanisms. The larger correlations in other locations will be due variously to local wind-driven vertical mixing and extra-equatorial Ekman dynamics[9]. The magnitude and curl of the wind stress are basic to these processes respectively, but a correlation with the zonal component is not unlikely. Anyway, to re-iterate, the lack of significant correlations in the zero-lag diagram shows that SSTs are not entirely determined by the wind on seasonal time scales (although calculations using daily TAO wind and SST data shows that SST, and especially the *rate of change* of SST, are very strongly correlated with the wind stress on shorter timescales of a few days).

Correlations at non-zero lag are more likely to be due to oceanic wave processes, *i.e.* remote rather than local forcing, so that one would typically need to use spatial as well as temporal lags in order to identify them. Nevertheless, the dipole of correlations antisymmetric about the equator at a lag of three months may be due to waves that have been reflected off the South American coast—such waves can just be made out in the equatorial SST diagram of Figure 3.20. However, this takes us too far from our main objective.

3.3 Trajectories

As noted in earlier chapters, two of the questions being addressed in the present study are the origin of the cold tongue waters west of the Galápagos, and the fate of the EUC when it strikes the islands. One way of attacking this problem with the help of OCCAM is to calculate particle trajectories. Because of limited computing resources, it is not feasible to re-run the model with added particle tracking code; instead, an off-line trajectory program has been developed.

[9] We should not neglect the fact that 1 and 5% of the area can be expected to show significant correlations at the 99 and 95% levels respectively, by chance, nor that *spatial* autocorrelations/integral scales can also enlarge these regions.

3.3.1 Methods

Three different types of trajectory can be calculated: at single model levels, on isopycnal surfaces, or using a fully three-dimensional velocity field. The latter probably gives the most realistic trajectories and will be described in the most detail here.

For purposes of realism it is generally preferable to use time-varying fields (rather than constant or time-averaged fields) in off-line trajectory calculations; this becomes essential at times and in regions of, for instance, intense eddy activity. Therefore, model output is linearly interpolated in time and trilinearly interpolated in space so that the horizontal velocity $\mathbf{u}_H$ is available as a function of three-dimensional position $\mathbf{x}$ and time t. Vertical velocity w is diagnosed from the horizontal fields using the (incompressible) continuity equation, taking careful account of the variation of grid box area with latitude, the non-zero free surface displacement, and the interpretation of model velocity fields near bottom topography[10]. Values for w between grid points were again calculated by linear interpolation; in particular, the more sophisticated vertical interpolation methods recommended by Methven (1997) for use with off-line trajectory calculations in the atmosphere were not felt to be necessary with the much smaller vertical velocities encountered in the ocean. The hypothetical particles are then moved around using a fourth-order Runge-Kutta method. That is, if the timestep used is Δt and times t, $t + \Delta t/2$ and $t + \Delta t$ are denoted by subscripts n, $n + 1/2$ and $n + 1$ respectively, then we calculate

$$\mathbf{x}_{n+1} = \mathbf{x}_n + \frac{\Delta t}{6}(\mathbf{u}_1 + 2\mathbf{u}_2 + 2\mathbf{u}_3 + \mathbf{u}_4) \tag{3.1}$$

where

$$\begin{aligned}
\mathbf{u}_1 &= \mathbf{u}(\mathbf{x}_n, t_n), \\
\mathbf{u}_2 &= \mathbf{u}(\mathbf{x}_n + \mathbf{u}_1\Delta t/2, t_{n+1/2}), \\
\mathbf{u}_3 &= \mathbf{u}(\mathbf{x}_n + \mathbf{u}_2\Delta t/2, t_{n+1/2}) \text{ and} \\
\mathbf{u}_4 &= \mathbf{u}(\mathbf{x}_n + \mathbf{u}_3\Delta t, t_{n+1}).
\end{aligned}$$

An option for calculating back-trajectories also exists; this is basically the same as the above but with Δt replaced by $-\Delta t$. The code was checked by running a set of

[10]The routine to calculate w was adapted from code supplied by Andrew Coward.

trajectories forwards and then backwards in time, to verify that they ended up where they had begun.

This is a tried and trusted method for off-line trajectory calculations (*Methven*, 1997), and allows relatively long time steps to be used. For instance, in a test involving 756 46-day back trajectories terminating in the cold tongue region between 95°W and 100°W, a run with $\Delta t = 1800$s took 45 minutes of cpu on a certain computer, whereas a run with $\Delta t = 60$s took $19\frac{1}{2}$ hours. The results were indistinguishable by eye, though plots of the difference trajectories revealed displacements between the two runs. Typical displacements appeared to be of order 1 km or less, with an occasional trajectory pair diverging by more than this[11]. This is encouraging; we would expect slight differences to arise between the two runs because of rounding error, and the subsequent relatively large divergence of a small number of trajectory pairs suggests that we are capturing something of the chaotic behaviour of trajectories in the real ocean.

Originally the program used a "no-slip" boundary condition, *i.e.* $\mathbf{u}$ was assumed to be zero at solid earth grid points and the zero values were used in the interpolation. This, however, led to the model coastlines acting as "particle attractors"—trajectories tended to be drawn into the coast, where they are terminated, whenever they came within one grid length of a solid earth point. To circumvent this, a "free slip" boundary condition was implemented, wherein the normal component at boundary points was kept at zero, but the tangential component was set, normally, to half the value at the neighbouring oceanic grid point. One could justify this choice by arguing that tracer grid points are considered primary in the model, but lie inside the coastline as defined by zeroes of velocity, therefore it is legitimate to use a non-zero value of $\mathbf{u}$ on the boundaries in this context. Reducing the tangential component by a factor of 1/2 is a crude way of representing a sub-grid scale lateral boundary layer. The horizontal viscosity used in OCCAM, 200 $m^2\ s^{-1}$, is an eddy viscosity appropriate to the open ocean. As a lateral boundary is approached the size of the "allowed" eddies will decrease, so that the effective eddy viscosity will also decrease, and there-

[11]The mean and standard deviation of the displacements in x, y and z at the end of the run were respectively (−0.49, 3.01) km, (3, 876) m and (1, 55) cm, the means of the *absolute* displacements being 0.87 km, 0.18 km and 55 cm.

fore a boundary layer of indefinitely small thickness, in particular smaller than can be resolved by the model grid, is possible. This is consistent with the pragmatic philosophy of the program, which aims to generate realistic trajectories even if this means sometimes being inconsistent with some of the definitions used in the model. Another example of this is the use of linear interpolation in space; the model's tracer advection scheme assumes **u** to be piecewise constant, and therefore discontinuous at boundaries between grid boxes.

At corner points on the boundary, both components of velocity are set to zero. This is necessary to prevent trajectories passing through solid earth. For instance, if u were set non-zero at a corner point, interpolation between this value and the zero u at a neighbouring boundary point to the north or south would produce a non-zero u on the boundary in between. This u could well be directed into the boundary, causing trajectories to pass inland[12]. It was found that setting u to zero at corner points did not cause these to act as attractors. Some trajectories can still become grounded, but this is not unrealistic—real Lagrangian drifters are frequently washed ashore! If anything, the program now errs in the opposite direction, with some trajectories sliding along the model coastline when grounding might be more realistic.

For the calculation of isopycnal trajectories (such as might mimic the behaviour of a Lagrangian drifter kept at constant density), the potential density σ_θ is also extracted as a function of time and position. Because the input data are archived for particular times, rather than, for instance, as means over the interval between successive dumps, the density profiles can be gravitationally unstable. When this occurs, the profile is "convectively over-adjusted" to be marginally stable. The adjusted density then increases strictly with depth and can therefore be inverted to give depth as a function of potential density, as required. Particles are advected around using a 4th order Runge-Kutta scheme applied to the u and v components only, interpolated vertically onto surfaces of constant density. Because of the extra interpolations, isopycnal runs take eight or nine times as long as those using three-dimensional velocities.

Isopycnal trajectories tend to undergo implausibly large vertical excursions when

[12]In runs of the program where free slip conditions were imposed at corner points, the trajectories would often pass right through the solid earth points and emerge at the other side of the island.

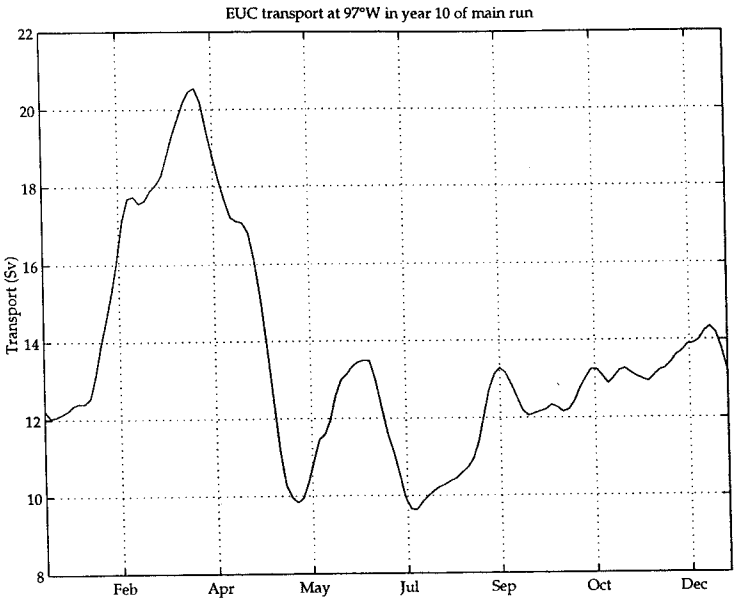

Figure 3.7: EUC transport (as defined in the text) for year 10 of the main run, at 97°W. 3-daily data with no smoothing.

they pass into the surface mixed layer. Accordingly, they have only been used to study sub-surface flows in the present work. Conversely, they may be considered to represent better the trajectories of drifters travelling below the surface layers; actual drifters (PALACE and the like) are usually designed to remain on constant density surfaces. Trajectories calculated using the full three-dimensional velocities may be taken to simulate a tracer release experiment, apart from the effects of sub-gridscale diffusive processes.

The trajectory program has been used to investigate two of the phenomena under consideration: the fate of the EUC as it strikes the Galápagos, and the origin of the cold equatorial waters east of the islands.

3.3.2 Results 1: Fate of the EUC

Two integrations were performed, both with a set of drifters injected at 97°W. This longitude was chosen to be close to the west coast of the islands, but far enough away for their influence not to be felt in the EUC. One integration was done when the EUC was strong, and the other when it was weak, to examine the behaviour at different

phases of the annual cycle. Suitable times were determined from the timeseries of EUC transport plotted as Figure 3.7. EUC transport is defined as the integral over the top 7 model levels (extending down to 182 m) of any positive (eastward) velocities between 2°N and 2°S inclusive. Visual inspection of the u fields for each day of the timeseries confirms that this was an appropriate choice; in particular, the EUC core was always at either level 4 or level 5 (76 and 102 m) and never strayed more than half a degree away from the equator.

The transport peaks sharply in the boreal spring, attaining a maximum value of 20.54 Sv on day 3741 (30th March year 10). It then falls off quite quickly to a minimum of 9.83 Sv at day 3792 (20th May) or to 9.64 Sv at day 3855 (22nd July), and recovers gradually during the rest of the calendar year, as in the composite annual cycle of Lukas and Wyrtki described in Chapter 2. A couple of subsidiary maxima in the transport occur later in the year in Figure 3.7; these are associated with seasonal Kelvin waves as discussed further below (section 3.5). The EUC core velocity undergoes a similar cycle, with a maximum of 97.7 $\mathrm{cm\,s^{-1}}$ on day 3738 (27th March) and a subsequent minimum of 64.6 $\mathrm{cm\,s^{-1}}$ on day 3795 (23rd May) at this longitude. Accordingly, the trajectory program was run for 150 days starting on 30th March of year 10 for the "strong EUC" case; and for 150 days starting on 22nd July for the "weak" case.

Figure 3.8 shows the set of initial positions chosen for these runs, superimposed on the zonal velocity at the start of the strong EUC run. The positions go from 1.5°S to 1.5°N at intervals of 0.05°, and from 60 to 120 m at 4-metre intervals, making a total of 976 drifters. As seen in the figure, this spans the two levels at which the EUC core is found, and the main latitude range of the current.

In Figures 3.9 and 3.11 are presented the trajectories originating on the equator, for the strong and weak cases respectively. These are typical of the trajectories of particles originating between about 0.5°S and 0.6°N, but show the salient features particularly clearly. Trajectories calculated using both the isopycnal version of the program and the version utilizing the full three-dimensional velocities are shown for comparison.

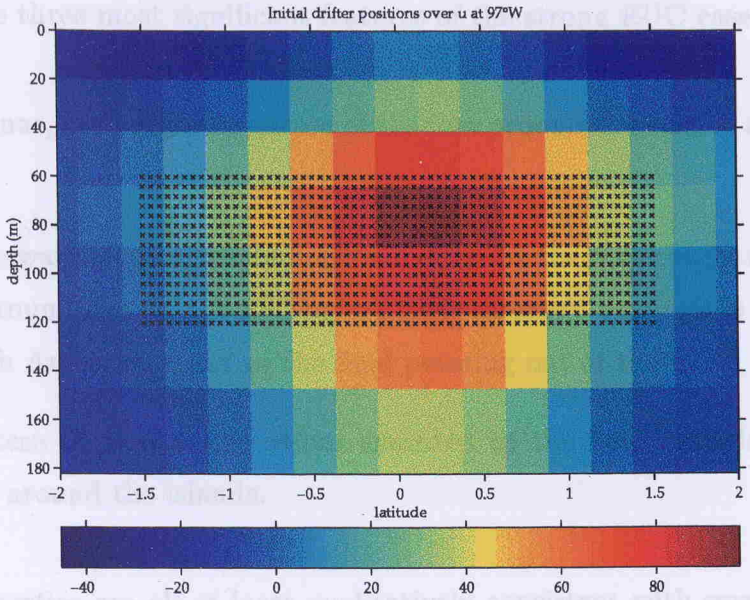

Figure 3.8: Initial positions of drifters for integrations of trajectory program used to investigate the fate of the EUC on encountering the Galápagos, superimposed on the u component of velocity at 97°W at the start of the "strong EUC" run. Velocities in $\mathrm{cm\,s^{-1}}$. Each x marks an initial position.

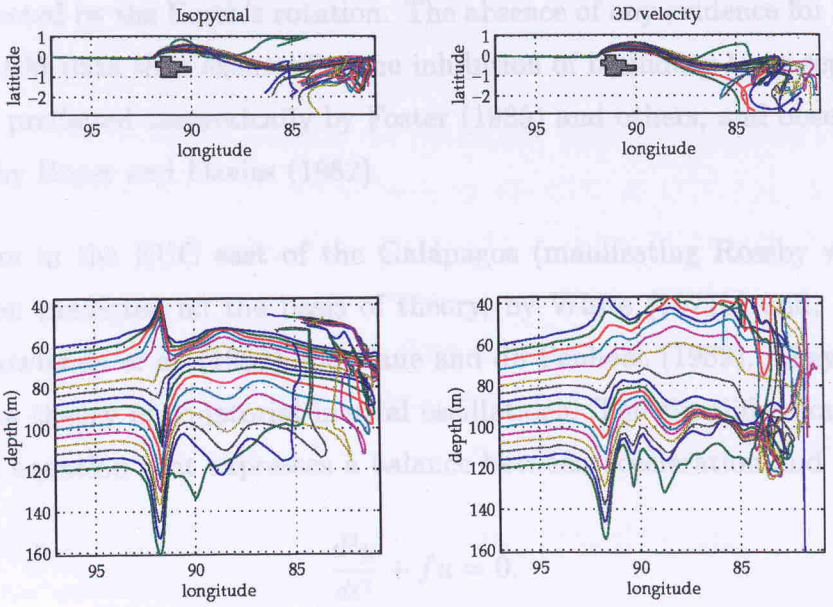

Figure 3.9: Trajectories beginning on the equator, for the "strong EUC" case discussed in the text. Top and side views for (a) isopycnal trajectories and (b) trajectories using full three-dimensional velocities.

Perhaps the three most significant features of the strong EUC case are:

1. The laminar, potential-like nature of the flow around the islands as viewed from above;

2. The large-wavelength meanderings undergone by the trajectories after they have passed around the islands and before their eastward progress is terminated by the South American coast or the final petering out of the EUC; and

3. The pattern of vertical excursions executed by the fluid particles as they flow into and around the islands.

These properties are all at least qualitatively consistent with several theoretical and observational studies of flow round equatorial islands. Firstly, the Reynolds number for the flow is between 100 and 500 depending on which upstream velocity one takes to be characteristic (and using the model's eddy viscosity in the denominator). At such values of Re one would expect to observe attached or even detaching eddies in a flow unaffected by the Earth's rotation. The absence of any evidence for such eddies in the OCCAM data thus exemplifies the inhibition of boundary layer separation on the β-plane predicted theoretically by Foster (1985) and others, and observed in the laboratory by Boyer and Davies (1982).

Meanders in the EUC east of the Galápagos (manifesting Rossby waves) have likewise been predicted on the basis of theory, by White (1971b) and, more rigorously, by Rowlands *et al.* (1982) and Cane and du Penhoat (1982). They also follow from a naïve theory of equatorial inertial oscillations. The simplified form of the v-momentum equation that expresses a balance between acceleration and the Coriolis force is

$$\frac{d^2y}{dt^2} + fu = 0. \tag{3.2}$$

Writing $y = R\theta$ where R is the Earth's radius and θ latitude, putting $\sin\theta \approx \theta$ close to the equator, and treating u as constant, for positive u equation (3.2) describes simple harmonic motion of angular frequency $\omega = (2\Omega u/R)^{1/2}$, period $T = 2\pi(R/2\Omega u)^{1/2}$ and wavelength $\lambda = uT = 2\pi(Ru/2\Omega)^{1/2}$, where Ω is the angular velocity of the Earth. Figure 3.10 shows T and λ as functions of u.

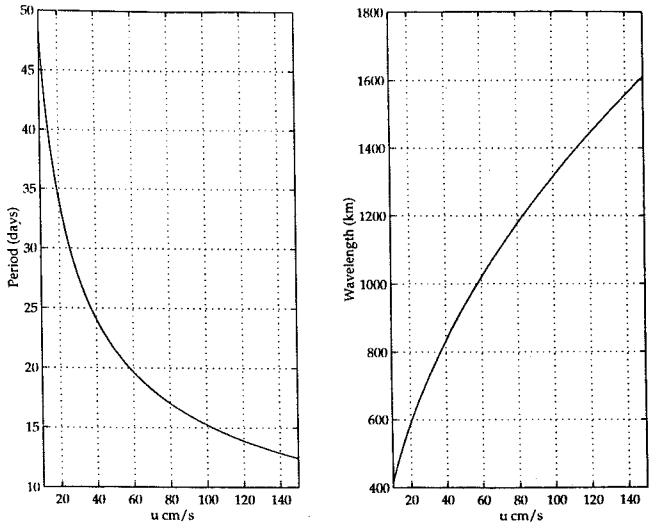

Figure 3.10: Period (left) and wavelength (right) of equatorial inertial oscillations as functions of zonal current u, assumed constant.

As noted in Chapter 1, such meanders have also arguably been observed in the wild by White (1973). That the particles in Figure 3.9 all follow similar trajectories, despite arriving east of the islands at different times, confirms that the wake is a (more or less) stationary wave rather than a time-varying Kármán-like phenomenon (*cf.* page 4). This stasis also vitiates the possibility that the meanders are related to the similar meanders observed further west in the EUC in OCCAM. The latter are associated with TIWs and propagate westwards at about 30 $\mathrm{cm\,s^{-1}}$. Animations of the EUC core velocity show that if anything the eastern meanders grow towards the east, away from the islands, during the time when the EUC is strengthening. These meanders are, however, sometimes modulated by westward-propagating disturbances of the type seen in this region in Figure 3.20 below and identified as TIWs.

Viewing a sequence of the core velocity diagrams also suggests that the wavelength of the meanders is smaller at the times when the EUC is weaker. This is consistent with White's prediction that the wavelength is proportional to the square root of the upstream velocity, which is also true of our naïve theory. However, this prediction is not quantitatively confirmed by the model; taking as a half-wavelength the zonal distance from the northmost point visited by a particle as it passes round the island to the point at which it next reaches a local minimum of latitude, a typical

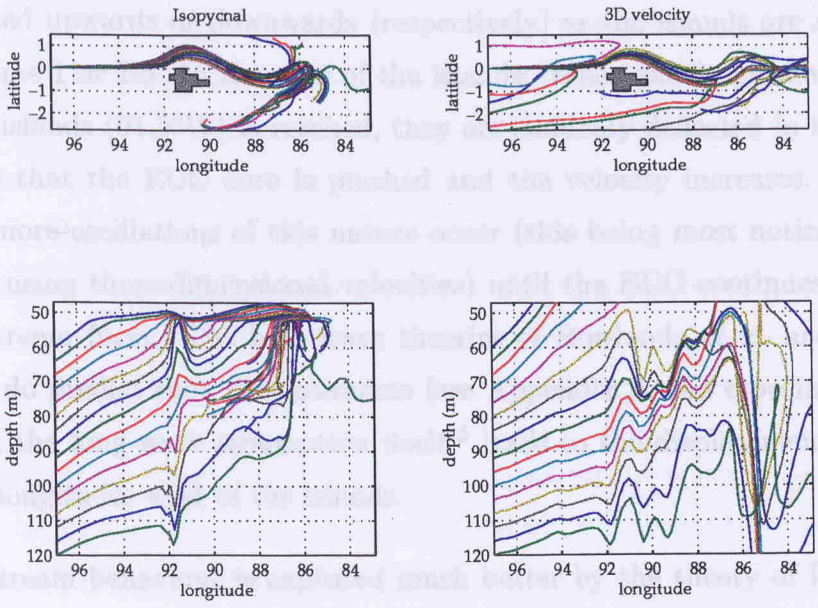

Figure 3.11: As Figure 3.9 but for "weak EUC" case.

wavelength in Figure 3.9 is about 930 km. For the weak EUC case of Figure 3.11 the wavelength is about 860 km, giving a ratio of 1.08. The square root of the ratio of the peak EUC velocities noted earlier is larger than this, at 1.23; and the ratio for the corresponding transports is larger still (1.45). Examination of the terms in the v-momentum equation suggests that the meanders are most likely to be inertial oscillations; the Coriolis acceleration is of a similar magnitude (order 10^{-6} m s^{-2}) or larger than the meridional pressure gradient acceleration, and is (of course) always restoring for this motion, whereas the PGF is consistently northward north of the equator and southward south of the equator.

The papers of Rowlands *et al.* and Cane and du Penhoat are based on linear inviscid theory which predicts that the wavelength decreases continuously with time, the eventual termination of this process by the non-linear and dissipative terms not being represented. Therefore they make no prediction concerning the wavelength that will actually be observed.

The third aspect of the trajectories that we drew attention to just now was the pattern of vertical displacements undergone by the particles on their journey around the islands. Figure 3.9 has particles originating above or below the core of the EUC

being deflected upwards or downwards (respectively) as the islands are approached, beginning some 1 or 1.5° to the west of the islands. When the longitude of the west coast of the islands (91.5°W) is reached, they are suddenly deflected in the opposite direction, so that the EUC core is pinched and the velocity increases. Thereafter one or two more oscillations of this nature occur (this being most noticeable in the calculations using three-dimensional velocities) until the EUC continues in a weakened downstream form. The long wave theories of Rowlands *et al.* and Cane and du Penhoat do predict such displacements (see Appendix A and especially equation (A.18)), but the long wave assumption itself[13] leads to the displacements being the same at all longitudes west of the islands.

The upstream behaviour is captured much better by the theory of Lamb (1932) and Drazin (1961) as applied by Hendry and Wunsch (1973). This theory is based on the time-independent, non-rotating, inviscid equations of motion and so the effects it predicts may be described as hydraulic or "Bernoulli". The equations of motion describe a balance between the non-linear or advective terms $\mathbf{u}\cdot\nabla\mathbf{u}$ and the three-dimensional pressure gradient force, and are solved to zeroth and first order in the reciprocal of the Richardson number. This formally requires the Richardson number to be large, which is only true of the OCCAM data (and the observations discussed by Hendry and Wunsch) in the vicinity of the EUC core; however, these authors found agreement with observations "despite the use of the theory outside its obvious range of validity". The zeroth order solution is a two-dimensional flow around the island(s), as might be expected from the stratification implied by a large Richardson number. At first order, however, trajectories originating above the level of zero vertical shear (*i.e.* the EUC core) are displaced upwards as the island is approached, and conversely for deeper trajectories. The maximum vertical displacements are of order

$$u\frac{du}{dz_0}/N^2$$

metres, where z_0 is the depth of the particle trajectory far upstream and N^2 the square of the Brunt-Väisälä frequency. For the OCCAM data this scale is about 60m at the levels adjacent to the EUC core (level 4). These maximum displacements are predicted at the coast of the island; the displacements decrease rapidly upstream, to

[13] Or, possibly, the assumption of linearity.

about 1/4 of the maximum value at a distance from the coast equal to the north-south extent of the island (for the elliptical island considered by Hendry and Wunsch). Referring to the previous paragraph, all this is clearly a good description of the behaviour of the OCCAM trajectories as they approach the Galápagos. (The maximum vertical displacements obtained, some 40m, are slightly smaller than predicted, but the trajectories in Figure 3.9 originate on the equator, which is the northern limit of the islands in this model. The displacements are largest for trajectories which hit the islands head-on.)

This hydraulic model also predicts vertical displacements in the opposite direction, of a similar magnitude to the original displacements, as the trajectories pass to the north and south of the land mass. Again this is observed in OCCAM. According to the alternative wave description, this part of the flow may be characterised as a pair of coastally trapped Kelvin waves (*cf.* page 5). Rowlands *et al.* conjecture that friction and non-linearity might lead to these jets separating from the island to form a two-core EUC downstream of the barrier. As noted in Chapter 2, this has occasionally been observed in the real ocean. It also occurs (rarely) in OCCAM, for instance on day 3801, when separate cores exist for some 400km to the east of the islands. The two currents usually reunite within a degree or so of the east coast, however.

Hendry and Wunsch predict, finally, that the EUC core should become more diffuse again for a short distance downstream of the islands—for their symmetrical island the displacement patterns are also symmetrical. Such a broadening is indeed seen in the trajectory data of Figure 3.9, although some of the trajectories calculated from the 3D velocity field show an additional kink as the particles pass round the north-eastern shoulder of the islands. Rowlands *et al.* also predict a thickening of the EUC core or thermocline to the east of the islands—in fact a sequence of thickenings and narrowings in the different phases of the island-induced Rossby wave. This offers an alternative explanation or description of this feature.

As we have already partially noted, the trajectory patterns for the time of year when the EUC is weak (Figure 3.11) are qualitatively similar to those for the strong EUC. Gross differences include the fact that the particle paths move upward more steeply and tend not to reach as far east. Both of these indicate that the EUC would

be surfacing anyway at these longitudes at this time of year, even if the Galápagos were not present. Differences between the two methods of calculation are also more marked in this set of trajectories. The isopycnal trajectories are all confined beneath the low-density surface layer, whereas several of the 3D trajectories eventually rise to the surface and are swept westwards by the SEC.

A few of the 3D trajectories also reach further east in the meandering tail end of the EUC. This observation is made more quantitative in Figure 3.12, which shows the percentage of trajectories attaining each longitude east of the starting position and is thus an indicator of the degree of eastward penetration of the EUC in the various cases. Each of the four scenarios discussed so far is represented, along with a fifth integration using 3-daily data and 3D currents for the strong EUC case, which shows that using the more frequent data makes little difference to this particular diagnostic at least.

The percentage of trajectories retroflected before reaching the longitude of the west coast of the islands (91.75°W in the model) is a quantity which is insensitive to the method of calculation. For all methods, about 30% of the particles fail to reach this longitude when the EUC is strong, the figure being closer to 50% when the EUC is weak. Thereafter the results are less similar, though the clear difference between the two times of year is robust.

As exemplified in Figure 3.13, most or all of the trajectories which fail to reach 91.75°W originate in the southern part of the EUC and are swept westward in the southern branch of the SEC. This figure also illustrates the potential-like nature of the flow round the islands, and that the bulk of the downstream-emerging EUC has taken the northern route round the islands. Taking these streaklines to approximate streamlines, the fact that the northern trajectories are closer together also shows that the northern flow is faster (as well as more voluminous) than the southern. Calculations of the transport in the two branches show that about 75% of the volume is transported in the northern branch, though this figure oscillates at the frequency of the Rossby-gravity waves noted below (page 82) as possibly nascent TIWs. During the spring maximum, the northern and southern branches carry about 12 Sv and 5 Sv, with peak velocities 80 and 50 $\mathrm{cm\,s^{-1}}$, respectively.

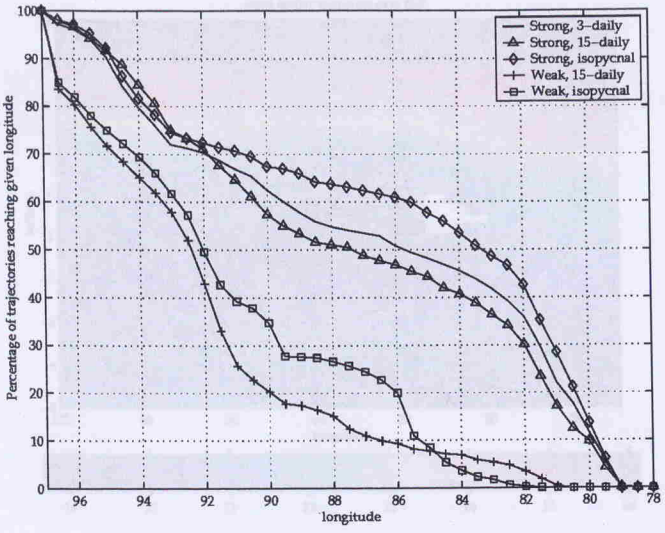

Figure 3.12: Percentage of trajectories reaching each longitude east of 97°W (the starting position) for each of the EUC trajectory scenarios described in the text.

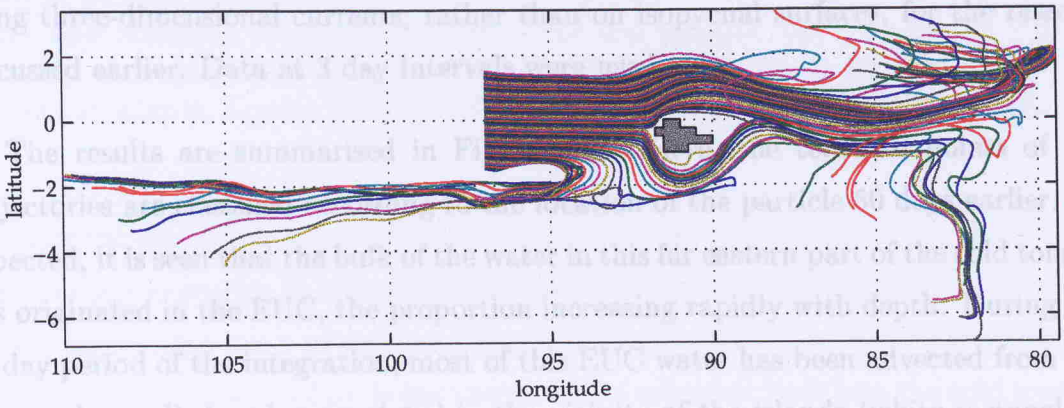

Figure 3.13: Isopycnal trajectories originating at 60m depth, for the strong EUC case.

3.3.3 Results 2: Origin of Cold Tongue waters

A set of 50-day back trajectories terminating on day 3865 (1st August, year 10) was calculated. Figure 3.14 shows the horizontal mesh of terminal positions (92°W to 96°W at 0.5° resolution, by 2°S to 1°N at 0.2° resolution). OCCAM SSTs for the end day are also shown; the cold tongue is at its coolest at this time of year in the model. In the vertical the mesh was 0 m to 30 m at 5 m spacing, giving a total of 1008 trajectories. Since these are all quite shallow, the trajectories were calculated

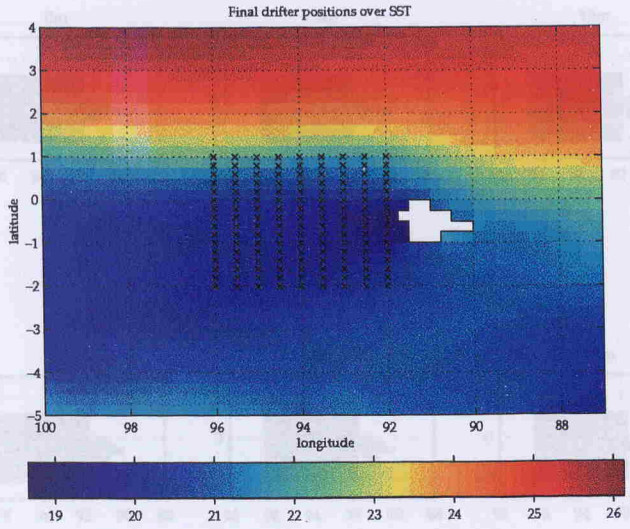

Figure 3.14: End positions for drifter back-trajectory calculations ending in the cold tongue, superimposed on model SST (in degrees Celsius) for end time.

using three-dimensional currents, rather than on isopycnal surfaces, for the reasons discussed earlier. Data at 3 day intervals were used.

The results are summarised in Figure 3.15. Here, the terminal points of the trajectories are classified according to the location of the particle 50 days earlier. As expected, it is seen that the bulk of the water in this far eastern part of the cold tongue has originated in the EUC, the proportion increasing rapidly with depth. During the 50 day period of the integration, most of this EUC water has been advected from the west and upwelled and recirculated in the vicinity of the islands (white rectangles). Another portion (blue rectangles) has only undergone the final part of this journey during this time, this being particularly true in the "plume" region immediately to the west of the islands. In the top few metres, on the other hand, most of the water has come from the east of the islands. Since the surface waters to the west of the Galápagos are generally cooler than those to the east, it is not surprising that the majority of these trajectories originate at depth (red rectangles), as opposed to the topmost model level (green rectangles). Interestingly, this also applies to the trajectories terminating in the relatively warm waters (SST greater than 21°C) in the northern branch of the SEC, on the northern side of the front.

A typical set of trajectories is depicted in Figure 3.16, which shows the paths of

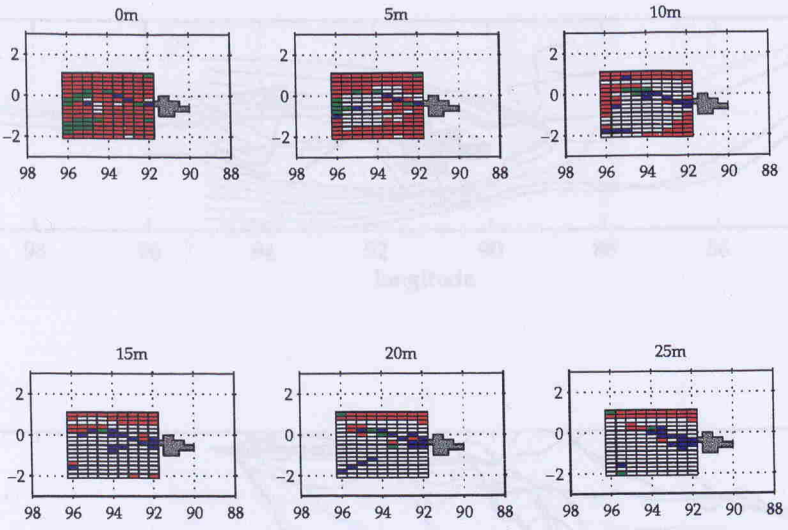

Figure 3.15: Origin of cold tongue waters in OCCAM as determined from back-trajectory calculations. Each frame indicates the source region for trajectories terminating at the depth shown in the title. There is one rectangle centred on the end position for each trajectory, colour coded as follows. White: Origin in the EUC west of the end position. Blue: Origin east of the end position but west of the islands, probably also ultimately from the EUC. Red: Origin at depth (greater than 10m) east of the islands. Green: Origin at the surface (above 10m) east of the islands.

the particles which finished at 5 m depth and 95°W. As will be seen from Figure 3.15, this contains examples of each type of trajectory. One unusual feature of this set of trajectories is that some of the water particles originating in the EUC have travelled right round the islands before being upwelled and advected back into the cold tongue. This is true of only 70 (13%) of the 548 trajectories originating in the EUC west of the Galápagos. The majority (399 or 72%) are turned back before reaching the longitude of the islands, the remaining 79 (14%) being retroflected at some point to the north or south of the islands, like the black trajectory terminating at 0.8°S in Figure 3.16. Of the particles originating to the east of the islands, the majority have come from the north-east, again as suggested by this Figure. Snapshots of the near-surface currents indicate that these are ultimately derived from recirculated NECC water. A set of trajectories was taken back 150 days in order to test this. The particles which passed north of the islands en route to the cold tongue or SEC did indeed originate in the NECC. The other back trajectories became becalmed near the South American coast, so that it was impossible to determine their ultimate origin.

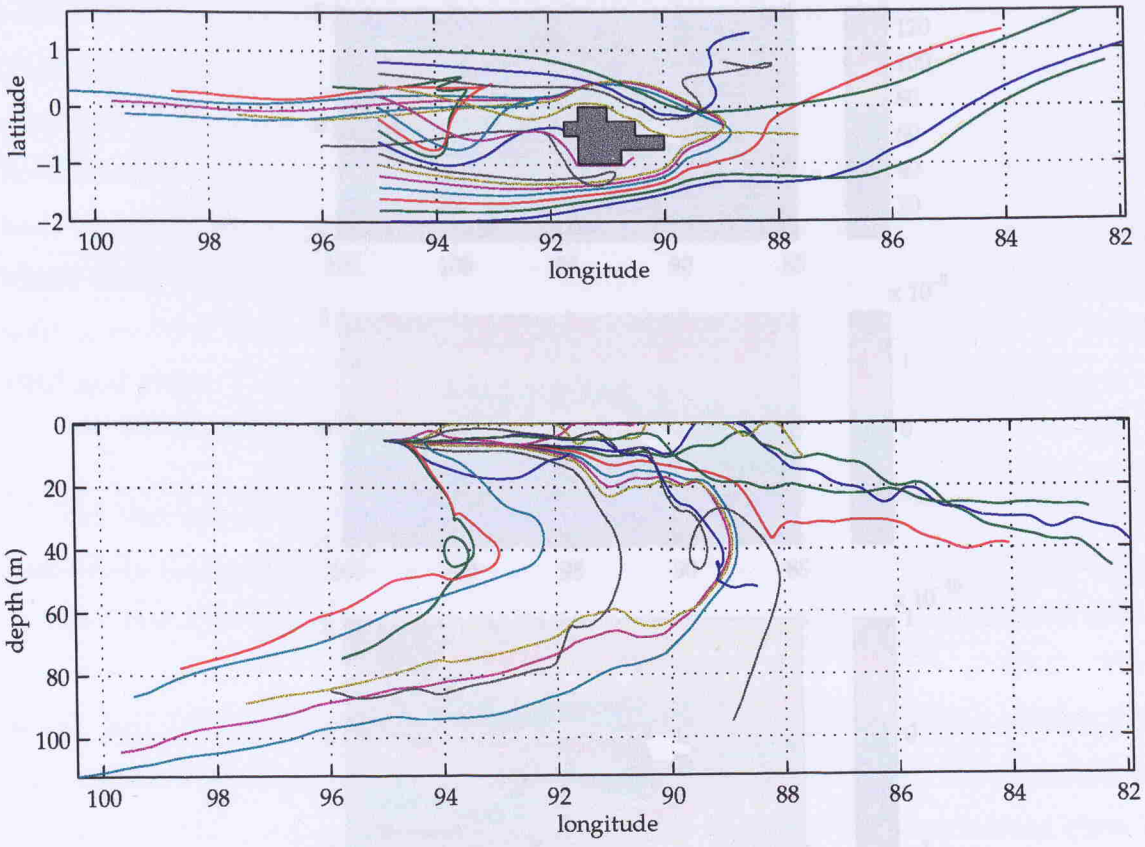

Figure 3.16: 50-day back-trajectories ending at 5 m depth and 95°W on day 3865 (1st August year 10) of OCCAM.

3.4 Island Jets and Tropical Instability Waves

An examination of a sequence of charts of surface velocity spanning an annual cycle of the model reveals that two westward jets can usually be found beginning at the northern and southern tips of the islands. At no time are they observed to the east of the Galápagos. The jets are at their strongest from early June till early November, but are clearly identifiable at almost all other times.

The possibility that these jets are generated by the interaction of the SEC with the Galápagos topography has already been noted, particularly in section 2.2.2, where evidence for such jets was found in an ocean colour scene. In this section we show that the jets found in OCCAM are broadly consistent with the theory of low-frequency flow past an equatorial island due to Cane and du Penhoat (1982) (henceforth referred

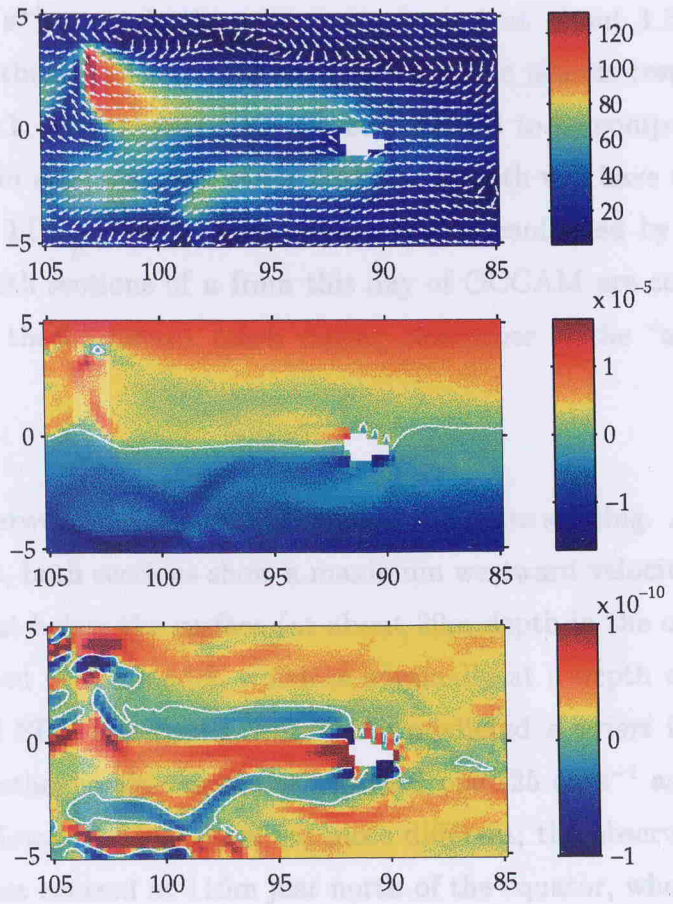

Figure 3.17: Top panel: Currents at 10m depth from day 3510 of OCCAM (11th August, year 9). Colour scale is speed in cm s^{-1}. The arrows, all of the same length, indicate the direction of the flow. Middle panel: Absolute vorticity associated with zonal component of flow (*i.e.* $f - \partial u/\partial y$), in s^{-1}. Bottom panel: Meridional derivative $\beta - \partial^2 u/\partial y^2$ of quantity plotted in middle panel. See text for significance of last two plots.

to as "CdP") and presented in Appendix A. Velocity sections from the historical record are adduced in further support of the verisimilitude of the model's flow field. Finally, evidence for a connection between these jets and the production of TIWs in the model is presented.

3.4.1 Island Jets

The top panel of Figure 3.17 shows near-surface velocities in the vicinity of the Galápagos on day 3510 of OCCAM, *i.e.* 11th August of year 9. Zonal jets of be-

tween 40 and 60 cm s^{-1} towards the west are apparent at about 1.5°N and 2°S, originating at the northern and southern boundaries of the islands respectively. As explained in section 3.1, flows at this time can be expected to be comparable to real flows somewhat later in a typical year of the real ocean; both will have a strong SEC and, usually, intense TIW activity. This expectation is confirmed by Figure 3.18, where three north-south sections of u from this day of OCCAM are compared with similar sections from the literature, taken during November of the "normal" years 1983 and 1984.

The similarities between the two sets of sections are quite striking. At 85°W, just east of the Galápagos, both sections show a maximum westward velocity close to the equator and somewhat below the surface (at about 20m depth in the observed data, and in the second level of the model, which is nominally at a depth of 30m). This is the well developed SEC mentioned earlier. As predicted *a priori* in section 3.1, the modelled jet is rather weaker than the observed one (25 $\mathrm{cm\,s^{-1}}$ as compared to 40 $\mathrm{cm\,s^{-1}}$). Deeper down, the two flows are more different; the observations show a weak westward current centred at 110m just north of the equator, whereas OCCAM has a weak eastward flow (of 15 $\mathrm{cm\,s^{-1}}$) at this location. This discrepancy may be due to the unsteadiness of the flow in this region; for instance, OCCAM has a small area of westward current nearby (at 87.75°W and 0.5°N) just 15 days later. Note that in neither section is there any evidence of surface jets or a divided SEC at this longitude. Although the observed section only extends to 1°N and S, the similarity with the model section and the absence of jets in the top panel of Figure 3.17 strongly suggest that they were absent from the ocean in November 1984.

At 92°W, immediately west of the islands, the near-surface flows are even more alike. In both cases there are westward jets north and south of the latitudes of the islands, with maximum velocities at the surface, separated by a region of weaker (possibly eastward) flow which is an upward extension or surface manifestation of the EUC. Both of the northern jets are centred at around 1.5°N, and both of the southern jets seem to be centred at or slightly south of the southern edge of the section. In each case the northern jet is the stronger of the two, at least in the sense that it penetrates to a greater depth than the southern one. Deeper down, both sections

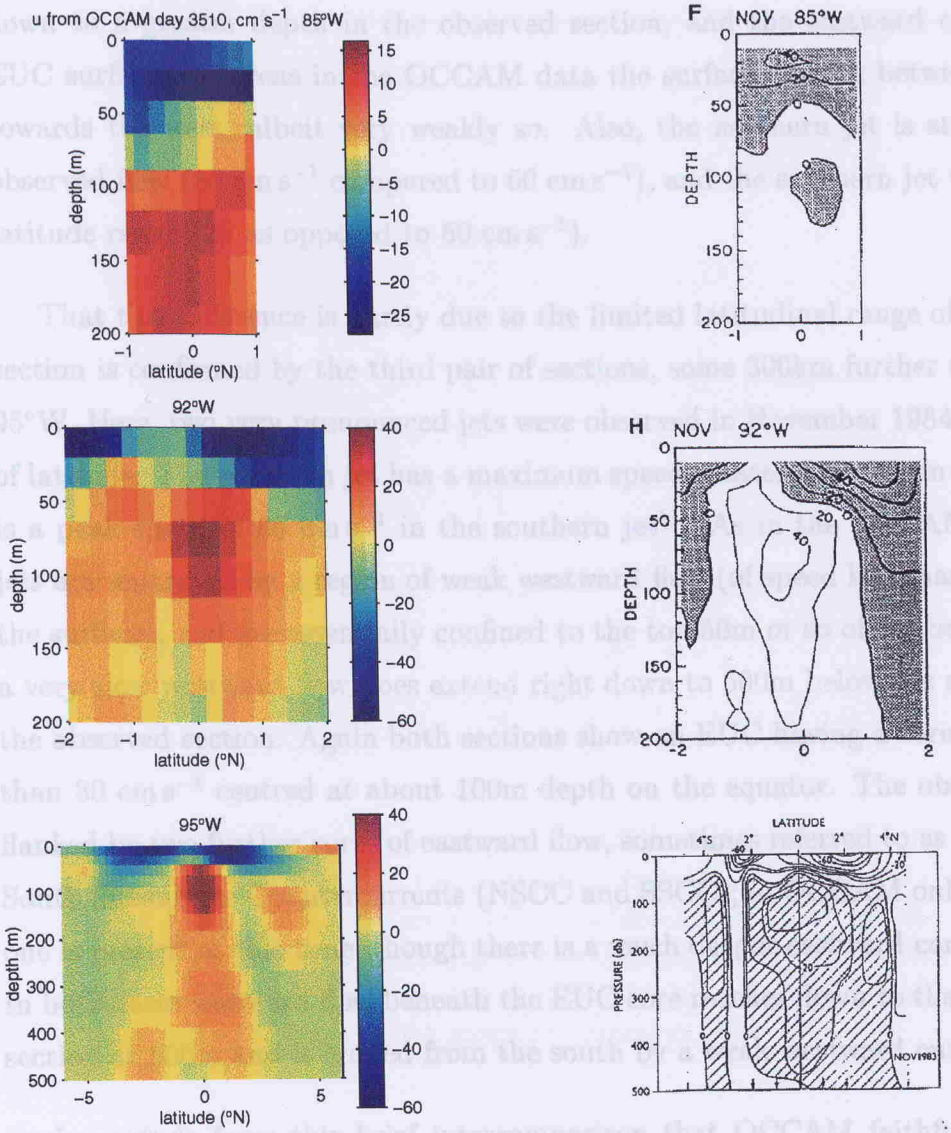

Figure 3.18: Left: North-South sections of zonal velocity u (cm s^{-1}) from day 3510 of OCCAM, for comparison with the observed sections in the right-hand column. Right: Sections from Wilson and Leetmaa (1988) (top two) and Hayes *et al.* (1986) (bottom). Top: At 85°W in November 1984. Middle: At 92°W in November 1983. Bottom: At 95°W in November 1983. In the top two, which are based on direct current measurements made using an ADCP, the contour interval is 20 cm s^{-1} and negative (westward) currents are shaded; in the bottom diagram the interval is 10 cm s^{-1} and positive (eastward) currents are hatched. An amalgam of direct and indirect (geostrophic) current estimates were used for this diagram, currents polewards of ±2° being geostrophic.

display a clearly defined EUC having a core velocity of about 40 cm s^{-1}. Detailed differences between the sections do exist. The westward currents in the jets reach

down to a greater depth in the observed section, and the eastward current of the EUC surfaces, whereas in the OCCAM data the surface current between the jets is towards the west, albeit very weakly so. Also, the northern jet is stronger in the observed flow (80 $\mathrm{cm\,s^{-1}}$ compared to 60 $\mathrm{cm\,s^{-1}}$), and the southern jet weaker in this latitude range (20 as opposed to 50 $\mathrm{cm\,s^{-1}}$).

That this difference is partly due to the limited latitudinal range of the observed section is confirmed by the third pair of sections, some 300km further to the west at 95°W. Here, two very pronounced jets were observed in November 1984 at about ±2° of latitude. The northern jet has a maximum speed greater than 90 $\mathrm{cm\,s^{-1}}$, and there is a peak speed of 60 $\mathrm{cm\,s^{-1}}$ in the southern jet[14]. As in the OCCAM section, the jets are separated by a region of weak westward flow (of speed less than 30 $\mathrm{cm\,s^{-1}}$ at the surface), and are essentially confined to the top 50m or so of the ocean, although a very slow westward flow does extend right down to 500m below the southern jet in the observed section. Again both sections show an EUC having a core speed greater than 30 $\mathrm{cm\,s^{-1}}$ centred at about 100m depth on the equator. The observed EUC is flanked by two further cores of eastward flow, sometimes referred to as the North and South Subsurface Countercurrents (NSCC and SSCC); in OCCAM only the northern one is present at this time, though there is a much deeper eastward core in the south. In both cases eastward flow beneath the EUC core reaches down to the bottom of the section at 500m and is eroded from the south by a weak westward current.

I conclude from this brief intercomparison that OCCAM faithfully reproduces oceanic flow patterns that exist at times in the real ocean in the neighbourhood of the Galápagos. Since Figure 3.17 strongly suggests that the presence of the islands is responsible for the two surface jets in OCCAM, and since the jets are observed to the west but not the east of the islands in the real ocean, this intercomparison provides circumstantial evidence that the observed jets are also due to the islands. This connection has not been made by previous authors.

Further confirmation is provided by the consistency of these jets with the CdP

[14]Note, however, that it is possible that these speeds may be slightly exaggerated. Currents poleward of ± 2° of latitude in this section were calculated from the geostrophic relation, which is very sensitive to small errors in dynamic height at such low latitudes, because of the smallness of the Coriolis parameter here.

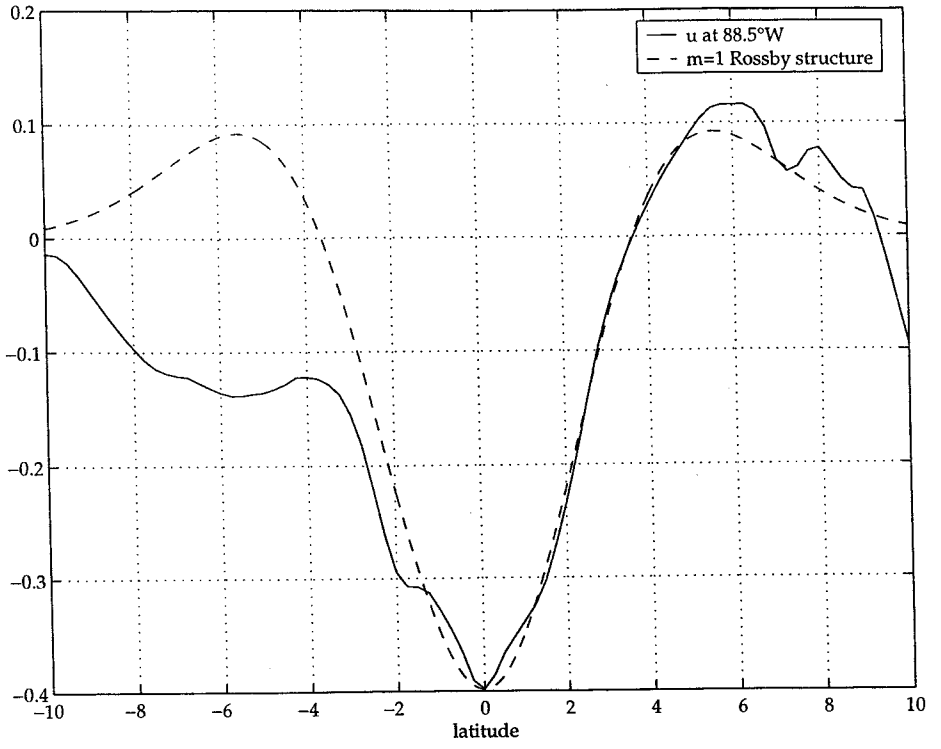

Figure 3.19: Zonal velocity u along the 88.5°W meridian on day 3510 of the main run of OCCAM, compared to the meridional structure function for the m=1 Rossby wave based on a Rossby radius of 329km, which is the value for the first baroclinic mode of a typical model profile east of the Galápagos. u here is the depth-weighted average of the values in the top two model layers. It has been scaled so as to have the same minimum value as the structure function.

theory referred to above. As explained in Appendix A, this theory predicts that the existence of such jets should be a characteristic feature of flows past equatorial islands, at least when the flow has been reasonably steady for a period of several days. CdP furthermore give expressions for the transport of the jets in terms of the ambient flow conditions. In general, in order to calculate these transports one needs to express the ambient flow near the islands as a superposition of "long" equatorial Kelvin, Rossby and Rossby-gravity waves (a procedure which is always possible given the completeness of the set of structure functions for these waves). However, the upstream zonal velocity in Figure 3.17 has a meridional structure sufficiently close to that of a first meridional mode Rossby wave, at least from 3°S to 7°N (see Figure 3.19) to justify considering only this mode for the order-of-magnitude calculations being attemped here.

Details of the calculation are given in Appendix B. Because the SEC and jets are confined to the top two model levels (see Figure 3.18), we consider the depth-weighted average of u from these two levels, as in Figure 3.19. Using the peak westward velocity (on the equator) to determine the amplitude of the Rossby wave in the model leads to predicted transports of 0.85 and 0.79 Sv to the west in the northern and southern jet respectively. Taking the jets to extend from the latitudes of the north and south coasts of the model Galápagos to 1.25°N and 2.25°S (as suggested by inspection of the top panel of Figure 3.17), their transports (after subtracting the transports east of the islands at the same latitudes) are respectively 0.84 and 0.63 Sv at 92°W.

On the one hand, the close agreement may be considered slightly fortuitous given all the simplifications and approximations involved, such as the steady state assumption, the neglect of other modes, and the lack of consideration given to the vertical structure or to other processes such as recirculation of water from the EUC and NECC. It is true that the values obtained are fairly sensitive to the choice of latitude range over which the jets are considered to exist, for instance. On the other hand, the agreement may not appear very surprising given that the basic physical process involved is a deflection of the SEC around the northern and southern tips of the island; if the upstream flows are similar in the two cases, the total transports downstream are likely to be similar too. However, the theory does make some predictions which are not obvious *a priori*, namely the fact that the flow *is* almost entirely diverted around the islands, rather than being reflected or deflected vertically[15]; the zonal character and narrow latitudinal confinement of the modified downstream flow, which is unlike even laminar wakes in non-rotating flow (see Tritton (1988, pages 21–34)); and the partition of the transport between the two jets, with the northern jet being only slightly stronger than the southern one in this case (we might expect the northern jet to be considerably stronger, as with the flow of the EUC around the islands discussed elsewhere, given the asymmetry of the islands about the equator). Since these properties are all possessed by the OCCAM flow, we can say that the plausibility of this flow, and the hypothesis that the jets are caused by the islands, are supported by this theory. Alternatively, we could argue that the theory is borne

[15]See Appendix B; there is a reflected Kelvin wave, but the currents involved are very feeble for the case of the Galápagos.

out by the observations presented in the right-hand column of Figure 3.18.

3.4.2 Tropical Instability Waves

We now turn to evidence for a connection between the jets and the Tropical Instability Waves (TIWs) first mentioned on page 2. We begin by showing that TIWs do exist in OCCAM, and that they do seem to arise or be amplified a short distance to the west of the Galápagos.

TIWs are essentially large eddies, of diameter about 1000km, on the Galápagos Front (although they also occur and are reasonably energetic south of the equator), and so they can be expected to give large signals in the fields of meridional velocity component v and sea surface temperature (SST). Figure 3.20 displays time-longitude diagrams of SST and v at the equator and at 4°N from one year of the main run of OCCAM, with annual and semi-annual harmonics removed. The most noticeable features on these diagrams are the stripes running from the bottom right to the top left of each frame. 2D Fourier analysis of the time-longitude data shows these westward propagating signals to have periods of about 30 days and wavelengths of about 1000km, so they are TIWs. This is confirmed by snapshots of SST, such as Figure 1.2, which closely resemble plots of satellite SST in which TIWs have been identified (see *e.g.* Philander *et al.* (1985)). Further confirmation is provided by animations of various dynamical and other fields. Animations of v in particular show very directly the nature of the waves as a mixture of Rossby-gravity waves and first meridional mode Rossby waves. In the eastern part of the TIW region they tend to have a Rossby-gravity character, the meridional profile of v taking a maximum at the equator and decreasing as a Gaussian either side thereof. A least squares fit to a typical meridional profile of v in this region gave a Rossby radius of 106 km, which corresponds to a high (10th) baroclinic mode—the waves will be essentially surface-trapped in this zone. Further west the waves more often assume the asymmetry about the equator characteristic of first meridional mode Rossby waves (though the Rossby-gravity waves still persist and indeed amplify in this region, as evinced by, for instance, charts of the mean variance of v; *cf.* Figure 3.24(a)). This time the meridional scale is closer to that of the first baroclinic mode; direct evidence for the

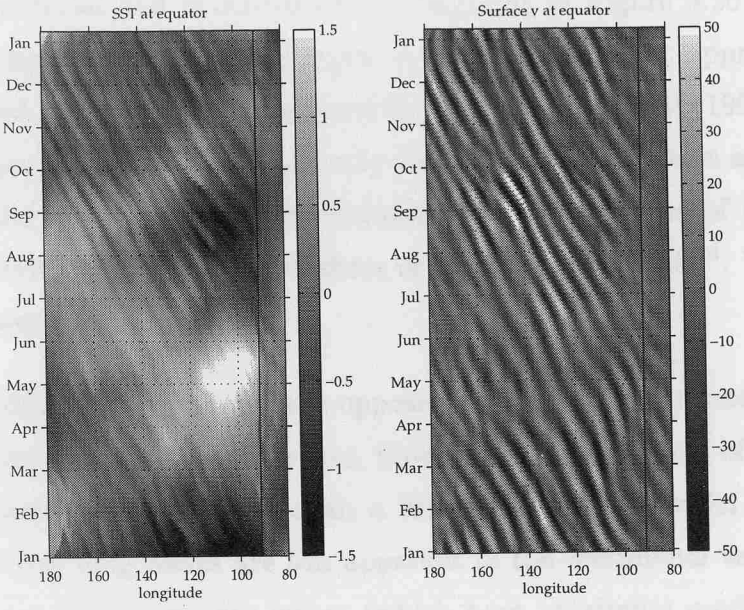

(a)

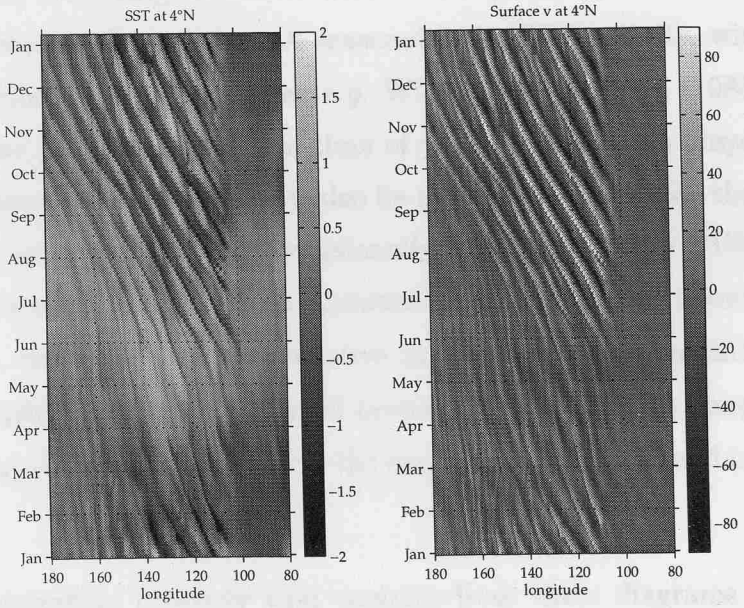

(b)

Figure 3.20: Time-longitude diagrams of SST and surface v from year 10 of the main run of OCCAM (3-daily data). (a) At the equator. (b) At 4°N. At each longitude the timeseries has been detrended and a best fit annual-plus-semiannual harmonic has been removed.

first baroclinic mode nature of these waves appears in section 3.5. The similarity between the equatorial and extra-equatorial diagrams in Figure 3.20 points to the perhaps surprising fact that the two types of wave propagate at approximately the same phase speed. This has been explained by Munnich and Latif (1998), who argue that these two particular waves are the only free modes of oscillation available to the equatorial Pacific whose propagation characteristics match those of the barotropic instability induced by the background shear of the surface currents[16]. TIWs are thus a kind of resonance.

The more diffuse bands going in the opposite direction in the equatorial diagrams of Figure 3.20 are probably Kelvin waves, though their zonal speed of about 1 $\mathrm{m\,s^{-1}}$ indicates a second or third rather than a first baroclinic mode (cf. section 3.5). The fact that these long waves are less apparent in the meridional velocity suggests that they are not Rossby-gravity waves (which have maximum meridional velocity amplitude at the equator). It is interesting to note the retardation and apparent weakening during the spring of the TIWs in the 4°N pictures, when these longer waves are most apparent at the equator. A seasonality in TIW activity, with a minimum in the spring, has been observed, see *e.g.* Wilson and Leetmaa (1988), though the weakening of the trade winds at this time of year certainly also plays a role in this cycle. Modulation by long waves may also be partly responsible for the impression of eastward group velocity which has occasionally been reported for TIWs; for instance Steger and Carton (1991) report an eastward group velocity of about 30 $\mathrm{cm\,s^{-1}}$ for Atlantic TIWs, based on a semi-subjective analysis of weekly satellite SST images. A similar, though more rapid, eastward propagation in the TIW amplitudes can be made out in Figure 3.20, particularly in the early part of the year and in the equatorial v diagram.

Another interesting property that emerges from these diagrams is an apparent merging of TIW eddies. In the 4°N SST picture this can be seen to happen at about 110°W in August/September, and there are a few other less clear examples. Merging events also show up clearly in animations of the SST field; the further east of a pair of eddies catches up and combines with its predecessor. This behaviour has not

[16]Note that these authors do not discuss the vertical modes required to satisfy the wavelength/frequency requirements.

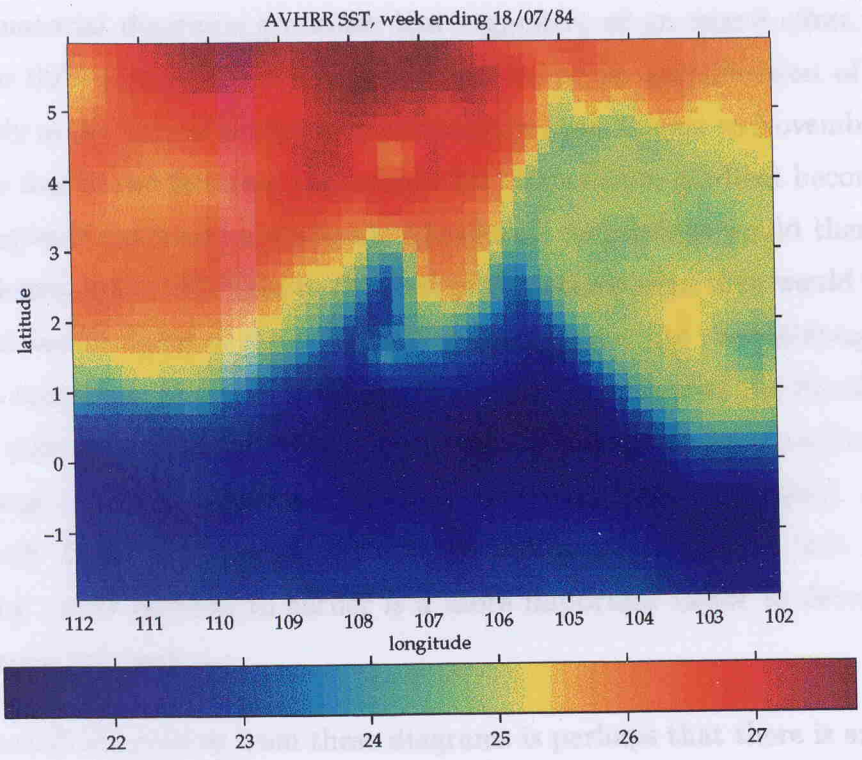

Figure 3.21: AVHRR interpolated SST image for week ending 18th July 1984. Colour axis is SST in degrees Celsius.

been reported in the literature, perhaps because the spatial and temporal coverage of observations is insufficient to detect these relatively infrequent events. That said, images can be found in the AVHRR record (*Kidwell*, 1995) which suggest that such events do take place in the real ocean, for example Figure 3.21.

However, of greater significance to the present study is the information these diagrams contain concerning the regions in which the TIWs are generated or amplified. It is very striking that at 4°N the TIWs suddenly attain their maximum amplitude when they pass through 102°W or thereabouts, and can scarcely be made out at all further east. Animations of SST also suggest that the northern TIW eddies grow out of undulations in the Galápagos front at about this longitude. As this occurs at the same longitude throughout the year, it is unlikely to be an effect of the wind and more likely to be due to a topographic effect, presumably of the Galápagos since this is the only significant topographic feature in the area.

The equatorial diagrams are much less suggestive of an island effect. It is true that in the SST picture there is some suggestion of an amplification of the waves immediately to the west of the islands, particularly from August to November, but this is probably due to the fact that the meridional temperature gradient becomes greater at this longitude (as noted elsewhere). Meridional oscillations would therefore show up more clearly in the SST field to the west of the islands than they would to the east. No obvious modification of the v field takes place on passing the Galápagos. For the first seven months of the year TIW-like oscillations originate at the South American coast and pass the islands pretty much unaffected (though there is maybe a hint of a phase change *e.g.* in the wave which reaches the islands in early April). Amplitudes are generally larger west of the Galápagos, but it would appear that modulation by the long waves referred to earlier is a more important factor in determining the amplitudes in this region.

The overall impression from these diagrams is perhaps that there is an equatorial mode of oscillation, at the frequency and wavelength of TIWs, which exists at small amplitudes east of the islands[17] but which is much amplified and spreads away from the equator after it has passed the islands. We now present evidence for a possible mechanism for this amplification.

The middle panel of Figure 3.17 shows the absolute vorticity $f - u_y$ associated with the zonal component of the flow. This quantity is of the opposite sign to the Coriolis parameter f if the flow state is inertially unstable, assuming the flow to be zonal and geostrophically balanced (*Holton*, 1979, pages 214–216). From the top panel of the figure, the first assumption is clearly good in the vicinity of the Galápagos. The second assumption is also good provided that the flow is not rapidly changing, both in general (*Brentnall*, 1995) and in particular when the flow is describable in terms of linear equatorial wave dynamics under the long wave approximation (*Cane and du Penhoat*, 1982). The zero contour that is plotted on the vorticity diagram does not wander more than a few tenths of a degree from the equator, where it must be if the flow *is* geostrophic, except for a small closed contour at about 103°W, 3.7°N, in the highly sheared leading edge of the TIW eddy. We might expect lateral mixing

[17] It would be interesting to install a mooring on the equator between the Galápagos and the South American mainland, to see if these oscillations exist in the real ocean.

to be taking place in this region, inertial instability being one possible mechanism. Alternatively, it might simply not be appropriate to talk of a geostrophic basic state in this part of the eddy. Anyway, this diagram shows this particular flow *not* to be inertially unstable, although we may note that the field comes close to zero in the region of strong anticyclonic shear at about 1.5°N in the northern jet.

The bottom panel of Figure 3.17 shows $\beta - u_{yy}$, *i.e.* the meridional derivative of the absolute vorticity plotted in the middle panel. Kuo's criterion (*Kuo*, 1949) states that this quantity passes through zero somewhere if the flow is barotropically unstable, and again the zero contour has been plotted here. We see at once that the criterion is satisfied comfortably in the jet regions to the west of the Galápagos, but only marginally to the east of the islands. It is interesting to note that Wilson and Leetmaa (1988) found the Kuo criterion to be satisfied near the surface at 1° or 2°N in ADCP sections along 108°W and 110°W at different times during 1984, whereas at 150°W it was satisfied only in November, at the height of the TIW season. As we have already noted, their November section at 92°W (the middle right panel of Figure 3.18) exhibits jets that are very similar to those in OCCAM, in both strength and location. Unfortunately they did not calculate the vorticity gradient for this section, but it is reasonable to suppose that this too would have satisfied the criterion.

As discussed in section 2.1.2, some relevant transects from the IRONEX2 cruise of November 1993 are available, and these have been subjected to such an analysis. The results are presented in Figure 3.22, where features on a smaller scale than would be resolved by OCCAM have been filtered out (see the caption). Similar sections from our case study day of OCCAM are presented for comparison in Figure 3.23. A wider latitude range has been used in the OCCAM sections. Furthermore the section at 89.75°W rather than 89°W has been used for the model section east of the Galápagos, because that is the longitude where the model bathymetry reaches 250m at 1°S. In section 2.1.2 we noted that this occurs at 89°W for the real topography, and proposed that this was dynamically significant in causing the SEC to divide. Sure enough, the model transect also shows an SEC which is divided at this longitude (unlike the SEC at 89°W, see Figure 3.18), the two branches both being weaker than they are west of the islands (which is also true of the observed flow). The model also agrees with

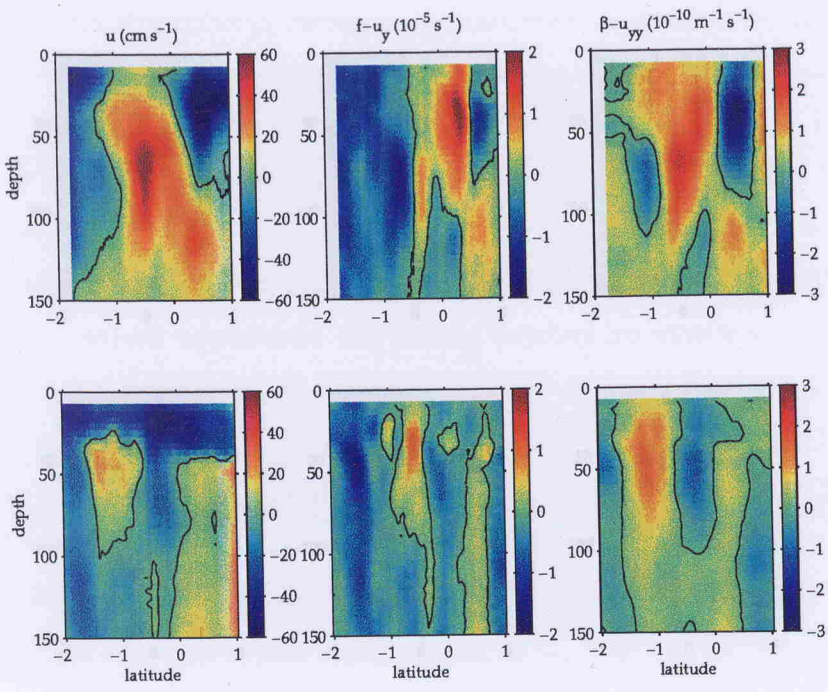

Figure 3.22: Stability analyses on IRONEX ADCP sections of u at 92°W (top) and 89°W (bottom). From left to right are shown u, $f-u_y$ and $\beta-u_{yy}$. The section at 92°W was composited into 0.01°bins and smoothed with a 25-point rectangular filter before plotting and before calculating u_y. A 51-point filter was used prior to performing each differentiation in the calculation of $\beta-u_{yy}$. For the 89°W section the figures are 0.05°, 5 points and 11 points. The black lines are zero contours.

the observations in having an EUC that is at about 70m west of the Galápagos, and which is divided into two branches to the east of the islands. Further diagnostics confirm that the two branches are in the process of re-merging, in the model as in the IRONEX data.

Of great significance to the present study is the fact that the zero contours of the curvature $\beta-u_{yy}$ assume similar shapes in the two sets of data. In both cases barotropic instability is indicated in each of the surface jets at 92°W, and again in the shear zones on the northern and southern flanks of the EUC. A similar pattern exists east of the islands, except that there are separate unstable regions associated with each branch of the divided EUC (though this is not very clear in the observations since these do not extend far enough to the north to cover the whole of the northern branch).

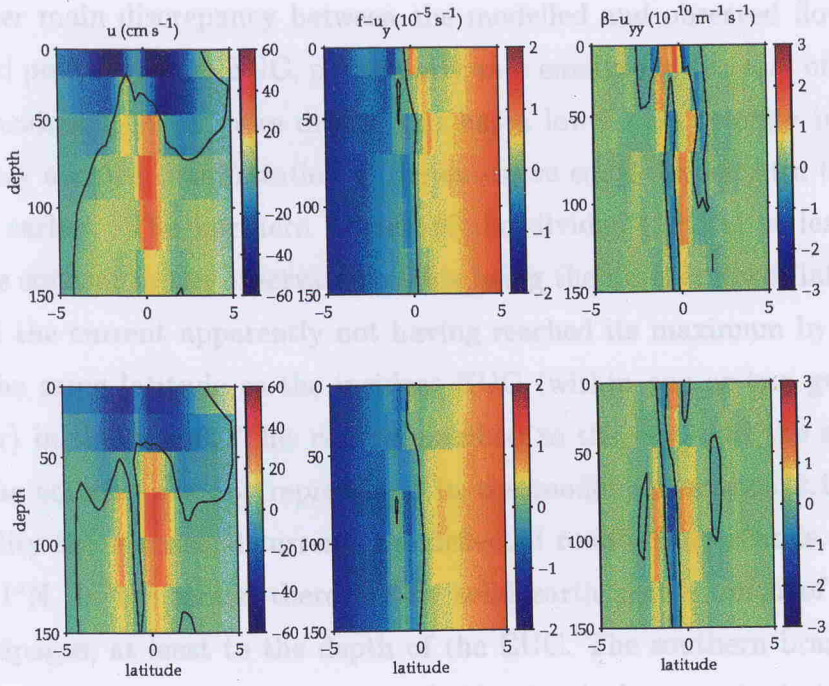

Figure 3.23: As Figure 3.22 but for model sections at 92°W and 89.75°W. No filters have been applied.

Despite these qualitative similarities, there are some quantitative differences between the model and observed transects. Firstly, the SEC jets or branches are more diffuse in the model. They extend to at least 2°N and S, whereas the northern branch in the IRONEX data has a well defined core at about 0.7°N west of the islands and would appear not to extend much further north than 1°N. Since the model's horizontal resolution is sufficient to represent a more confined jet, it is likely that the eddy viscosity is inappropriately large as regards this phenomenon. As a consequence the shears are considerably smaller in the model; for instance, there is no region of eastward surface flow between the two jets in OCCAM. As a consequence of *this*, whereas the observed flow is sufficiently sheared to produce negative absolute vorticity, making the flow susceptible to inertial instability, on the northern flank of the northern branch west of the Galápagos[18], there are no significant such regions in the model transect. Likewise, the curvatures involved in the Kuo criterion calculations are smaller in the model than in the observed data.

[18]The patch of positive vorticity (south of the equator) between the northern SEC and southern EUC in the 89°W section is arguably another case in point.

The other main discrepancy between the modelled and observed flows is in the strength and position of the EUC, particularly as it emerges to the east of the islands. That the incident EUC is more diffuse and has a lower core velocity in the model is presumably another manifestation of the excessive eddy viscosity (in this context) referred to earlier. The northern branch of the divided EUC is at least 1 degree north of the equator in the observations (this being the northernmost latitude of the section and the current apparently not having reached its maximum by this point), but is at the same latitude as the incident EUC (within one or two grid points of the equator) in the model. This can be ascribed to the fact that the small islands north of the equator are not represented in the model—in section 2.1.2 we noted that in reality the equatorial currents are deflected round these islands, which reach almost to 1°N. In the model there are no solid earth points north of the equator in the Galápagos, at least to the depth of the EUC. The southern branch is rather shallower in the observations; this is probably simply because it derives from the southward-extending lobe of the incident current at about the same depth (40 or 50 metres).

Nevertheless, the observations provide important confirmation that the equatorial currents are divided into two branches as they pass round the islands; that the SEC continues as two branches further west, whereas the EUC recombines into a single current to the east; and that the SEC jets are barotropically unstable according to the Kuo criterion.

Although there are a few dissenting voices[19], theory and numerical experiments have produced a consensus that TIWs are principally due to barotropic instability. This result dates back to the pioneering work of Philander (1976; 1978) and has been confirmed by calculation of energy transfer terms from observations (*Hansen and Paul*, 1984; *Wilson and Leetmaa*, 1988; *Brady*, 1990, etc.), which indicate that the background potential energy provides only about a tenth of the energy of the waves.

In OCCAM too the principal energy source seems to be barotropic instability. Figure 3.24 presents two terms in the equation for the conversion of mean to eddy

[19]Notably McCreary and co-workers (*McCreary and Yu*, 1992; *Yu et al.*, 1995), who have suggested that the main energy source is a "frontal instability" associated with meridional temperature gradients.

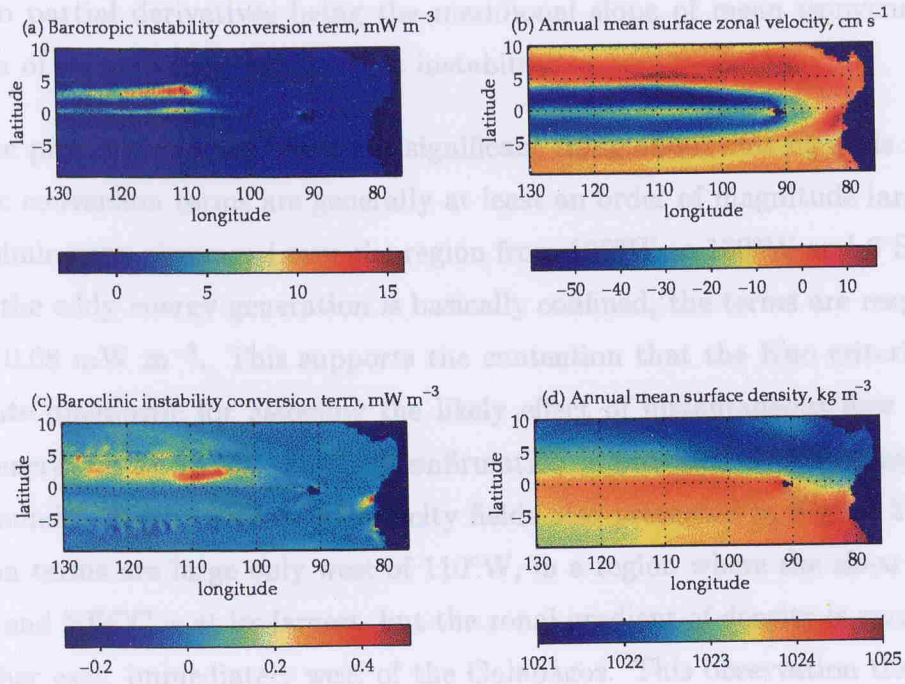

Figure 3.24: (a) Barotropic and (c) baroclinic mean-eddy energy conversion terms for the surface layer of OCCAM, in mW m^{-3}, averaged over one model year (8th January year 10 to 3rd January year 11). (b) and (d) present the surface u and ρ fields averaged over the same period.

energy in the surface layer, averaged over 1 year of OCCAM data. The first,

$$-\overline{\rho}\,\overline{u'v'}\,\frac{\partial \overline{u}}{\partial y}, \tag{3.3}$$

represents the interaction between the northward eddy transport of eastward momentum and the shear of the background zonal velocity field, *i.e.* the production of eddy energy by barotropic instability. Here the overbar stands for averaging over the one year's worth of data. These were only available at 3-daily intervals; the apparent patchiness in the zonal direction is due to aliassing with the approximately 30-day oscillations of the TIWs. Primed quantities are instantaneous deviations from the mean values.

The second term plotted is

$$-g\overline{v'\rho'}\,\frac{\partial \overline{\rho}/\partial y}{|\partial \overline{\rho}/\partial z|}, \tag{3.4}$$

which represents the conversion of mean potential energy to eddy energy (the ratio

of the two partial derivatives being the meridional slope of mean isopycnals), *i.e.* generation of eddy energy by baroclinic instability.

For the present purposes, the most significant thing about this figure is that the barotropic conversion terms are generally at least an order of magnitude larger than the baroclinic ones. Averaged over the region from 100°W to 130°W and 6°S to 6°N, in which the eddy energy generation is basically confined, the terms are respectively 1.16 and 0.08 mW m^{-3}. This supports the contention that the Kuo criterion is an appropriate diagnostic for assessing the likely effect of instantaneous flow patterns on the generation of TIWs. Further confirmation is provided by the annual mean ("background") density and zonal velocity fields also presented in Figure 3.24. The conversion terms are large only west of 110°W, in a region where the shear between the SEC and NECC is at its largest, but the zonal gradient of density is smaller than it is further east, immediately west of the Galápagos. This observation ties in with Figure 3.20, where we saw that the TIW signal at 4°N amplifies suddenly at about this longitude. None of the terms is large on the equator east of this region, which suggests that the equatorial oscillations observed close to the South American coast in Figure 3.20 may be a free mode. Various other terms have been calculated at various depths to confirm this.

As an aside, we note that calculations based on Lagrangian drifter data from the equatorial Pacific (*Baturin and Niiler*, 1997) show that the term

$$-\overline{\rho}\,\overline{v'v'}\,\frac{\partial \overline{v}}{\partial y},$$

representing the interaction between the background (Ekman) divergence and the meridional Reynolds flux of meridional momentum, is also significant. In the surface layer of OCCAM this term has a magnitude intermediate between that of the baroclinic and barotropic terms; averaged over the same region, this term is -0.14 mW m^{-3}. The minus sign indicates that the net effect of this mechanism is to convert eddy to mean energy, but a chart of this quantity reveals that it is positive at about 5°N and negative at about 2°N, so that in these latitudes the mechanism effects a southward transport of mean kinetic energy (decelerating the NECC and accelerating the northern branch of the SEC) using eddy energy as a carrier. The term is negative on the equator (as is the baroclinic term), partially offsetting the generation of Rossby-

gravity wave energy by barotropic instability.

The annual mean data in Figure 3.24 incidentally confirm the year-round influence of the Galápagos on the local conditions in OCCAM. The bifurcated SEC commences at the islands in the annual mean, and the high surface densities associated with the cold tongue terminate abruptly at this longitude. In particular we see again that the cold tongue is clearly separate from any westward extension of the waters of the Peru-Chile upwelling region.

3.5 Seasonal waves

In this section we look at the seasonal waves in OCCAM, to compare them with those noted in the observational data of sections 2.1.1 and 2.1.3, and to examine their behaviour on striking the Galápagos. Figure 3.25 displays the vertical displacement of various isotherms from their annual mean positions at each point, as time-longitude data along the equator. Positive values (red or orange) correspond to downwelling of the isotherms. Depths are calculated by straightforward linear interpolation. This means that the 2.5°C isotherm, for instance, is generally always found in the same vertical grid box (level 21).

One striking feature of this diagram is the set of narrow stripes running from the bottom right to the top left of each frame. These are the signature of TIWs, as discussed in section 3.4; the interesting thing here is that they are discernible even in the data for the 2.5°C isotherm, the average depth of which is about 1750 m. TIWs are generally regarded as a surface-trapped phenomenon; the figure shows that this is not the case in OCCAM. Further confirmation of this observation is provided by Figure 3.26, which is a snapshot of v at 4°N at a time of peak TIW activity. The first baroclinic mode nature of the waves is apparent. For instance, at 130°W the current is southward from the surface to 1400 m, and northward below that, the greatest northward velocities being at the sea bed. Although $|v|$ is much larger in the surface layer, it would be incorrect to characterise the waves as surface-trapped; for instance, the depth-weighted average of v at this time and location is about 1.5 $\mathrm{cm\,s^{-1}}$ to the *north*. Observations sufficiently detailed to test this model prediction directly have

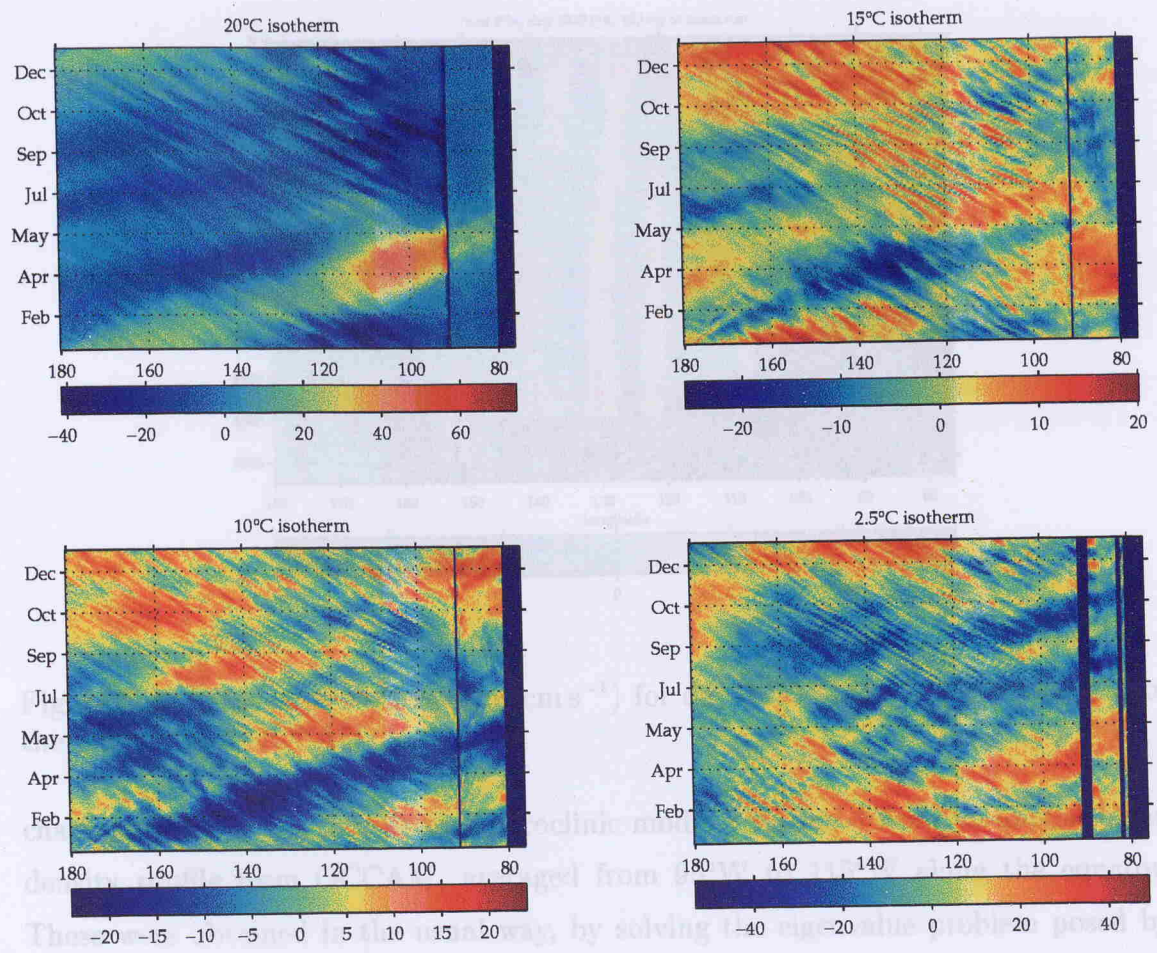

Figure 3.25: Time-longitude diagrams of isotherm depth on the equator from year 10 of OCCAM. Departures from the annual mean at each location are plotted, in metres. Positive values indicate downwelling.

never been made.

Figure 3.25 also reveals several bands of isotherm displacement running in the opposite direction. These are broader in both time and space, and are the seasonal waves in question. The most prominent is the upwelling wave in the 10°C isotherm which arrives at the Galápagos during April–May. Since the 20°C and 2.5°C isotherms both show downwelling at this time, the wave is of at least the third baroclinic mode. As noted in Chapter 2, these seasonal waves have traditionally been identified with Kelvin waves of different vertical modes, and this seems a correct interpretation here too, for the following reasons. Measurements of the slope of the 10°C upwelling band reveal an eastward propagation speed of about 85 cm s^{-1}. Table 3.1 lists the

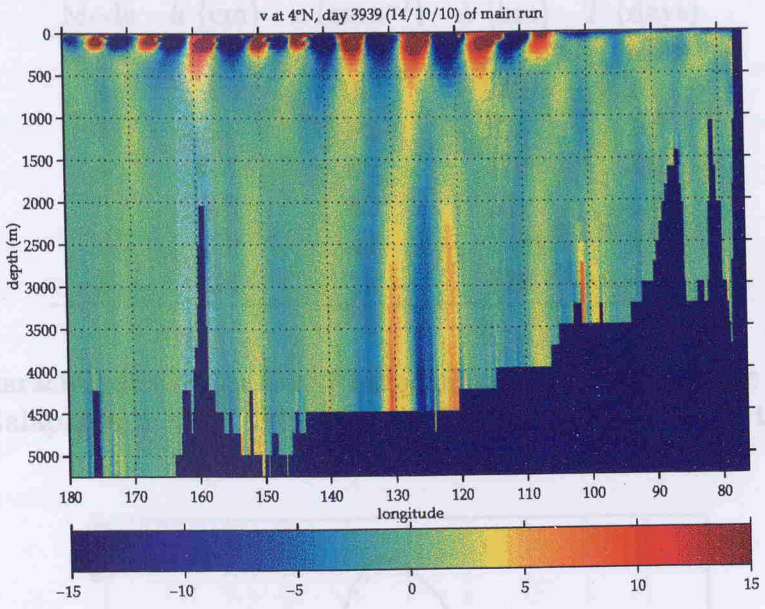

Figure 3.26: East-west section of v ($\mathrm{cm\,s^{-1}}$) for day 3939 (14th October year 10) of the main run of OCCAM, at 4°N.

characteristics of the first several baroclinic modes calculated from an annual mean density profile from OCCAM, averaged from 95°W to 115°W along the equator. These were obtained in the usual way, by solving the eigenvalue problem posed by the vertical structure equation

$$S_{zz} + \frac{N^2}{gh} S = 0 \tag{3.5}$$

for the equivalent depths h.[20] The other parameters are the gravity wave speed $c = (gh)^{1/2}$, Rossby radius $\lambda = (c/\beta)^{1/2}$, and equatorial inertial time $T = (\beta c)^{-1/2}$. Note that c, which is also the speed of equatorial Kelvin waves, takes the value 85 $\mathrm{cm\,s^{-1}}$ for the third baroclinic mode, matching the propagation speed obtained from the time-longitude diagram.

The meridional structure of the isotherm displacement provides another piece of evidence. Figure 3.27 shows the result of fitting the 10°C isotherm displacement at 97°W, at the time when the wave under discussion passes through that meridian, to a function which is essentially the meridional structure function $\exp(-y^2/2\lambda^2)$ of a

[20] See Philander (1990). Here S is the vertical structure function for w (the structure function for the other dynamical fields being $-ghS_z$), so that the boundary conditions for (3.5) are $S = 0$ at the surface and the sea bed. N^2 is the Brunt–Väisälä frequency squared, $-(g/\rho)\partial\rho/\partial z$.

Mode	h (cm)	c (cm s^{-1})	λ (km)	T (days)
1	64.3	251	332	1.5
2	18.1	133	242	2.1
3	7.4	85	193	2.6
4	4.4	66	170	3.0
5	2.8	52	151	3.4
6	1.9	44	138	3.7
7	1.4	38	128	4.0

Table 3.1: Characteristics of the first 7 baroclinic modes of an average density profile west of the Galápagos in OCCAM. See text for further details and the meaning of the symbols.

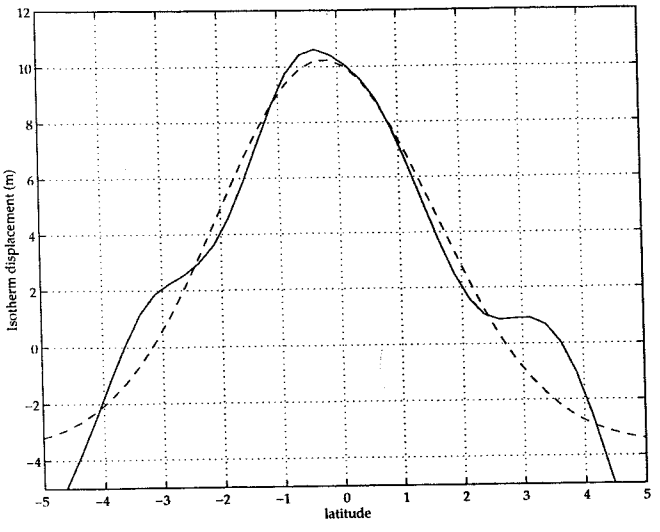

Figure 3.27: 10°C isotherm displacement at 97°W (solid line) in the spring, and Gaussian fit thereto (dashed line). Data are averaged over days 3756–3786 (14th April–14th May) to remove effects of TIWs. The function used to fit the data was $\alpha + A\exp((y-\delta y)^2/2\lambda^2)$ with α, A, δy and λ all free parameters, and data from 10°S to 10°N were used in the calculation.

Kelvin wave. The fit is evidently a good one close to the equator, and the least squares calculation returned a value of 199 km for λ; this is close to the third baroclinic mode value of 193 km in Table 3.1. All in all, this constitutes firm evidence that the seasonal waves in OCCAM are third baroclinic mode equatorial Kelvin waves.

On the other hand, when the zonal velocity structure is considered this interpretation is more difficult to defend. For one thing, as seen in Figure 3.7, at 97°W the maximum in the zonal current occurs during late March, at a time when the

isotherm displacements are close to zero. Such quadrature is typical of Rossby rather than Kelvin waves; for the latter, u and the isotherm displacement η are in phase (*Philander*, 1990). For another thing, the meridional and vertical structure of the u field is more complicated than that of η, and doesn't support the interpretation as a third baroclinic mode Kelvin wave. For instance, Figure 3.28(a) and (b) shows the zonal velocity at the time when it is at its maximum (averaged over 30 days in order to filter out the effects of TIWs). The two most noticeable things about this section are that the dominant baroclinic mode seems to be the fourth one (there being four changes in sign of u between the surface and the sea floor); and that although the meridional structure has patterns which may be characteristic of equatorial waves, these patterns are more complex than the simple Gaussian of the Kelvin wave. As an example, frame (c) of this figure shows the u profile at about 1000 m depth and a fit to this profile which was made in the following way. Firstly a third meridional mode Rossby wave (see equation (A.34), page 131) was fitted to the profile using a non-linear least squares fit in which the Rossby radius was a free parameter. Then a Kelvin wave was fitted to the residual as per the isotherm depth section described earlier. The final fitted curve, which is again clearly a good representation of the section, is the sum of these two waves. The calculated Rossby radii were 140 and 264 km, which from Table 3.1 appear to correspond to the sixth and the second baroclinic modes respectively.

Three other features of the isotherm depth diagrams of Figure 3.25 are worthy of note. Firstly, the Kelvin wave activity continues throughout the year, though with reduced magnitude and generally opposite sign. Three waves can be discerned which are upwelling in the 20°C isotherm and downwelling in the 10°C isotherm. The wave that emerges during May at 180°W appears to change from upwelling to downwelling in the 10°C data, which may be evidence for the mode swapping detected by Giese and Harrison (1990), though this has not been investigated any further. Secondly, the powerful spring wave is seen to reflect off the South American coast (presumably as a Rossby wave). It seems to interact linearly with the incoming waves so as to give the impression of westward group velocity in the latter (this being, of course, impossible for the non-dispersive Kelvin waves). This is most noticeable in the 10°C diagram.

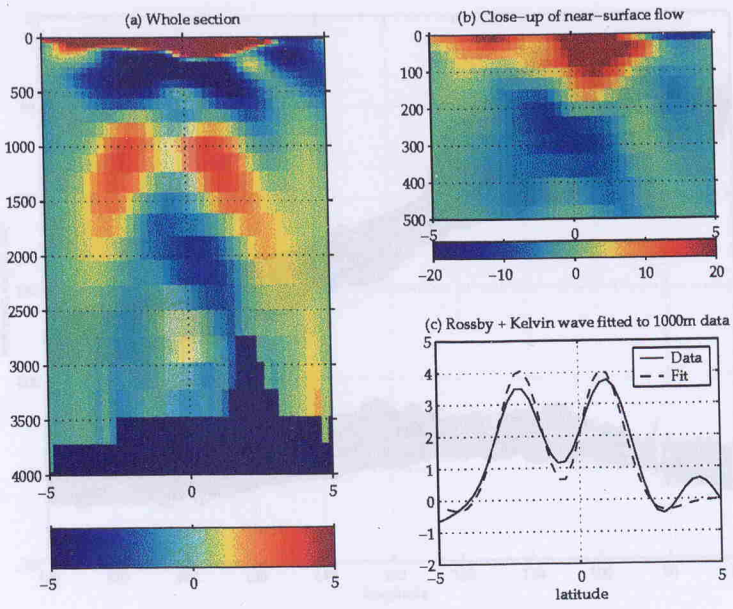

Figure 3.28: (a) u at 97°W averaged over the 30 days centred on day 3741, minus the annual mean. The 30-day averaging is used to filter out TIW effects. Units cm s^{-1}. (b) Close-up of the near-surface flow. (c) Data averaged over levels 17 and 18 (915 to 1236 m), and a fit to this data of the sum of a Kelvin wave and a third meridional mode Rossby wave as discussed in the text.

Thirdly and perhaps most relevantly to the present study are the effects of the Galápagos on the waves. At depth there is little or no effect; waves in the 10°C and 2.5°C isotherm data (the former is at about 425 m) pass unimpeded around the islands. The effect on the shallower regions is best illustrated in conjunction with Figure 3.29, which presents the 15 and 20°C isotherm depth data as superimposed zonal sections. This figure shows that for most of the year the thermocline slopes upwards gradually to 120°W, then more steeply to 105°W. From here to a couple of degrees west of the Galápagos the thermocline is fairly flat but the 15°C isotherm deepens somewhat, so that the thermostad continues to thicken as in the hydrographic data of Lukas (1981; 1986) discussed in Chapter 2. In the last 200 km or so the 20°C isotherm (*i.e.* the thermocline) shoals very rapidly, in agreement with the Bernoulli-type theory of Hendry and Wunsch (1973) considered briefly in section 3.3.2, which we can now assert to be chiefly responsible for the cold tongue enhancement immediately to the west of the islands.

With the coming of the vernal Kelvin wave the situation changes dramatically.

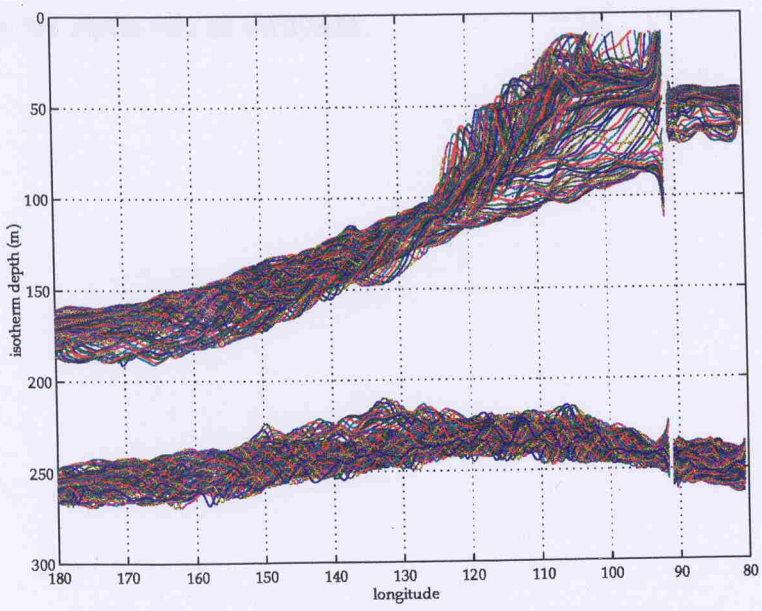

Figure 3.29: 15 and 20°C isotherm depths on the equator for year 10 of OCCAM.

Between 115°W and 93°W the thermocline deepens by about 50 m, and the sign of the large displacement close to the islands is reversed. According to the Bernoulli theory this means that the 20°C isotherm is now below the EUC core (which, as noted earlier, is never found below about 100 m in this region of OCCAM), exemplifying again the decoupling between the temperature and velocity fields. The SST on the west coast of the islands increases correspondingly at this time, but is still low enough to produce a recognisable cold patch; the eastward expansion of high SST is curtailed at or shortly before the longitude of the islands (Figure 3.20). A complementary upward displacement of the 15°C isotherm can also be observed at this time of year.

The difference between the behaviour of the 20°C isotherm east and west of the Galápagos is very striking. The zone of increased variability in the thermocline depth (partly due to TIW activity) which begins at about 115°W comes to an abrupt halt at the islands. Between the islands and the continental coast the isotherm is again horizontal, and for most of the year about 10 m deeper than the corresponding section to the west. Furthermore it undergoes only a relatively modest depression (say 20 or 30 m) as a result of the spring Kelvin wave. These effects on both the transient and the mean properties of the near-surface temperature field constitute our final example of the apparent impact of the Galápagos on the dynamics of the equatorial

East Pacific in the main run of OCCAM.

Chapter 4

Numerical Experiments

Earlier chapters have, I believe, presented compelling evidence that the Galápagos Islands have a significant effect on the near-surface temperature and current structures of the equatorial East Pacific. This evidence is, however, largely diagnostic or circumstantial, rather than mechanistic; the extent to which the phenomena have been fitted into the wider picture of the physical ocean-atmosphere system of the equatorial East pacific is rather limited. In particular, it is not easy from such evidence to disentangle effects due to the wind forcing from effects due to the topography of the islands. The orthodoxy is that the timing, location and temperature of the cold tongue can be explained purely by the seasonal development of the radiative forcing and wind patterns in the region (see *e.g.* Kessler *et al.* (1998)). An SEC divided into barotropically unstable northern and southern branches is likewise a common feature of ocean models having no representation of the Galápagos (*e.g.* McCreary and Yu (1992)). There is therefore a burden of proof on anyone who asserts that these phenomena are even partly due to the presence of the Archipelago.

One rather obvious way of furnishing such proof is to run a believable numerical model of the equatorial Pacific with and without a representation of an equatorial island group, and that is the philosophy behind the work presented in this chapter. In fact, results from two very different models are presented. The first is OCCAM. As described in section 4.1, an integration of some three-and-a-half years has been performed in which the Galápagos were removed (or, more precisely, reduced to a seamount). Chapter 3 has already shown this model to simulate realistically the near-

surface currents and temperatures of the region. The wind and thermal forcing used were exactly as in the main run considered in the earlier chapter, so this represents a clean experiment with a state of the art model incorporating comprehensive physics.

The second model used is a $2\frac{1}{2}$-layer model. This uses greatly simplified physics, particularly as regards the vertical structure of the ocean and the parametrization of sub-grid-scale processes and thermodynamics, in order to enable large numbers of integrations to be performed with relatively limited computer resources. The simplifications also tend to make the interpretation of model results easier whilst still capturing the essential dynamics.

4.1 An experiment using OCCAM

Towards the end of the time during which this study was carried out, the increased availability of computing resources made it possible to perform an integration of OCCAM with the Galápagos removed[1]. This was done simply by taking the model fields for day 3600 (9th November, year 9) of the main run, converting the Galápagos solid earth points to ocean points down to a depth of 500m (the top 13 model levels), and filling in the new oceanic points by linear interpolation from the surrounding data. The model was then run on for 1264 days, using the same forcing as in the main run, finishing on day 4864 (26th April, year 13). The simple method of initialisation was justified *post hoc* by the fact that the resulting unbalanced hydrographic fields did not produce any numerical instability in the model; after an initial burst of inertia-gravity wave propagation out of the modified region, the fields settled down to a smooth and believable state. Surface temperature and salinity are available every 8 model days for the entire run; three-dimensional fields every 15 days for the period 4470–4860 (28th March year 12 to 22nd April year 13) only.

In this section, data from the two integrations are compared in order to assess the islands' impact on the upper ocean in OCCAM. SSTs are considered first; this leads

[1] In fact, an experiment in which the Mediterranean throughflow was blocked off was part of the same integration. We assume that the two experiments did not interact, partly because the experimental integration only lasted a few years.

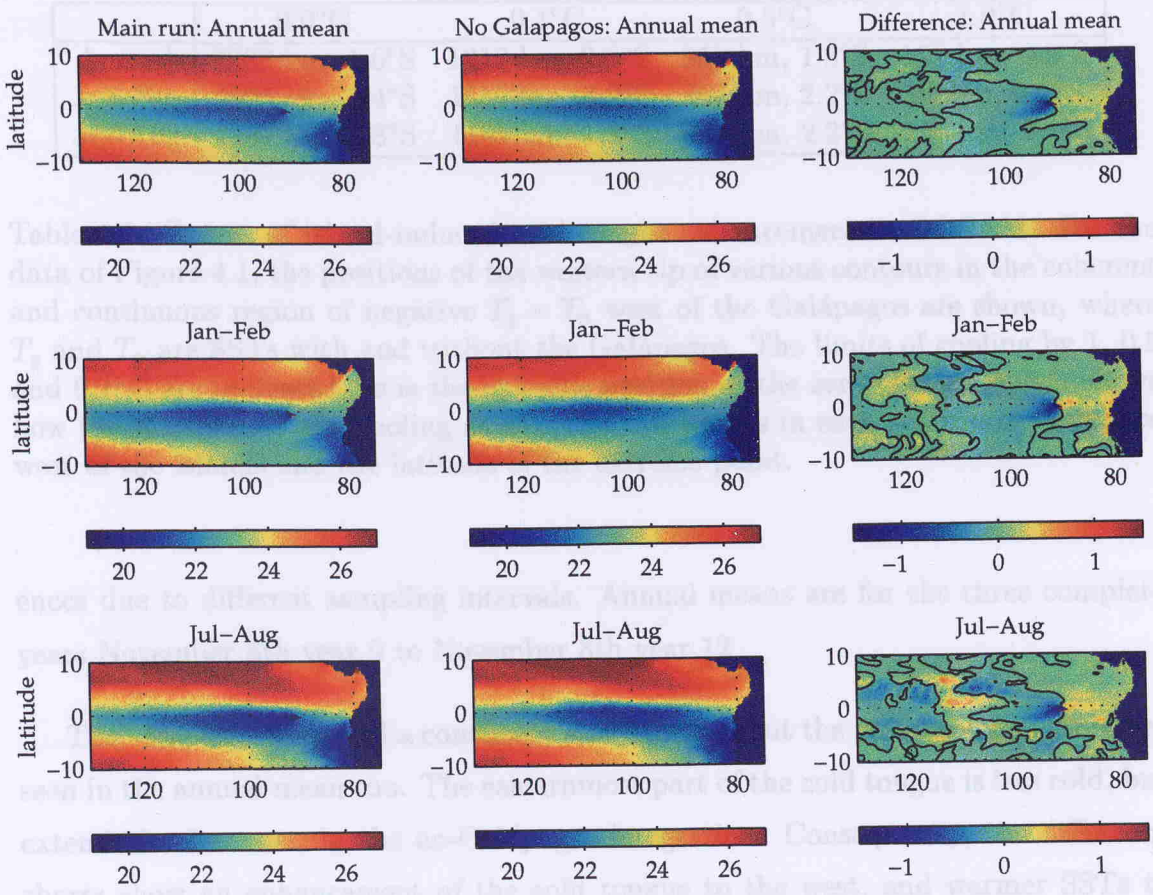

Figure 4.1: Annual and seasonal mean SSTs in OCCAM with and without the Galápagos. Top row: Annual means. Middle row: Means for the bimester January–February. Bottom row: Means for the bimester July–August. First column: Main run. Second column: No-Galápagos run. Third column: Difference (Galápagos minus no-Galápagos), with zero contours plotted. All in °C and composited from data for days 3600 to 4864 inclusive.

naturally on to a consideration of how TIWs are affected. Finally the effects on the EUC are discussed.

4.1.1 SSTs and TIWs

Annual and seasonal (two-monthly or "bimestral") mean SSTs from this integration are compared with data from the main run in Figure 4.1. All means have been calculated from the same set of days (3600 to 4864 inclusive at 8 day intervals), even though more frequent data were available for the main run, to avoid spurious differ-

	0.0°C	0.1°C	0.5°C	1.0°C
Annual	2282 km, 1.6°S	1213 km, 2.5°S	356 km, 1.8°S	122 km, 0.9°S
Jan-Feb	2605 km, 3.4°S	1837 km, 3.2°S	367 km, 2.2°S	89 km, 0.6°S
Jul-Aug	1937 km, 1.8°S	1169 km, 1.9°S	512 km, 2.2°S	156 km, 1.1°S

Table 4.1: Extent of island-induced cold tongue enhancement in OCCAM. For the data of Figure 4.1, the positions of the western tip of various contours in the coherent and continuous region of negative $T_g - T_n$ west of the Galápagos are shown, where T_g and T_n are SSTs with and without the Galápagos. The limits of cooling by 1, 0.5 and 0.1°C are indicated, as is the extreme position of the zero contour which shows how far out there is any cooling at all. The two figures in each cell are the distance west of the islands and the latitude of the extreme point.

ences due to different sampling intervals. Annual means are for the three complete years November 8th year 9 to November 8th year 12.

The seasonal means tell a consistent story throughout the year, which is therefore seen in the annual mean too. The easternmost part of the cold tongue is less cold, but extends further east, in the no-Galápagos integration. Consequently, the difference charts show an enhancement of the cold tongue to the west, and warmer SSTs to the east, of the islands in the main run. The maximum island-induced cooling varies between 1.5°C in Jan–Feb and 1.9°C in Jul–Aug, with an annual average of 1.7°C, and is always found on the west coast of the islands. Table 4.1 shows that this cooling falls off quite rapidly to the west, a cold tongue enhancement of 1°C or more never being found much more that 150 km away from the islands. On the other hand, a cooling of 0.1°C (a temperature difference which is thought to be climatologically significant at least in the *western* Pacific) exists for at least 1000 km to the west at all times, as do coherent cooling structures of at least 2000 km extent or so. Note too that the enhancement is principally to the south of the equator, as in the expansion of the cold tongue away from the Galápagos in Figure 3.3. Likewise, locally to the islands the pattern extends to the south-west, in line with Houvenaghel's observations of the seasonal cycle of SST in the region, discussed in section 2.1.1.

Figure 4.2 illustrates the effects on SST on a regional scale. Timeseries of main run SST and the difference in SST between the two runs are shown, averaged over three different geographical areas: the Niño-3 region; the region where Figure 4.1

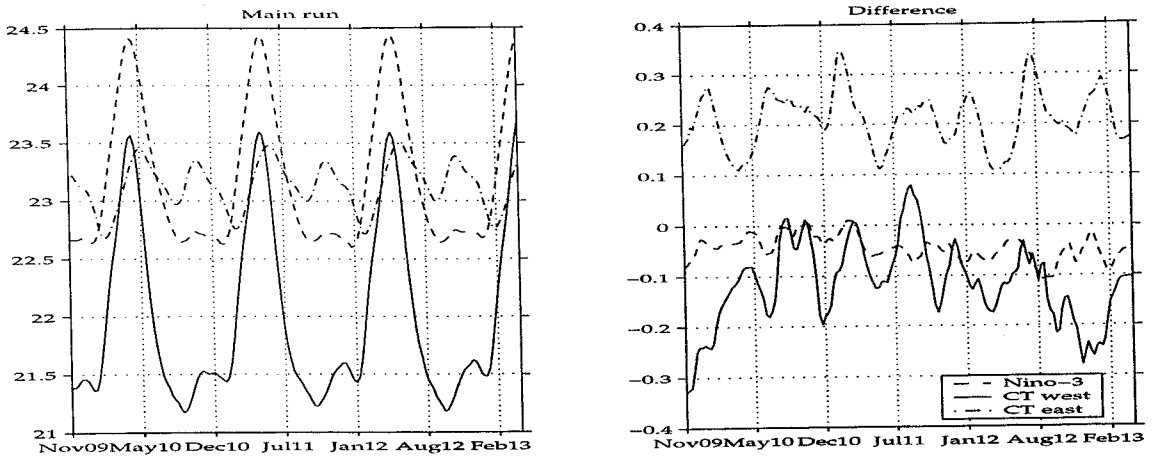

Figure 4.2: SST from main run (left panel) and SST difference between main run and no-Galápagos integration (right panel), averaged over the following three regions: (1) Niño-3: 90–150°W, 5°S–5°N; (2) 91.5–115°W, 2°S–2°N ("CT west"); (3) 80°W–90°W, 2°S–2°N ("CT east"). A 5-point rectangular filter (centred running mean) has been applied to the 8-daily data. Dates are in the form mmmyy where 'mmm' is a string specifying the month and 'yy' an integer specifying the year.

suggests the enhanced cooling due to the islands to be greatest; and the region east of the island where the truncation of the cold tongue by the islands produces the greatest warming relative to the no-Galápagos scenario (*i.e.* the band from 2°S to 2°N between the islands and the South American coast). The series cover the $3\frac{1}{2}$-year period for which reasonably frequent (8-daily) SST data are available for each run.

Considering first the SST timeseries in the left-hand panel, we note that the area-mean SSTs to the west of the island are dominated by an annual cycle with a maximum in the northern spring. This maximum suppression of the cold tongue is due to the seasonal Kelvin wave discussed in section 3.5. To the east of the islands, on the other hand, the dominant harmonic is the semi-annual one (*cf.* Figure 3.5).[2] As noted elsewhere, this is what would be expected if the SSTs were being determined by the insolation, but this mechanism is not available to OCCAM. Neither the Levitus SSTs nor the ECMWF winds used to drive the model has a dominant semi-annual cycle except in very limited geographical areas (of a few grid boxes in dimension). Hence the semi-annual cycle east of the Galápagos must be determined by the model

[2]The ratios of the annual to semi-annual harmonic amplitudes for the three areas are respectively 2.1, 1.8 and 0.5.

Region	A 10^6 km^2	ΔT °C	ΔE 10^6 TJ	δE MJ m^{-2}
Niño-3	7.4	−0.04	−27	−3.7
CT west	1.2	−0.12	−11	−9.5
CT east	0.5	0.21	9	17.2

Table 4.2: Time mean differences (main run minus no-Galápagos run) of various quantities, averaged over the three areas defined in Figure 4.2. A – area of region. ΔT – change in top layer temperature. ΔE – change in top layer internal energy. δE – change in top layer internal energy per unit area. Energies calculated using specific heat capacity and density of water at 20°C and 35 psu.

dynamics, either as an internal mode of variability or by filtering out the annual cycle in the forcing. Interannual variability in these area mean quantities seems rather slight, although the secondary peak in the cold tongue SST does seem to be increasing with time.

The semi-annual cycle in the region between the islands and the continent is also apparent in the timeseries of differences between the two runs, in the right-hand panel of Figure 4.2. Despite this oscillation, the no-Galápagos run is warmer in this region at all times, by at least 0.1°C. The Niño-3 region is likewise almost always cooler, by about 0.04°C on average. The differences in the apparently most affected "CT west" region are more variable. In particular the SST is *higher* here in the main run during the late northern summer of year 11. As we shall shortly see, this was a time when TIWs were particularly active in the main run, compared to the no-Galápagos integration. It would appear that the concomitant enhanced lateral mixing of cool (warm) water away from (towards) the equator is sufficient to reverse the islands' direct cooling effect on the cold tongue at this time. Apart from this period, the SSTs are consistently lower in the main run, the average temperature difference being 0.12°C. Although these differences are quite small, it must be remembered (a) that they are averaged over horizontal areas of the order of a million square kilometres; and (b) that they are mean values for the top 20 m of the model ocean. The implied amount of internal energy redistribution is therefore large, of the order of tens of millions of TJ (see Table 4.2).[3]

A number of other features in Figure 4.1 are worthy of note. Firstly, even in the

[3] 1 TJ (terajoule) = 10^{12} Joules.

no-Galápagos integration the cold tongue is not simply a westward continuation of the South American coastal cold region. Even when the cold tongue is well developed during the northern summer, its equatorial minimum is at about 100°W. The axis of minimum temperature in the coastal region is at about 4°S and is not continuous with that of the cold tongue. This provides yet further evidence that westward expansion of the coastal upwelling region plays little or no role in the production of the cold tongue proper.

Secondly, the Jan–Feb composite shows a region along the continental coast where the surface temperatures in the main run are about 0.5°C higher than those in the run in which the Galápagos were absent. This is especially true south of the equator but can also be seen to the north. One way in which low SSTs can be produced along this coast is by the division into two coastal Kelvin waves of an incoming upwelling equatorial Kelvin wave. Indeed, given that the wind forcing is the same in the two integrations, this is the mechanism which is most likely to be involved here. A time-longitude diagram of 20°C isotherm depth from the no-Galápagos integration (unsurprisingly) shows the large spring downwelling wave passing the longitude of the islands relatively unmolested (as compared to the wave in the main run seen at Figure 3.25), and it is likely that the same applies to the weaker upwelling waves found at other times of the year.

A third noteworthy feature of Figure 4.1 is the band of relatively high SSTs just north of the equator in Jul–Aug of the no-Galápagos run, which begins just west of the 100°W meridian and extends to about 117°W. A similar though less pronounced band can be discerned south of the cold tongue. Comparing the two individual seasonal means, we see that the reason for this is that the cold tongue is narrower in this region in the main run. Enhanced horizontal mixing due to increased TIW activity is a likely candidate for this erosion of the cold tongue. The infrequency of available data from OCCAM renders impracticable a direct proof of this by means of calculation of eddy Reynolds fluxes $\overline{v'T'}$. In particular, the fact that v is available only every 15 days for just one year of the no-Galápagos integration (and for most of the main run) leads to serious aliassing problems—the "background" state against which the departures v' are calculated is dominated by features having a wavelength of about 500 km at 4°N.

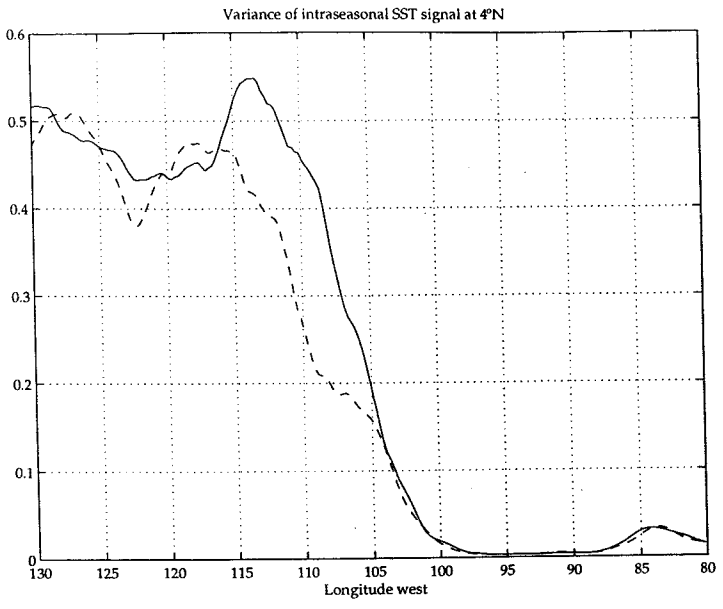

Figure 4.3: Variance of intraseasonal SST fluctuations at 4°N in the main run (solid line) and the no-Galápagos run (dashed line) of OCCAM. Calculated from 8-daily data from years 10–12 inclusive (days 3656–4744; 4th January year 10 to 27th December year 12). "Intraseasonal" in this context is defined in the text. Data have been smoothed with a 9-point rectangular filter to remove aliassing effects. Units $(°C)^2$.

Similar considerations apply to the other Reynolds fluxes and the energy conversion terms. However, it is possible to show that TIWs are more energetic in this region in the main run, using the 8-daily SST data (the differences observed being on a larger spatial scale than the $\frac{1}{4}$-wavelength we would expect if aliassing were a problem here).

Figure 4.3 shows the variance of the "intraseasonal" component of the SST variability at 4°N with and without the Galápagos, over the three complete years (10 to 12) for which data are available for both runs. The intraseasonal component at any longitude is defined as the total SST timeseries at that longitude minus annual and semi-annual harmonics as determined using a least squares fit. As observed in Figure 3.20, this component is strongly dominated by TIWs. It is clear from Figure 4.3 that TIWs are on average more active in the main run from 105°W to 115°W, the region where we have just noted a greater erosion of the cold tongue in this run. Outside this longitude range the variance is approximately the same in the two integrations.

Figure 4.4 visualizes the two-dimensional distribution of the variance and the

differences between the two runs. As with the mean SSTs of Figure 4.1, the patterns are broadly very similar in the two cases. The total variance is dominated by the seasonal cycles associated with the Peru-Chile upwelling region and the south side of the cold tongue. The difference chart shows clearly that the variability as well as the coldness of the cold tongue is enhanced to the west or south-west of the Galápagos, with a corresponding decrease to the south and east. There is another marked increase in the variance at about 5°S and just west of the islands, *i.e.* in the region where we are claiming that TIW activity will be enhanced by the islands. A corresponding region north of the equator shows up more clearly in the intraseasonal variance difference chart. Both north and south of the equator we find regions further west where the variance is *smaller* (and the SSTs of Figure 4.1 higher) in the main run. This does not necessarily imply that the TIWs are more vigorous here in the no-Galápagos integration; by the time they reach these longitudes, the cold tongue waters might already have been mixed by the main run TIWs to the extent that meridional oscillations associated with the waves have less of a signature in the SST field.

We have hypothesized that the extra TIW activity in the main run is due to barotropic instability of the island tip jets whose existence in reality was established in sections 2.1.2, 2.2.2 and 3.4. This hypothesis is corroborated by Figure 4.5.

Part (a) of this figure shows the difference between the mean surface u of the two runs. Two things are particularly clear. Firstly, in the no-Galápagos run the SEC is divided into two separate jets all the way to the South American coast, whereas in the main run this is true only west of the islands (*cf.* section 3.4). This ties in with our earlier observation that the cold tongue exists to the east of the longitude of the islands in the no-Galápagos run; upwelled EUC/thermocline waters are responsible for low equatorial SSTs as well as relatively eastward equatorial currents. Secondly, where they do exist (*i.e.* at and to the west of the islands) the jets are much more intense in the main run. We might predict that the extra shear implied by this would tend to make the flow more unstable, and this is borne out by frames (c) and (d), where the vorticity gradients involved in the Kuo criterion (see page 87) are plotted for the two cases. North of the equator the region of negative absolute vorticity

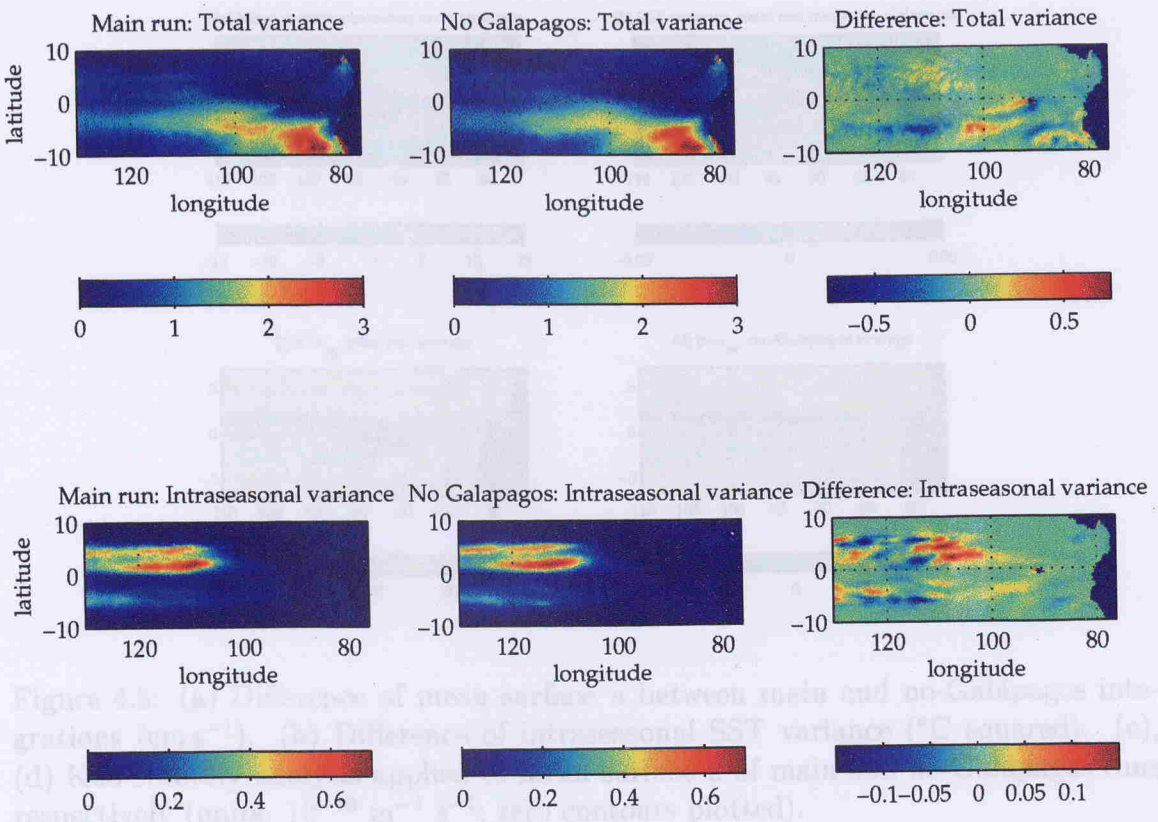

Figure 4.4: SST variance from OCCAM with and without the Galápagos, in $(°C)^2$. What is plotted in each frame is indicated by the title. Variances calculated for days 3600 to 4864 at 8-day intervals; "intraseasonal" has the same meaning as elsewhere in this section. Aliassing effects have been smoothed out of the intraseasonal variances using a 9-point rectangular filter in the zonal direction.

gradient is broader in the main run (though, interestingly, it begins at about the same longitude when the islands are absent). In the south the criterion is satisfied only when the islands are present. Frame (b) shows the intraseasonal SST variance, our rough indicator of TIW activity (this is just a close-up of the corresponding frame in Figure 4.4). Increased variability in the vicinity of the unstable island jets, especially the southern one, is very clear in this diagram.

One surprising feature of the filtered SST timeseries used to compile Figure 4.3 is the large amount of interannual variability; for instance, whereas the variance plot for year 11 shows a very large decrease from the main to the other run between 105 and 115°W, the differences are much smaller for years 10 and 12 (though the variance is always larger for the main run over this range of longitudes). These issues are further

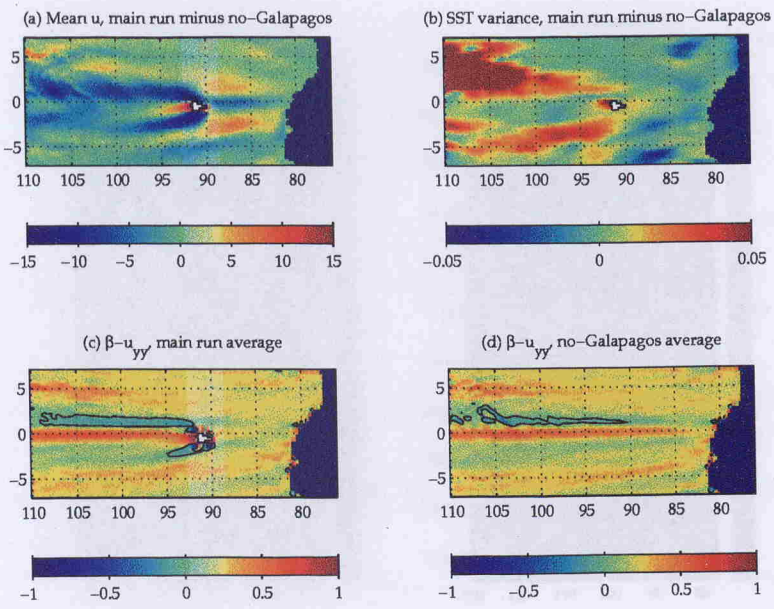

Figure 4.5: (a) Difference of mean surface u between main and no-Galápagos integrations ($\mathrm{cm\,s^{-1}}$). (b) Difference of intraseasonal SST variance (°C squared). (c), (d) Kuo stability analysis applied to mean surface u of main and no-Galápagos runs respectively (units: 10^{-10} $\mathrm{m^{-1}\,s^{-1}}$; zero contours plotted).

illustrated in Figure 4.6, where the filtered time-longitude data are presented in full. Regarding differences between the two runs, we can see that the TIWs begin further east in the main run during year 11 and during June to September of year 12, whereas the opposite is true during the early part of the TIW season of year 10 and the later part of year 12. For a couple of examples of interannual variability, compare the later part of the TIW season in year 11 of the main run with that for year 12, when there is little or no TIW activity east of the 110°W meridian; or the TIW seasons of years 10 and 11 of the no-Galápagos integration. These observations may be contrasted with the behaviour between 80°W and 90°W. Here, the two short-lived TIW-like oscillations between February and May are visually the same between the two runs and between different years of the same run. These oscillations are presumably a reproducible response to the annual cycle of the winds, whereas in detail the TIWs exhibit some chaotic aspects, the longitude of their inception in particular being sensitive to small changes in the ambient conditions, or to larger perturbations such as the introduction or removal of the Galápagos. As another example of the generally small interannual variability in the model, typical differences between annual mean

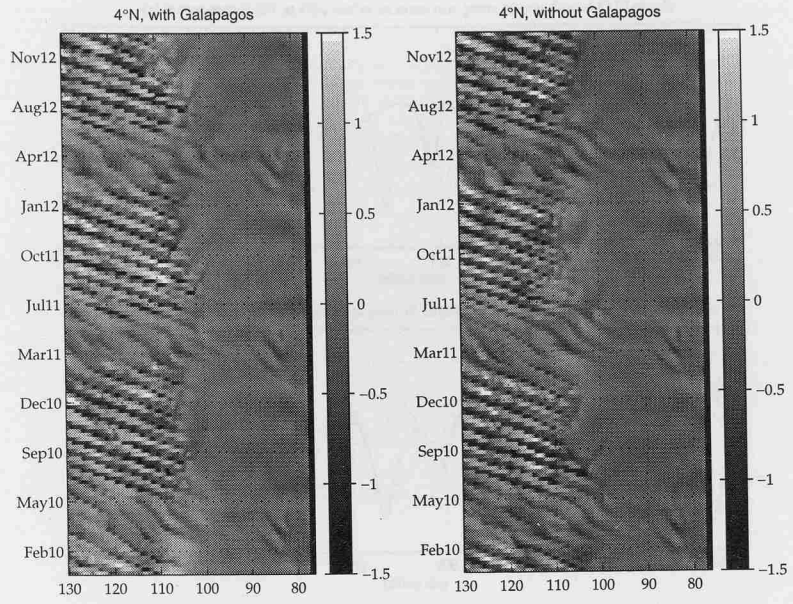

Figure 4.6: Time-longitude diagram of the data used to compile Figure 4.3.

SSTs of different years, averaged over the area of Figure 4.4, are around 0.05°C; and most of this is due to relatively large differences (up to about 0.4°C) in the TIW regions, which are affected by aliassing as discussed earlier.

That the timing of the TIWs is another of these "chaotic" aspects is clearly illustrated by Figure 4.7, where timeseries of the filtered SST fields at 4°N, 120°W are compared. At this longitude the variance in the two runs is similar. Part (a) of the figure compares data from two years of the main run. Differences of up to two days in the timing can be accounted for by the fact that the year 10 series begins on 4th January and the year 12 series on the 2nd (both continuing at 8-day intervals). However there are several times when the phase difference is greater than this. For instance, the first clear TIW signal in the season beginning in year 12 is the SST minimum at about Julian day 170, whereas there is no such signal until about day 200 of year 10. As another example, the intraseasonal SST maxima at days 204 and 218 in years 10 and 12 respectively indicate TIWs that are in antiphase at this time of year. Part (b) of Figure 4.7 demonstrates a similar lack of coherence between the data for year 11 in the two integrations. The two series are, for instance, clearly in antiphase at about day 250. These results contrast with those of Allen *et al.* (1995), who present evidence that the timing of TIWs is determined by the wind forcing (and

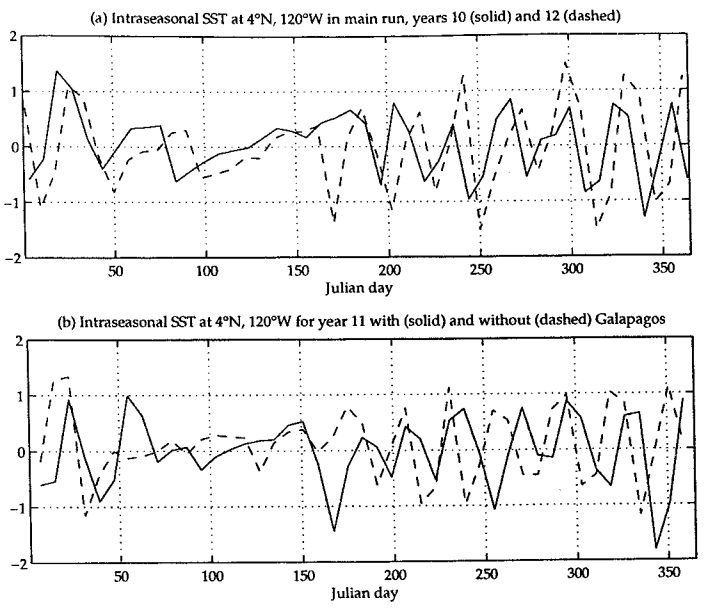

Figure 4.7: Timeseries of intraseasonal SST fluctuations at 4°N, 120°W. (a) From years 10 (solid line) and 12 (dashed line) of the main run of OCCAM. (b) From year 11 of OCCAM with (solid line) and without (dashed line) the Galápagos.

especially by sporadic and remote wind stress episodes such as WWBs).

4.1.2 The EUC

Figure 4.8 depicts the zonal current at the depth of the EUC core in each of the integrations, at a time (late December) when the EUC is beginning to build towards its spring maximum (see Figure 3.7). This figure illustrates vividly that the meanders in the EUC between 90°W and the South American coast, identified as inertial or possibly Rossby waves at section 3.3.2, are indeed due to the presence of the islands; no such meanders are ever seen in the no-Galápagos integration. The figure also provides an example of the division of the EUC into two branches as it passes round the islands, with the northern branch being the stronger and the two branches reuniting a short distance downstream, which was also noted earlier.

A third feature highlighted by Figure 4.8 is the effect of the islands on the EUC transport. Even though u rather than the speed $|\mathbf{u}|$ is shown here[4], it is clear that

[4]The meridional component v will make a contribution to the transport in the meandering region.

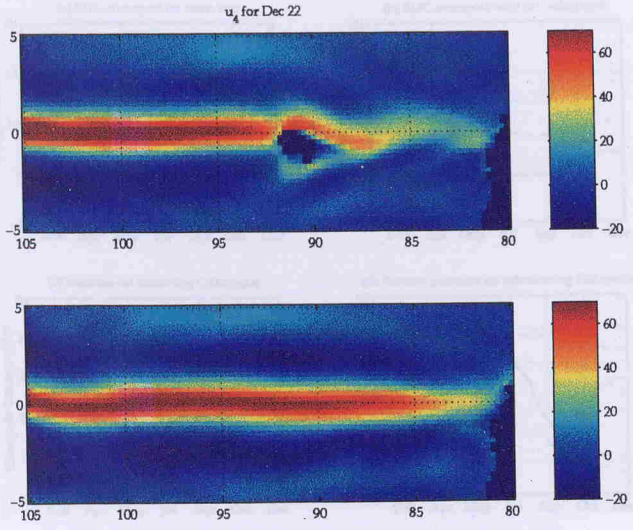

Figure 4.8: u for OCCAM level 4 (76 m) with (top) and without the Galápagos, for late December of years 10 and 12 respectively. Units cm s^{-1}.

the EUC east of the longitude of the islands is feebler in the main run than it is when the islands are removed. This observation is made quantitative in Figure 4.9, which shows timeseries of EUC transport at four longitudes (two on each side of the islands), for representative years of each of the integrations. Differences between the two runs are also given, both in Sverdrups and as a percentage decrease on introducing the Galápagos.

Both integrations show the same annual cycle in the EUC transport, with the marked spring maximum and comparatively small values at other times noted in earlier chapters. Eastward propagation of the spring pulse is evident in both series. In both series the transport decreases from west to east at all times, but the decrease from 95°W to 88°W (*i.e.* from one side of the islands to the other in the main run) is much more pronounced when the islands are present. Specifically, for the filtered series presented here the average percentage decrease between these two longitudes is 47% (with a standard deviation of 10%) when the islands are present, but only 27% (standard deviation 4%) when they are absent. Calculation of terms from the mean u-momentum equation (after Wacongne (1989)) confirms that the extra deceleration is due mainly to the adverse pressure gradient west of the islands associated with the hydraulic effects discussed especially in section 3.3.2. Enhanced mixing (horizon-

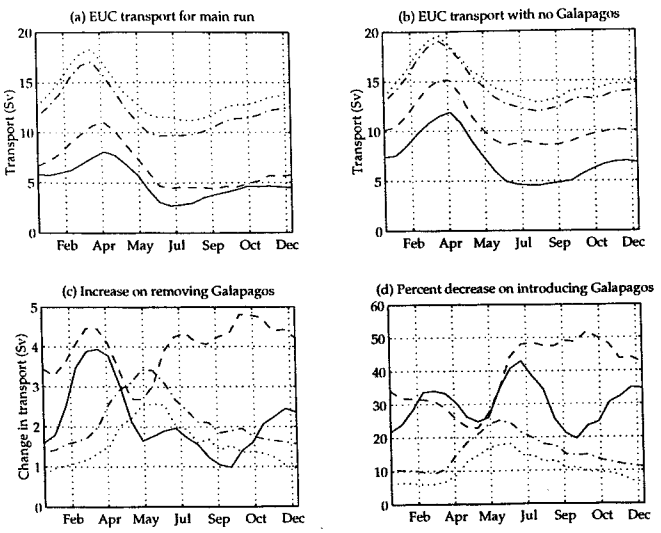

Figure 4.9: Timeseries of EUC transport (Sv), as defined on page 64, for (a) main run, (b) no-Galápagos integration of OCCAM. Transports at 97°W (dotted line), 95°W (dot-dash), 88°W (dashed) and 85°W (continuous) are shown. 15-daily data filtered using 5-point centred running mean. (c) Change in transport effected by removing the Galápagos. (d) Change as a percentage of the no-Galápagos transport.

tal and vertical diffusion of momentum) in the vicinity of the islands only makes a contribution of the order of 1% of that due to the hydraulic effect.

The difference timeseries in Figure 4.9 show that the biggest effect of the Galápagos is to the east, where the spring peak in EUC transport is decreased by about 4 Sv or 30%. At 88°W the absolute decrease continues at about the same level for the rest of the year, the percentage decrease being correspondingly larger, whereas at 85°W the decrease in transport is smaller during the months when the EUC is weak, so that the percentage decrease remains about the same. Perhaps more surprising is that a reflection of the spring pulse off the islands seems to have a large effect on the upstream transport. Even at 97°W, some 600 km from the islands, the transport is reduced by 2.5 Sv, or nearly 20%, during May and June.

As a final diagnostic, the trajectory calculations of section 3.3.2 have been repeated using data from the no-Galápagos integration. The calculations covered the same dates, but of year 12 instead of year 10. Qualitatively the trajectories are as might be expected. There is no meridional deflection as the particles pass the

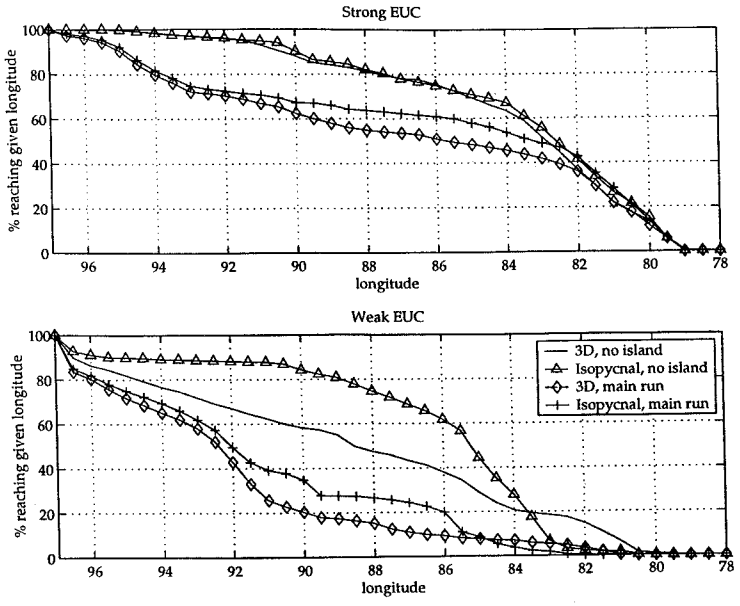

Figure 4.10: Percentage of trajectories reaching each longitude east of 97°W for strong (top) and weak EUC, with and without the Galápagos, for each of two different trajectory calculation methods. *Cf.* Figure 3.12.

longitude of the islands (though with 3D velocities there are some small vertical displacements – remember that the islands were only truncated to a depth of 500 m), nor any meandering between this longitude and the continent. As in Chapter 3, the percentage of particles reaching a given longitude east of the starting position has been used as a measure of the eastward penetration of the EUC. The results are compared with those from the main run in Figure 4.10, which again (*cf.* Figure 3.12) presents data for both "3D velocity" and isopycnal integrations. When the EUC is strong the results are clear and consistent. For the main run, only about 65% of the particles travel beyond the east coast of the islands, whereas when the islands are removed about 90% of the trajectories reach these longitudes. The difference remains at least 15% until 84°W, where the influence of the islands diminishes and the EUC is decelerated principally by a negative zonal pressure gradient originating at the South American coast.

When the EUC is weak the results are equally clear but less consistent. The trajectories again reach significantly further east when the islands are absent, but this is much less true of the 3D velocity trajectories than it is for the isopycnal ones.

Many of the former are carried upwards into the top model layer and subsequently advected westwards by the SEC, whereas the isopycnal trajectories remain confined beneath the top level and are not exposed to the full force of the SEC.

Nevertheless, this does not affect the main result: the trajectory calculations confirm the implication of the transport and u snapshot diagnostics that the EUC is significantly curtailed by its interaction with the Galápagos.

4.2 Experiments with a $2\frac{1}{2}$-layer model

My original intention to use a simplified model as the principal means of investigating the behaviour of the ocean with and without the islands was superseded by the no-Galápagos integration of OCCAM which has just been discussed. Nevertheless, the $2\frac{1}{2}$-layer model is able to shed further light on the mechanism of cold tongue enhancement, and this is what shall be considered in this section.

A detailed description of the model is presented as Appendix C. This model was chosen for the following reasons.

1. Being a reduced gravity (RG) model, fast barotropic motions are *a priori* filtered from the model, which enables a relatively long timestep to be used. This, coupled with the small number (two) of active layers in the model, enables the model to be run with rather limited computing resources. In the configuration used here, the model takes about 10 seconds cpu to run on one processor of a high performance unix machine. As integrations of at most a few years were generally required, this meant that many runs could be performed on readily available computers, in order to test the model's sensitivity to the choice of its adjustable parameters and, more importantly, to examine the system's response to various forcing régimes.

2. Unusually among RG models, the one used here has horizontally varying temperatures. This enables the effect of the forcing and topography on the SSTs to be studied directly, rather than by using the thickness of the top layer as a crude proxy as is sometimes done.

3. Earlier incarnations of this model have been used in many process modelling studies of the equatorial Pacific (*Cane*, 1979; *Schopf and Cane*, 1983; *Schopf and Harrison*, 1983; *McCreary and Yu*, 1992; *McCreary and Lu*, 1994; *Lu and McCreary*, 1995; *Lu et al.*, 1998). The model is therefore well-known to simulate the circulation of this ocean sufficiently well for such purposes. This reduced the amount of time required to develop the model.

For the canonical or "control" integration, the model was configured as follows:

- Grid spacing 0.5° in latitude by 1° in longitude.
- Rectangular closed basin from 135°E to 75°W and from 30°S to 30°N.
- Galápagos represented by a rectangular island extending from 1°S to 1°N and from 90°W to 91°W – *i.e.* 2 grid boxes in the zonal by 5 in the meridional directions.
- Mixing parameters (see Appendix C): $\nu = 5 \times 10^7 \mathrm{cm^2\,s^{-1}}$, $\kappa = 2 \times 10^7 \mathrm{cm^2\,s^{-1}}$, $\kappa_m = 0.2\,\mathrm{cm^2\,s^{-1}}$, $t_e = t_d = 3\,\mathrm{hr}$, $h_1^{min} = h_2^{min} = 20\,\mathrm{m}$.
- Forced with zonal mean, annual mean wind stresses from the same ECMWF dataset as used by OCCAM. The zonal stress τ_x is everywhere towards the west, with a local minimum of about 0.2 dynes $\mathrm{cm^{-2}}$ on the equator, and local maxima of 0.45 and 0.58 dynes $\mathrm{cm^{-2}}$ at 15°S and 15°N respectively. Polewards of these latitudes the stress tails off to approximately zero at the northern and southern boundaries of the model domain. The meridional stress τ_y is convergent onto the equator, with extrema of 0.2 dynes $\mathrm{cm^{-2}}$ and -0.25 dynes $\mathrm{cm^{-2}}$ at 15°S and 15°N.
- Climatological SSTs for initialization and relaxation: annual mean Levitus 94 values, linearly interpolated onto the model grid and then smoothed with a 17 by 35 point rectangular window.
- Initial layer thicknesses $h_1 = 75$ m, $h_2 = 175$ m. This implies equatorial Rossby radii of 373 and 233 km for the two vertical modes, the corresponding gravity wave speeds being 3.17 and 1.24 $\mathrm{m\,s^{-1}}$.

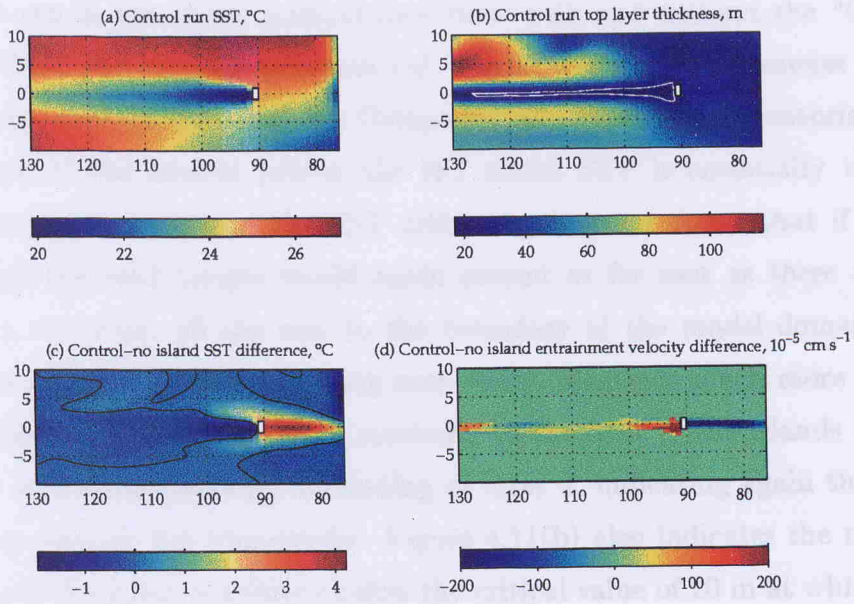

Figure 4.11: Effect of island on SST in main run of $2\frac{1}{2}$-layer model. The small white rectangle is the island. (a) SST averaged over fifth year of integration. (b) Top layer thickness h_1. 20 m contour in white. (c) Difference of SST between runs with and without island. Zero contour in black. (d) Difference of entrainment velocity w_1 between these runs.

Layer 2 temperatures were also initialised using Levitus 94 data, averaged over a suitable set of levels in the vertical. This appeared to ameliorate the long-term upward drift in layer 2 temperature reported by McCreary and Yu (1992), who used a spatially constant initial value. The passive layer is held at 0°C. The layer 2 temperatures were smoothed in the same way as those for the top layer. This degree of smoothing is quite sufficient to remove any trace of an island effect in the thermal forcing; using a zonal mean wind stress likewise ensures that any zonally inhomogeneous dynamical effects are due to the island/basin configuration.

In all the integrations reported here, the model was spun up for four 360-day "years" (from a state of rest), after which time a statistically stationary[5] state is reached. Each integration was then continued for a further year with diagnostics being saved.

Figure 4.11 shows the most important results from the experiment in which the

[5] Or, for integrations with repeat annual cycle forcing, periodic.

model was run in the above configuration both with and without the "Galápagos". As in OCCAM and the satellite data (*cf.* Figure 3.4) the most intense part of the cold tongue occurs just west of the Galápagos, and there is no equatorial minimum of SST east of the islands (where the RG model SST is essentially the same as the climatological forcing). The SST difference diagram shows that if the islands were absent the cold tongue would again extend as far east as there are easterly winds – in this case, all the way to the boundary of the model domain, which is one reason why the relative warming east of the islands is much more pronounced in this model. The top layer thins markedly to the west of the islands (frame (b)), and there is a complementary thickening of layer 2, indicating again that the EUC is piling up against the topography. Figure 4.11(b) also indicates the region where the top layer thickness is reduced below the critical value of 20 m at which the crude parametrization of mixed layer dynamics starts to cause rapid entrainment of layer 2 water. This is the principal mechanism for establishing the cold tongue in this model, further confirmation being provided by the difference in mean entrainment velocity plotted in frame (d). The ratio h_1/h_2 is also below its critical value in this region, so that "background diffusion" is also contributing to entrainment, *i.e.* cooling.

It will be observed that the cold tongue is broader than the region where entrainment is active. This spreading is achieved by horizontal mixing, both of the unresolved kind parametrized by Laplacian diffusion with an eddy coefficient, and of the resolved kind – TIW-like motions are present in this model. The various types of TIW found in the model are discussed by McCreary and Yu (1992), but are essentially the usual mixture of Rossby and Rossby-gravity waves.

This explanation for the broadening of the cold tongue was confirmed by a sequence of sensitivity runs in which the viscosity was progressively decreased. In general, the smaller the viscosity the higher the equatorial temperatures (as measured, for instance, by means over the three areas introduced in section 4.1.1). This is consistent with the finding of McCreary and Yu that "TIW" activity, and hence lateral mixing, increases with decreasing viscosity (on the "quasiperiodic route to turbulence").

The cold tongue effect is particularly clear and particularly large in this experiment

Expt.	Niño 3	CT west	CT east
1	−0.08	−0.50	2.73
2	−0.01	−0.06	0.04
3	−0.09	−0.28	0.67
4	−0.04	−0.21	0.07
5	−0.00	−0.07	0.19

Table 4.3: Change in area mean SST (ΔT) between with-island and no-island runs of $2\frac{1}{2}$-layer model, for the five different forcing regimes listed in the text. The three areas are as defined in section 4.1.1 (caption to Figure 4.2). All in °C.

with zonal mean winds. How the model responds to other variants of the forcing is summarised in Table 4.3. This table shows changes in annual mean SST between runs with and without the islands for various forcing regimes, averaged over the three areas defined in section 4.1.1. The five experiments are respectively forced by:

1. Zonal mean, annual mean wind, smoothed annual mean SST (as discussed above).
2. Smoothed annual mean wind, smoothed annual mean SST.
3. Smoothed time-varying wind (interpolated from monthly means), smoothed annual mean SST.
4. Unsmoothed time-varying wind, smoothed annual mean SST.
5. Unsmoothed time-varying wind, unsmoothed time-varying SST.

It will be seen that the introduction of an island consistently gives rise to a cold tongue enhancement to the west and a warming to the east of the island. The magnitude of the effect varies significantly with the forcing. In particular, the eastern warming is much reduced when winds are used which are not easterly all the way to the eastern boundary of the model, so that the cold tongue is not so well developed in the no-island integrations. Nevertheless, these $2\frac{1}{2}$-layer model integrations both confirm the fundamental result of the thesis and emphasize the role of increased vertical mixing due to topographically induced thinning of the mixed layer in producing the cold tongue enhancement.

Chapter 5

Discussion and Conclusions

5.1 Summary of Results

The main substantive conclusions of this thesis are:

1. Under normal (non-El Niño) conditions, the Galápagos form a well-defined eastern cut-off point of the equatorial Pacific Cold Tongue; westward expansion of the Peru-Chile upwelling zone makes at most a secondary contribution to the development of the cold tongue in this region, and is most significant to the south of the cold tongue proper (2.1.1, 2.2.1, 3.2)[1].

2. Were the islands not present, the cold tongue would extend some hundreds of kilometres further east, at least to the eastern limit of easterly winds on the equator (4.1.1).

3. The island-induced cooling is such that the SST difference between the east and west coasts of the islands is typically about 2°C and as much as 8°C at times (2.1.1, 3.2). Modelling studies suggest that on larger (regional) scales the effect is more modest – of the order of 0.1°C – but this may be an under-estimate due to the model SSTs being constrained by the climatological forcing (4.2, 4.1).

4. This cooling is effected mainly by enhanced upwelling and westward advection of EUC waters (2.1.1, 3.3.3, 4.1.2), though a decrease in mixed layer thickness

[1]Numbers in brackets refer to the section(s) where evidence for these conclusions can be found.

with consequent enhanced entrainment also plays a role (4.2).

5. Despite their modest latitudinal extent, the Galápagos have a marked effect on the EUC as it approaches its eastern terminus (2.1.2, 3.3.2, 4.1.2):

   - A hydraulic or Bernoulli effect as the current runs into the islands causes the upwelling of the surface waters noted above, together with a downwelling below the EUC core. The current then divides into two branches, with about 3/4 of the transport being carried by the northern branch, and the fluid particles undergo further vertical excursions of some tens of metres, in the opposite direction to those they experienced to the west of the islands.

   - The two branches usually reunite less than 100 km downstream of the islands, to complete a potential-like flow around the obstruction, but occasionally separation occurs and they remain distinct for about 400 km.

   - Following their north- or southward deflection, the particles undergo inertial oscillations about the equator causing the downstream EUC to meander.

   - The EUC loses about 47% of its transport during its interaction with the islands, compared to the 27% it would lose over the same range of longitudes were the islands not present. Put another way, the transport east of the islands is about 70% of what it would be in the absence of the archipelago, decreasing to 50% at times when the EUC is weak. Because of the retroflection, the upstream EUC transport is also affected, by up to 20%.

6. The Galápagos also form the eastern limit of the region where the SEC divides into a northern and a southern branch. The behaviour of the SEC as it strikes the archipelago is consistent with the theory of low-frequency flows past equatorial islands, though the existence of a divided SEC in models with no representation of the islands suggests that this is not the whole story (2.1.2, 2.2.2, 3.4.1).

7. These two SEC jets are intensified by the presence of the islands, to a degree which makes them more susceptible to barotropic instability. This has the effect of making TIWs more vigorous between 105°W and 115°W, with consequent effects on the equatorial SST patterns, including a partial offsetting of the cold tongue enhancement noted above (3.4.2, 4.1.1).

Some further observations were made in passing, including:

1. Equatorial wave activity with periods of 20–30 days and wavelengths of around 1000 km, generally identified as TIWs, consists of two distinct components: (a) a high baroclinic mode Rossby-gravity wave which can be identified even to the east of the Galápagos, and (b) a first baroclinic mode, first meridional mode Rossby wave which exists only west of about 105°W (3.4.2).[2]

2. The phase, longitude of onset and intensity of the TIWs proper (the Rossby wave component) are "chaotic", varying significantly from year to year of a repeat annual cycle GCM integration and being sensitive to relatively small perturbations such as the introduction of the Galápagos (4.1.1).

3. Although the seasonal wave activity in the equatorial East Pacific is dominated by a remotely forced Kelvin wave which arrives in the region during the northern spring, the activity continues at a lower level during the rest of the year. In OCCAM these waves are of the third baroclinic mode. (2.1.3, 3.5)

5.2 Significance of Results; Future Directions

One of the stated aims of the EPIC programme (page 1) is to determine why the cold tongue extends eastward beyond the longitude (about 110°W) where the wind on the equator becomes predominantly southerly, and to the South American coast. This thesis has given a two-part answer to this question. Firstly, a close look at the extant satellite SST data shows that the cold tongue does *not* typically reach as far east as the continent, but terminates abruptly at the Galápagos. Secondly, while the wind

[2]Not all of these observations are new to this study.

is indeed predominantly southerly in this region, it still has an eastward component which is capable of cooling the equatorial waters by means of upwelling. In the last thousand kilometres or so this effect is enhanced by hydraulically forced upwelling of EUC waters due to the presence of the islands themselves. It is hoped, anyway, that the present study may inform some of the observational work to be carried out under EPIC.

The climatological significance of this effect is more difficult to assess. An SST difference of a few degrees between the east and west of the islands is likely to induce an "inverse Walker" circulation on a local scale, and indeed (for instance) it is noticeably more cloudy to the east than it is to the west of the islands[3]. On regional and seasonal scales we found that the islands made a difference of at most a few tenths of a degree C. Whether such changes in the East Pacific are sufficient to have a significant meteorological impact is not obvious and remains to be determined, perhaps using a suitably forced atmospheric model in the manner of the original Palmer/Mansfield experiment. Alternatively, coupled model integrations with and without the Galápagos could be performed; this would also avoid the possibility noted earlier that the models used in the present study underestimate the islands' effect on SST because of being constrained by the climatological forcing. A wider range of forcing could also be applied to ocean-only models to assess the islands' effects under different conditions; analysis of the recent integration of OCCAM using 6-hourly winds would be a good starting point for this.

Observational effort could also be put into verifying some of the other findings of this study. Some of these phenomena have never been sought, *e.g.* the Rossby-gravity waves east of the Galápagos or the benthic signature of TIWs. Others, such as the determination by the islands of the eastern limit of the divided SEC, or the downstream behaviour of the EUC, have been observed only incompletely or haphazardly.

This thesis is the result of work done wholly while I was in registered postgraduate candidature.

[3]For example, in the AVHRR weekly SST data for 1990, a 97,500 km^2 region immediately to the west of the islands had an average of 36 out of a possible 52 SST measurements per pixel, whereas for a comparable region to the east the number was only 25.

Appendix A

Summary of CdP Theory

The following is a summary, with some clarification, of the theory presented by Cane & du Penhoat (1982) and referred to several times in the main part of the thesis.

The basic idea is to consider what happens after an initial set-up consisting of a Kelvin wave to the west, or a Rossby wave to the east, of a "thin" island occupying latitudes y such that $b < y < a$, in units of the appropriate Rossby radius. (As pointed out on page 4, one can be fairly relaxed about the "thinness" requirement.) The water on the other side of the island is initially stagnant. The waves in question are linear equatorial waves in the long-wave approximation, so that the zonal wavelength is effectively infinite[1] and the meridional velocity component is negligible even for the Rossby waves. Furthermore, only waves in the limit as the frequency tends to zero ($\sigma \to 0$) are considered. Therefore the problem is really an *adjustment* problem in which the initial condition has the eastern or western half-plane filled by zonally constant zonal currents with the meridional structure of the appropriate wave. This is not as great a restriction as it sounds, because of the completeness of the set of meridional structure functions—and in any case, the near-equatorial currents sometimes resemble individual waves, as noted in Section 3.4.

One nice property of this problem is that for times t large compared to an equatorial inertial period (of order 2 days), all that need to be considered are the incident,

[1] Thus the "wave" terminology is somewhat debatable, though it is standard and is used throughout this Appendix. However, it is better to think of the resulting expressions as determining the steady-state currents after the adjustment has finished, rather than wave amplitudes as such.

reflected and transmitted remnants of the initial wave, plus a short $\sigma \to 0$ Rossby and/or Yanai (Rossby-gravity) wave to the east of the island (*Anderson and Rowlands*, 1976; *Cane and Sarachik*, 1976). This reduces much of the calculation to simple matching of boundary conditions. The short wave gets shorter with time, like $J_0\left(2\sqrt{xt}\right)$ where J_0 is a Bessel function, thus resolving itself into a thin boundary current.

For the case of an incident Kelvin wave to the west of the island, the argument is as follows. Non-dimensionalising on the Rossby radius $\lambda = (gH/\beta^2)^{1/4} = (c/\beta)^{1/2}$ for horizontal lengths, the equivalent depth H of the vertical mode in question for vertical distances, the equatorial inertial time $(gH\beta^2)^{1/2} = (\beta c)^{-1/2}$ for times and the gravity wave speed c for velocities, the "unit" incident wave has $v = 0$, $u = h = \psi_0(y) = \pi^{-1/4}\exp(-y^2/2)$. The ψ_0 notation emphasises that the Gaussian is also the zeroth order Hermite function of Moore and Philander (1977) (see equation (A.41) below). [Thus, for example, the vertical displacement at the equator is dimensionally $\pi^{-1/4}H$ times the appropriate vertical structure function.] Under the long-wave approximation the reflected long Rossby wave also has $v = 0$, and both waves are in geostrophic balance

$$yu + \frac{\partial h}{\partial y} = 0. \tag{A.1}$$

Cane and du Penhoat (henceforth referred to as "CdP") consider the reflected Rossby wave not as a sum over meridional modes, but simply as having dynamical fields u^R, h^R to be determined by the boundary conditions. (This is another intelligent simplification.) Similarly the short Rossby wave east of the island is defined by

$$[u^s, v^s, h^s] = \left[-\frac{\partial}{\partial y}, \frac{\partial}{\partial x}, y\right] J_0\left(2\sqrt{xt}\right)\chi(y) \tag{A.2}$$

where χ is to be determined.

Introducing the island as a barrier from $y = a$ to $y = b$ at $x = 0$, the boundary conditions are

$$u = 0 \text{ at } x = 0_+ \text{ and } x = 0_-, \text{ for } b < y < a; \tag{A.3}$$

$$u, h \text{ continuous, for } y < b \text{ and } y > a. \tag{A.4}$$

Denoting solutions west and east of the island by superscript W and E respectively, and letting T be the amplitude transmission coefficient for the Kelvin wave,

$$u^W = u^R + \psi_0(y), \text{ and} \tag{A.5}$$

$$h^W = h^R + \psi_0(y). \tag{A.6}$$

Using (A.3), (A.4) and the fact that $J_0(0) = 1$,

$$u^E = T\psi_0(y) - \frac{\partial \chi}{\partial y} \text{ and} \tag{A.7}$$

$$h^E = T\psi_0(y) + y\chi \tag{A.8}$$

at $x = 0_+$ and for all y. Hence for $y < b$ and $y > a$ (*i.e.* beyond the latitudes covered by the island),

$$u^W = T\psi_0(y) - \frac{\partial \chi}{\partial y} \text{ and} \tag{A.9}$$

$$h^W = T\psi_0(y) + y\chi \tag{A.10}$$

at $x = 0_-$. Note that the solution at $x = 0_-$ applies for all $x < 0$, because of the "infinite" zonal wavelength of all the structures in this region. Since u^W and h^W satisfy the geostrophic relation (A.1) (because the Kelvin and reflected Rossby waves do so individually), we deduce from (A.9), (A.10) that

$$\chi = 0 \text{ for } y < b \text{ and } y > a, \tag{A.11}$$

i.e. that no short Rossby waves exist outside the latitude range of the island. Hence from (A.5), (A.6), (A.9) and (A.10),

$$u^R = h^R = (T-1)\psi_0(y) \text{ for } y < b \text{ and } y > a, \tag{A.12}$$

determining the reflected Rossby wave north and south of the island.

Next, from (A.1), (A.3) and (A.4),

$$h^W = \text{ const. } = D, \text{ say, for } x = 0_- \text{ and } b < y < a; \tag{A.13}$$

the water piles up against the west coast of the island, with a set-up D independent of latitude. Comparing (A.13) with (A.10) and (A.11), we observe that, at $x = 0_-$, h is equal to D just south of the northern tip of the island, but to $T\psi_0(a)$ just north

thereof, and similarly at the southern tip. Hence *there must be a discontinuity in* $h(y)$ *at at least one tip* (except possibly when $a = -b$, *i.e.* when the island is symmetric about the equator, since ψ_0 is even in y). None of this undermines the geostrophy (A.1), and so for this inviscid case there exists a contribution

$$u = A\delta(y-a) + B\delta(y-b) \tag{A.14}$$

to the flow field west of the island. *This is the origin of the jets in this theory.* In the viscous case the δ-functions are replaced by jets of small but finite thickness in which A and B represent the *transport* in the jets. CdP work through an example with Rayleigh friction.

Continuing with the analysis, we next have

$$\chi(y) = T\int_b^y \psi_0(\tilde{y})\,d\tilde{y} + C \text{ for } x = 0_+ \text{ and } b < y < a, \tag{A.15}$$

which follows from (A.3), (A.4), (A.7) and (A.8).

Putting it all together, the solution to the problem has the form:

For $y \geq a$ and $y \leq b$ (outside the latitude range of the island) and at $x = 0$:

$$u^W = u^E = T\psi_0(y) + A\delta(y-a) + B\delta(y-b), \tag{A.16}$$
$$h^W = h^E = T\psi_0(y). \tag{A.17}$$

For $b < y < a$ (east and west of the island):

$$u^W = 0,\ h^W = D \text{ for } x < 0, \tag{A.18}$$
$$u^E = 0,\ h^E = y\left[\int_b^y \psi_0(\tilde{y})\,d\tilde{y} + C\right] + T\psi_0(y), \text{ for } x = 0_+. \tag{A.19}$$

It remains to determine the five constants; we need five equations in the unknowns A, B, C, D, T. Integrating the geostrophic relation (A.1) over tiny intervals spanning the island tips,

$$aA + T\psi_0(a) - D = 0, \tag{A.20}$$
$$bB - T\psi_0(b) + D = 0. \tag{A.21}$$

Here we have used $h = DH(a-y) + T\psi_0(y)H(y-a)$ for the interval spanning the northern tip, and similarly at the southern tip, H being the unit step function.

Next, define an inner product of two waves by

$$\left[(u^a, h^a), (u^b, h^b)\right] \equiv \int_{-\infty}^{+\infty} (u^a u^b + h^a h^b)\, dy. \tag{A.22}$$

The Kelvin wave and the individual meridional-mode Rossby waves are all mutually orthogonal under this inner product (see *e.g.* Cane and Sarachik (1976)). Taking the inner product of ((A.5),(A.6)) with the unit Kelvin wave (ψ_0, ψ_0) then gives

$$\left[(\psi_0, \psi_0), (u^W, h^W)\right] = [(\psi_0, \psi_0), (\psi_0, \psi_0)] = 2, \text{ since } \int_{-\infty}^{+\infty} \psi_0^2\, dy = 1. \tag{A.23}$$

Using (A.16), (A.17) and (A.18) to perform the integral west of the island, this gives us our third equation

$$2T\left\{\int_a^\infty \psi_0^2\, dy + \int_{-b}^\infty \psi_0^2\, dy\right\} + A\psi_0(a) + B\psi_0(b) + D\int_b^a \psi_0\, dy = 2. \tag{A.24}$$

Physically, the role of the jets is to supply the mass flux for the portion of the transmitted Kelvin wave due east of the island. This they do by flowing into the east coast boundary current, from which the water is gradually drawn out into the transmitted wave. So the flux from the southern jet equals the short Rossby wave flux at the southern tip. (This result can also be proved more rigorously.) Since the latter flux is, using (A.2), (A.11) and (A.15),

$$\int_{0_+}^\infty v^s_{y=b}\, dx = C\int_{0_+}^\infty \frac{\partial}{\partial x}\left[J_0(2\sqrt{xt})\right]\, dx = C[J_0(\infty) - J_0(0)] = -C, \tag{A.25}$$

our fourth equation is simply

$$B = -C. \tag{A.26}$$

The same physical considerations give the final required equation

$$A + B = T\int_b^a \psi_0(y)\, dy. \tag{A.27}$$

[Again this can be obtained mathematically, by integrating the continuity equation over the little rectangle $[-\varepsilon, \varepsilon] \times [b - \varepsilon, a + \varepsilon]$ surrounding the island.]

Solving the five equations (A.20), (A.21), (A.24), (A.26) and (A.27), we finally obtain

$$T = 2(a-b)/E \text{ where} \tag{A.28}$$

$$E = -ab\left(\int_b^a \psi_0\,dy\right)^2 + 2(a-b)\left(1-\int_b^a \psi_0^2\,dy\right) + 2\left(a\psi_0(b) - b\psi_0(a)\right)\int_b^a \psi_0\,dy + \left(\psi_0(a)-\psi_0(b)\right)^2, \tag{A.29}$$

$$A = \frac{-T\left\{\psi_0(a)-\psi_0(b)+b\int_b^a \psi_0\,dy\right\}}{a-b}, \tag{A.30}$$

$$B = \frac{T\left\{\psi_0(a)-\psi_0(b)+a\int_b^a \psi_0\,dy\right\}}{a-b}, \tag{A.31}$$

$$C = -B, \text{ and} \tag{A.32}$$

$$D = aA + T\psi_0(a). \tag{A.33}$$

The argument for an m-th meridional mode Rossby wave

$$(\hat{u},\hat{h}) = \left(\frac{\psi_{m+1}}{2\sqrt{2(m+1)}} - \frac{\psi_{m-1}}{2\sqrt{2m}},\ \frac{\psi_{m+1}}{2\sqrt{2(m+1)}} + \frac{\psi_{m-1}}{2\sqrt{2m}}\right) \tag{A.34}$$

incident on the eastern side of the island goes through *mutatis mutandis* to give

$$T_R = \frac{TF}{2(a-b)}, \text{ where} \tag{A.35}$$

$$F = (a-b)\int_b^a (\hat{u}+\hat{h})\psi_0\,dy + \left(b\psi_0(a) - a\psi_0(b)\right)\int_b^a \hat{u}\,dy + \left(b\hat{h}(a) - a\hat{h}(b)\right)\int_b^a \psi_0\,dy + \left(\psi_0(a)-\psi_0(b)\right)\left(\hat{h}(a)-\hat{h}(b)\right) + ab\int_b^a \hat{u}\,dy\int_b^a \psi_0\,dy; \tag{A.36}$$

$$A = -\frac{T_R\left\{\psi_0(a)-\psi_0(b)+b\int_b^a \psi_0\,dy\right\} + \hat{h}(a) - \hat{h}(b) + b\int_b^a \hat{u}\,dy}{a-b}, \tag{A.37}$$

$$B = \frac{T_R\left\{\psi_0(a)-\psi_0(b)+a\int_b^a \psi_0\,dy\right\} + \hat{h}(a) - \hat{h}(b) + a\int_b^a \hat{u}\,dy}{a-b}, \tag{A.38}$$

$$C = -B, \text{ and} \tag{A.39}$$

$$D = aA + \hat{h}(a) + T_R\psi_0(a). \tag{A.40}$$

Here T is as in equation (A.28), T_R is the amplitude of the reflected Kelvin wave, and

$$\psi_m = \frac{\exp(-y^2/2)H_m(y)}{\sqrt{2^m m!\sqrt{\pi}}} \tag{A.41}$$

is the m-th "Hermite function" of Moore and Philander (1977), H_m being the m-th Hermite polynomial. A, B, C and D all have the same meaning as for the other case.

Although CdP do not mention this, the integrals involved can be evaluated using

standard functions (*i.e.* without recourse to quadrature as such). I have determined the following analytical expressions for the required integrals:

$$\int_b^a \psi_0^2\, dy = \frac{1}{2}\left[\mathrm{erf}(a) - \mathrm{erf}(b)\right], \tag{A.42}$$

$$\int_b^a \psi_0\, dy = \frac{\pi^{1/4}}{\sqrt{2}}\left[\mathrm{erf}(a/\sqrt{2}) - \mathrm{erf}(b/\sqrt{2})\right], \tag{A.43}$$

$$\int_b^a (\hat{u}+\hat{h})\psi_0\, dy = \frac{\sum_{k=0}^{m+1} a_k \Gamma\left(\frac{k+1}{2}\right)\left[S_k^a P\left(a^2, \frac{k+1}{2}\right) - S_k^b P\left(b^2, \frac{k+1}{2}\right)\right]}{(m+1)\sqrt{2^{m+4} m! \pi}}, \tag{A.44}$$

$$\int_b^a \hat{u}\, dy = \frac{\sum_{k=0}^{m+1} 2^{k/2} a_k \Gamma\left(\frac{k+1}{2}\right)\left[S_k^a P\left(\frac{a^2}{2}, \frac{k+1}{2}\right) - S_k^b P\left(\frac{b^2}{2}, \frac{k+1}{2}\right)\right]}{(m+1)\sqrt{2^{m+5} m! \sqrt{\pi}}} - \frac{\sum_{k=0}^{m-1} 2^{k/2} a_k \Gamma\left(\frac{k+1}{2}\right)\left[S_k^a P\left(\frac{a^2}{2}, \frac{k+1}{2}\right) - S_k^b P\left(\frac{b^2}{2}, \frac{k+1}{2}\right)\right]}{\sqrt{2^{m+3} m! \sqrt{\pi}}} \tag{A.45}$$

where a_k is the coefficient of y^k in the appropriate Hermite polynomial $H_{m\pm1}(y)$,

$$S_k^x = \begin{cases} 1 & \text{if } k \text{ is odd} \\ \mathrm{sgn}(x) & \text{if } k \text{ is even,} \end{cases} \tag{A.46}$$

and P is the incomplete gamma function defined by

$$P(x,c) = \frac{1}{\Gamma(c)} \int_0^x y^{c-1} e^{-y}\, dy. \tag{A.47}$$

Most of the required functions are available in standard mathematics packages. For instance, Matlab routines are available for everything except the Hermite polynomials $H_m(y)$ and their coefficients a_k. The latter I calculate *via* their representation as linear combinations of hypergeometric functions (see *e.g.* Mathews and Walker (1973)), whence for m odd we have

$$\begin{aligned} a_k &= 0 && k \text{ even} \\ a_1 &= \frac{2^m \Gamma(-1/2)}{\Gamma(-m/2)} \\ a_k &= \frac{2(k-m-2)}{k(k-1)} a_{k-2} && k \text{ odd and } 1 < k \leq m; \end{aligned} \tag{A.48}$$

and for m even (including $m = 0$),

$$\begin{aligned} a_k &= 0 && k \text{ odd} \\ a_0 &= \frac{2^m \Gamma(1/2)}{\Gamma((1-m)/2)} && \\ a_k &= \frac{2(k-m-2)}{k(k-1)} a_{k-2} && k \text{ even and } 0 < k \leq m. \end{aligned} \tag{A.49}$$

Actual values of the Hermite polynomials are easily calculated from the standard recursion relation

$$\begin{aligned} H_0(y) &= 1, \\ H_1(y) &= 2y, \\ H_m(y) &= 2\left(yH_{m-1}(y) - (m-1)H_{m-2}(y)\right), \ m > 1. \end{aligned} \tag{A.50}$$

(See *e.g.* Philander (1990), p.156.)

In conclusion, the two main points to take away from this Appendix are:

1. According to this theory, island-tip jets are a characteristic feature of flows past equatorial islands on timescales of more than a few days. The jets originate at the north and south tips of an island and extend zonally towards the west, though the direction of the flow can be either towards or away from the island.

2. The transport in each jet can be calculated from A and B of equations (A.30), (A.31) and/or (A.37), (A.38). In principle the ambient flow near the island should be constructed as a superposition of "long" planetary waves, and the transports calculated as the sum of the corresponding A's and B's. In practice, however, it seems that one wave is usually enough, for two reasons. Firstly, actual and modelled flows often approximate individual such waves. Secondly, the simplifications in the assumptions on which the theory is based should make us wary of using the formulæ for much more than order-of-magnitude estimates of the strength of the jets; adequate estimates can probably be made using single waves.

Appendix B

Application of the CdP Formulæ

In this Appendix is described the application of equations (A.30), (A.31), (A.37) and (A.38) to particular transects of zonal velocity. The example of an incident first meridional mode Rossby wave, referred to in Chapter 3, is used as an illustration.

The first step is to be clear about the meaning of the symbols involved, in dimensional terms. As in Appendix A, we define λ to be the Rossby radius in metres and c the corresponding gravity wave speed (usually an internal wave speed) in $\mathrm{m\,s^{-1}}$. Then the dimensional velocities are c times the non-dimensional velocities considered in Appendix A; for instance, if $\hat{u}_1$ is the meridional structure function of our Rossby wave (*i.e.* $\hat{u}$ of equation (A.34) with m=1), the "unit" wave depicted in Figure 3.19 represents a flow with westward velocity $c\hat{u}_1(0)$ at the equator. For our example c was about 2.5 $\mathrm{m\,s^{-1}}$, and $\hat{u}_1(0)$ is about -0.4, giving an equatorial velocity of about 1 $\mathrm{m\,s^{-1}}$ to the west. The vertically averaged current transect from OCCAM in Figure 3.19 has a peak westward velocity of about 0.31 $\mathrm{m\,s^{-1}}$ and may therefore be described as a Rossby wave of amplitude about 0.31; the transports in the jets predicted from the theory will be 0.31 times those for the dimensional version of the "unit" wave.

To see the dimensionalisation appropriate for the transports A and B in the jets, consider that equation (A.16) has the form

$$u = \cdots + A\delta(y-a) + \cdots. \tag{B.1}$$

Since the δ function is defined by

$$\int f(y)\delta(y-a)\,dy = f(a)$$

(for any range of integration including a), its dimension is formally the reciprocal of that of the variable of integration; so in our example the dimensional δ function has dimension $(\lambda\ \mathrm{m})^{-1}$. Since the dimension of u is $c\ \mathrm{m\,s^{-1}}$, it follows from equation (B.1) that the dimensional transport in the northern jet is $\lambda cA\ \mathrm{m^2\,s^{-1}}$ for our unit Rossby wave. The transport in the southern jet is similarly $\lambda cB\ \mathrm{m^2\,s^{-1}}$. Transports in Sverdrups can be obtained by multiplying by the appropriate depth d in metres (and dividing by 10^6). For our example λ was 3.29×10^5 m, and d is 41m (the sum of the depths of the top two model layers, within which the SEC and the jets were confined), so that one "CdP jet unit" is about 33.7 Sv. The consistency of these dimensionalisations can be (and in this case has been) checked *via* the fact that the transport in the two jets has to add up to the Rossby wave transport that is blocked by the island plus the transport in the reflected Kelvin wave; in symbols,

$$\lambda c(A+B) = c\int_b^a \hat{u} + T_R\psi_0\,dy.$$

As represented in OCCAM, the Galápagos reach from the equator to 1.25°S, whence a=0 and b=−0.4229 (in units of λ). For these values the formulæ of Appendix A give A=−0.0813 and B=−0.0757, implying transports of 2.7 and 2.5 Sv respectively given our choice of λ, for the unit wave. The amplitude T_R of the reflected Kelvin wave is 8.6×10^{-4}, whence the transport in this wave in the latitude range of the islands is 0.009 Sv. Comparing this with the 5.256 Sv in the Rossby wave provides a *post hoc* justification for ignoring the Kelvin wave in our representation of the OCCAM flow pattern by a single mode.

Multiplying our OCCAM incident wave amplitude of 0.31 by the jet transports calculated for the unit wave gives us the predicted transports of 0.85 and 0.79 Sv quoted in Chapter 3.

Appendix C

Description of RG Model

The numerical model used in the present study has been adapted from a version of the model used in recent work by McCreary and co-workers (*McCreary and Yu*, 1992; *Lu et al.*, 1998), and which has a genealogy dating back at least to Cane (1979). Like all numerical models, it is at two removes from reality. First there is the continuous mathematical model of the real ocean, with suitably simplified dynamics and/or thermodynamics, and then there is the discretized version of the mathematical model which can be implemented (to within rounding error) on a computer. I shall describe each of these in turn.

C.1 Mathematical model

C.1.1 The concept of an RG model

The distinguishing feature of a "reduced gravity" (RG) model is that the vertical structure of the ocean is approximated as a number n of "active" layers of finite thickness overlying a "passive" layer in which the water is assumed to be at rest. The model is then referred to as an "n-and-a-half ($n\frac{1}{2}$) layer model". The fastest wave motions allowed are those corresponding to the first baroclinic mode of the real ocean, which are much slower than those of the barotropic mode, which is effectively filtered out. This greatly increases the maximum timestep permitted by the CFL condition, which is the principal reason for using this type of model in numerical studies. Most

of the integrations carried out during the present study used $n = 2$, with the top, middle and passive layers being referred to as layer 1, 2 and 3 respectively. A $3\frac{1}{2}$-layer version is also available, but none of the results from this are reported here, and this Appendix will concentrate on the $2\frac{1}{2}$-layer version.

The top layer can be considered to be confined under a rigid lid at $z = 0$, though this is not essential. All the layers are assumed to be well-mixed, *i.e.* in a vertical profile the horizontal velocity $\mathbf{u} = (u, v)$, temperature T and density ρ are constant within each layer and change abruptly at the interfaces between layers. It is not assumed that the mass of water above a point in the passive layer (or the equivalent quantity for the rigid lid model) is the same as that above neighbouring points—the active layer thicknesses can vary in space and time—so that horizontal pressure gradients can exist in this layer. This can only be reconciled with the layer being stationary by formally assuming that the layer is of infinite thickness and therefore mass.

That, at least, is how the concept of an RG model is usually presented. However, it is usually also stated that the horizontal pressure gradient vanishes in the passive layer, *e.g.* "the lower layer is assumed to be so deep that its horizontal pressure forces and velocities vanish" (*Cane*, 1979, page 234). As will be seen below, it is indeed essential to assume that the pressure gradient does vanish at some depth, when setting up the equations of motion for the model. Perhaps the best way to avoid the inconsistency is to retain the "infinite thickness" assumption, but to allow $\mathbf{u}$ to vary with depth in the passive layer. The passive layer can then be thought of as an infinitely deep homogeneous layer with motion forced by an imposed pressure distribution at its upper surface. As with surface gravity waves (see *e.g.* LeBlond and Mysak (1978)), the velocity and the pressure gradient will be non-zero just below the interface, but will tend to zero as $z \to -\infty$. In any case, the fluid in an RG model is further assumed to be hydrostatic (so that the model applies only to phenomena on sufficiently large spatial and temporal scales), and this leads to the passive layer pressure gradients being everywhere zero—again this is seen below. That is, the hypothetical $\mathbf{u}$ and ∇p near the top of the passive layer, while non-zero, are "small" in the relevant sense, and therefore negligible.

Reduced gravity models usually take the temperature and density to be constant within each layer, in the horizontal as well as the vertical. The model used here is unusual in that in the active layers the temperature is allowed to vary with x and y. Density is taken to be the linear function

$$\rho = \rho_0[1 - \alpha(T - T_0)] \tag{C.1}$$

of T, where α is the coefficient of thermal expansion and the subscript 0 refers to values in the passive layer, where the temperature does *not* vary with x or y. So the density also varies in the horizontal. α is assumed to have the constant value $2.5 \times 10^{-4}\,\mathrm{K}^{-1}$, which is the value it takes at a salinity of 35 psu and a temperature of about 19°C at atmospheric pressure. (In reality α depends quite strongly on T, varying from $0.5 \times 10^{-4}\,\mathrm{K}^{-1}$ at 0°C to $3.3 \times 10^{-4}\,\mathrm{K}^{-1}$ at 30°C—*i.e.* by a factor of more than 6 over the range of temperatures found in the real ocean.) Salinity is not carried as a variable in this model.

C.1.2 Equations of motion

We proceed to derive the various terms in the equations of motion for the model, integrated vertically across each active layer.

Pressure at depth z can be found by integrating the hydrostatic relation upwards from some deep level $z = -D$ (in the passive layer) where the horizontal pressure gradient can be taken to vanish, as discussed above. For the case $n = 2$ (Figure C.1) this gives

$$p = \begin{cases} p_0 - \rho_0 g D - \rho_1 g z + g(\rho_0 - \rho_1)h_1 + g(\rho_0 - \rho_2)h_2, & -h_1 < z \leq 0 \\ p_0 - \rho_0 g D - \rho_2 g z + g(\rho_0 - \rho_2)(h_1 + h_2), & -(h_1 + h_2) < z \leq -h_1 \\ p_0 - \rho_0 g(z + D), & z \leq -(h_1 + h_2), \end{cases} \tag{C.2}$$

where p_0 is the pressure at $z = -D$. Since everything apart from p_0, ρ_0, g, D and z is a function of x and y, the horizontal pressure gradients in the active layers are respectively

$$\nabla p_1 = g\alpha\nabla[(T_1 - T_0)h_1 + (T_2 - T_0)h_2] + g\alpha z \nabla T_1 \tag{C.3}$$

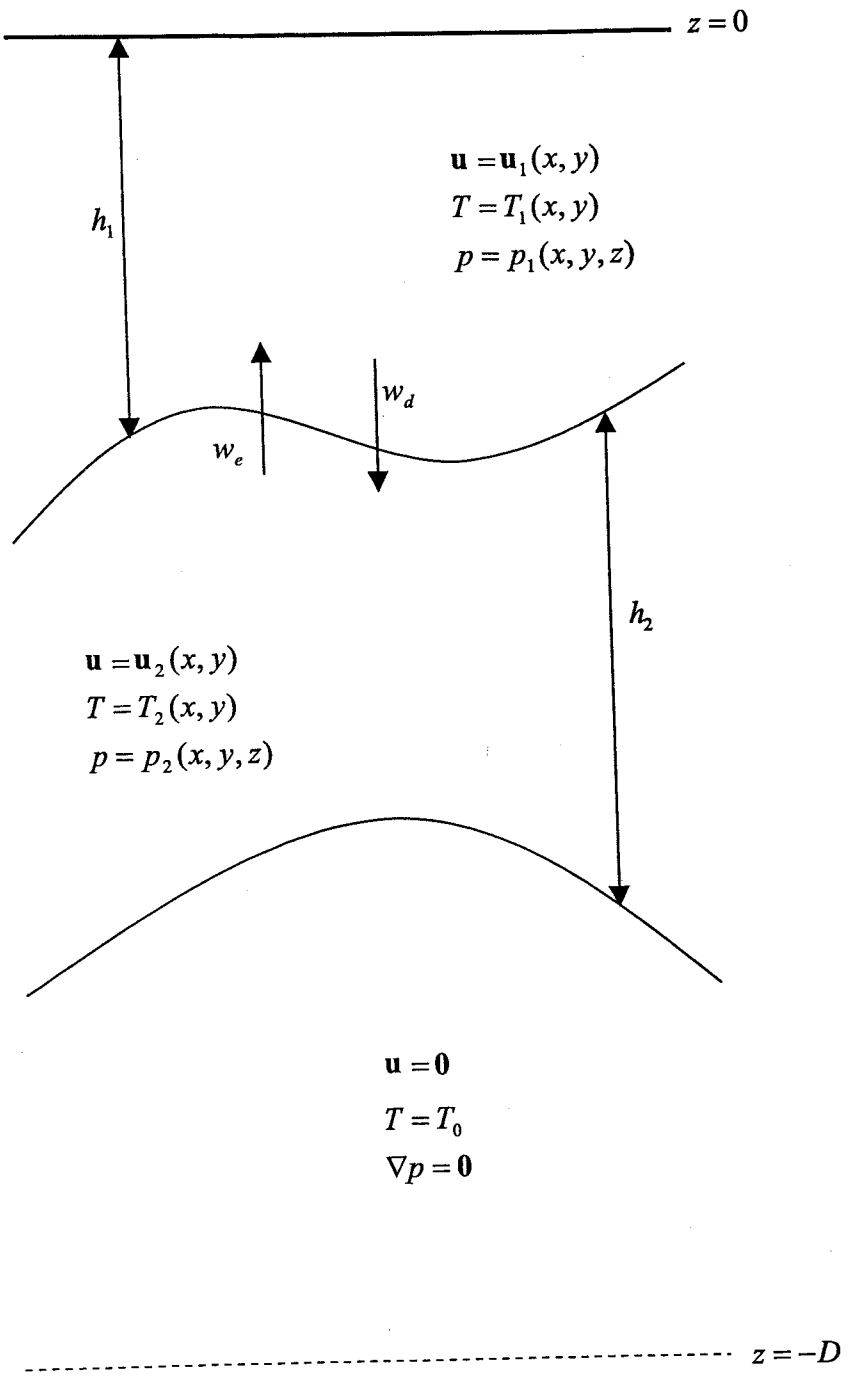

Figure C.1: Vertical structure of $2\frac{1}{2}$-layer model.

in the top layer, and

$$\nabla p_2 = g\alpha\nabla[(T_2 - T_0)(h_1 + h_2)] + g\alpha z\nabla T_2 \tag{C.4}$$

in the lower layer. Here (C.1) has been used to express the densities in terms of the temperatures, and the constant density ρ_0 has been absorbed into the definition of p. *I.e.* the p referred to from now on is the p of (C.2) divided by ρ_0.

The vertically integrated pressure gradient forces are thus $h_1 \langle\nabla p_1\rangle^z$ and $h_2 \langle\nabla p_2\rangle^z$, where the vertically *averaged* forces are

$$\langle\nabla p_1\rangle^z = \frac{1}{h_1}\int_{-h_1}^{0} p_1\, dz = g\alpha\nabla[h_1(T_1 - T_0) + h_2(T_2 - T_0)] - \frac{1}{2}g\alpha h_1\nabla T_1, \tag{C.5}$$

$$\langle\nabla p_2\rangle^z = \frac{1}{h_2}\int_{-(h_1+h_2)}^{-h_1} p_2\, dz = g\alpha\nabla[(h_1 + h_2)(T_2 - T_0)] - g\alpha(h_1 + \frac{1}{2}h_2)\nabla T_2. \tag{C.6}$$

Note that the presence of the $T_i - T_0$ terms is equivalent to using $g(\rho_0 - \rho_i)/\rho_0$ instead of the much larger value g for the gravitational acceleration, which is where the "reduced gravity" terminology comes from.

The non-linear terms can be derived as a special case of the general vertical coordinate formulation of Kasahara (1974), as in Schopf and Cane (1983), but a much simpler derivation is possible. Consider an elemental volume of horizontal extent Δx by Δy, and height $h(x, y)$. The flux of, for instance, v-momentum through one of the north-south walls of the elemental volume is

$$\begin{aligned} & \text{mass} \times \text{velocity flux} \\ = \ & \rho \times \text{volume flux} \times \text{velocity} \\ = \ & \rho \times uh\Delta y \times v, \end{aligned}$$

so that on making a Boussinesq-type approximation (*i.e.* ignoring variations in ρ), the net u-advection of v-momentum into the elemental volume is

$$-\rho\Delta x\Delta y\frac{\partial}{\partial x}(uhv).$$

Dividing by the mass $\rho h\Delta x\Delta y$ and then integrating vertically across the layer (multiplying by h) gives

$$-\frac{\partial}{\partial x}(uhv)$$

as the (vertically integrated) net flux per unit mass, which is what occurs in standard forms of the equations of motion. Using the standard tensorial notation

$$\nabla\cdot(\mathbf{ab}) = \frac{\partial}{\partial x_i}(a_i b_j) = b_j \nabla\cdot\mathbf{a} + a_i \frac{\partial b_j}{\partial x_i} = \mathbf{b}\nabla\cdot\mathbf{a} + (\mathbf{a}\cdot\nabla)\mathbf{b}, \tag{C.7}$$

this and the other three similar terms can be written compactly as

$$\nabla\cdot(\mathbf{u}h\mathbf{u}) \tag{C.8}$$

(for the fluxes *out of* the elemental volume). By comparison with (C.7), this can be written

$$h\mathbf{u}\nabla\cdot\mathbf{u} + (\mathbf{u}\cdot\nabla)(h\mathbf{u}),$$

which with the incompressibility assumption $\nabla\cdot\mathbf{u} = 0$ makes (C.8) look more like standard non-flux forms of the non-linear terms.

Because $\mathbf{u}$ is not a function of z, the rate of change of the vertically integrated velocity (volume flux into the elemental volume) for the top layer is

$$\frac{\partial}{\partial t}\int_{-h_1}^{0} \mathbf{u}_1\, dz = \frac{\partial}{\partial t}(h_1\mathbf{u}_1),$$

and the vertically integrated Coriolis term is

$$f\mathbf{k}\times h_1\mathbf{u}_1,$$

where $f = \beta y$, *i.e.* the equatorial β-plane is used. The terms in the layer 2 equation are the same (with suffix 2).

In the absence of horizontal and vertical mixing (whose parametrizations are given in the next subsection), the volume of our fluid element increases at a rate equal to the convergence of the volume flux, whence the continuity equation (under incompressible and Boussinesq conditions) is

$$\frac{\partial h_i}{\partial t} + \nabla\cdot(h_i\mathbf{u}_i) = \text{ mixing terms}, \tag{C.9}$$

for $i = 1, 2$. Because the temperature does not vary with z, the thermodynamic equation is the same whether vertically integrated or not, and is

$$\frac{\partial T_i}{\partial t} + \mathbf{u}_i\cdot\nabla T_i = \text{ adiabatic terms}. \tag{C.10}$$

C.1.3 Parametrizations

The wind stress τ used to drive the model dynamically is all put into the top layer. A heat flux into the surface layer is prescribed by relaxation towards some climatological value, after Haney (1972). Specifically, the rate of change of the top layer temperature is Q_1/h_1, where

$$Q_1 = \frac{H_q}{t_q}(T_1^* - T_1),$$

H_q being a Haney coefficient (set to 100 m in this model) and t_q a relaxation time (100 days). T_1^* is the climatological temperature. For very long integrations of the closed basin version of this model, which was used here, a similar formulation can be used to prevent the lower layer temperatures from drifting too far from unrealistic values (the relaxation then representing the effects of large scale thermohaline circulations). However, this was not felt to be necessary for the integrations of a few years at most which were carried out for the present study.

Horizontal mixing is represented by a Laplacian with kinematic viscosity ν, though a biharmonic ("scale-dependent") form is also available. Horizontal diffusion is also given a Laplacian representation, with coefficient κ. Vertical mixing is basically parametrized by an entrainment velocity w_e^0 and a detrainment velocity w_d specifying exchange of water between the two active layers (there is no exchange with the passive layer). These velocities are defined simply to cause the top and bottom active layer thicknesses to relax towards pre-specified minimum values when they fall below these values, with the deficit being made up by water from the other active layer. That is

$$w_e^0 = \frac{(h_1^{\min} - h_1)^2}{h_1^{\min} t_e}\theta(h_1^{\min} - h_1), \text{ and} \tag{C.11}$$

$$w_d = -\frac{(h_2^{\min} - h_2)^2}{h_2^{\min} t_d}\theta(h_2^{\min} - h_2), \tag{C.12}$$

where t_e and t_d are timescales for the entrainment and detrainment, and θ is the step function defined by

$$\theta(x) = \begin{cases} 1 & \text{if } x > 0 \\ 0 & \text{otherwise.} \end{cases}$$

(The minus sign in the expression for w_d is due to the fact that the mixing velocities both define fluxes *into* layer 1.) Lu *et al.* (1998) remark that as currents in a layer (and

therefore the shear between neighbouring layers) are large when the layer is thin, this amounts to a simple parametrization of Richardson number-dependent mixing. For the top layer there is also the consideration that when layer 1 is thin, the energy from the wind will mix down through the layer, causing mixing at its base and deepening the layer; that is, equation (C.11) also contains aspects of a Kraus-Turner mixed layer parametrization (*Kraus and Turner*, 1967), in a very crude form.

A problem I encountered wherein layer 1 thicknesses were going negative at certain isolated points on the boundary of the model was solved in the same spirit. I determined that the advection terms in the continuity equation were responsible, and chose enhanced vertical mixing close to lateral boundaries as the unrepresented physical phenomenon to balance the excessive divergence. Whenever a boundary value of h_1 fell below a critical value defined as the minimum of $h_1^{\min}$ and a certain fraction (9/10) of the value of h_1 one gridpoint further in from the boundary, the entrainment velocity was increased just enough to return the boundary value to the critical value at the end of the timestep. This was not found to be necessary near the islands discussed later.

A background level of diffusive mixing across the interface between the active layers is represented as a contribution w_m to the entrainment velocity based on a steady state advective-diffusive balance, $(\kappa_m T_z)_z = w_m T_z$ (*Lu et al.*, 1998), where the finite-difference representation of w_m is given in the next subsection. We write $w_e = w_e^0 + w_m$ as our final entrainment velocity.

The rate of transfer of momentum from layer 1 to layer 2 is then $w_d \mathbf{u}_1$, and the rate of transfer from layer 2 to layer 1 likewise $w_e \mathbf{u}_2$. Similarly the volume fluxes (per unit area) are simply w_d and w_e respectively.

Putting it all together, the equations of motion for the top layer of the model are

$$\frac{\partial h_1 \mathbf{u}_1}{\partial t} + \nabla\cdot(\mathbf{u}_1 h_1 \mathbf{u}_1) + f\mathbf{k}\times h_1\mathbf{u}_1 + h_1 \langle \nabla p_1 \rangle^z = \boldsymbol{\tau} + w_e\mathbf{u}_2 + w_d\mathbf{u}_1 - \nu\nabla^2(h_1\mathbf{u}_1), \quad \text{(C.13)}$$

$$\frac{\partial h_1}{\partial t} + \nabla\cdot(h_1\mathbf{u}_1) = w_e + w_d - \kappa\nabla^2 h_1, \text{ and} \quad \text{(C.14)}$$

$$\frac{\partial T_1}{\partial t} + \mathbf{u}_1\cdot\nabla T_1 = \frac{Q_1}{h_1} - \frac{w_e(T_1 - T_2)}{h_1} - \kappa\nabla^2 T_1; \quad \text{(C.15)}$$

and those for the other active layer are

$$\frac{\partial h_2\mathbf{u}_2}{\partial t} + \nabla\cdot(\mathbf{u}_2 h_2\mathbf{u}_2) + f\mathbf{k}\times h_2\mathbf{u}_2 + h_2\langle\nabla p_2\rangle^z = -w_e\mathbf{u}_2 - w_d\mathbf{u}_1 - \nu\nabla^2(h_2\mathbf{u}_2), \quad \text{(C.16)}$$

$$\frac{\partial h_2}{\partial t} + \nabla\cdot(h_2\mathbf{u}_2) = -w_e - w_d - \kappa\nabla^2 h_2, \text{ and} \quad \text{(C.17)}$$

$$\frac{\partial T_2}{\partial t} + \mathbf{u}_2\cdot\nabla T_2 = -\frac{w_d(T_1 - T_2)}{h_2} - \kappa\nabla^2 T_2. \quad \text{(C.18)}$$

The model also has a simple convection scheme. Whenever the difference $\Delta T_1 = T_1 - T_2$ between the two active layer temperatures falls below a specified value (0.03°C was used here), the temperatures are reset so that the new difference takes that value. The adjustment is made in such a way as to preserve the depth-weighted average temperature and therefore the mass of the water column. In the supplied model the value used was zero, so that adjustment took place only when the column became gravitationally unstable; a non-zero value was used in the present study because the actual ΔT_1, rather than an arbitrarily specified value, was used in the parametrization of vertical diffusion described below. A zero value of ΔT_1 would have produced infinite entrainment or detrainment velocities. Other parametrizations to do with the representation of large-scale thermohaline processes were disabled for this study, for the reason given earlier regarding the heat flux into the lower layer.

C.2 Numerical implementation

The model is integrated on the Arakawa C grid (*Mesinger and Arakawa*, 1976), as defined in detail in Figure C.2. As in equations (C.13) to (C.18), the prognostic variables are T, h and the products hu, hv, in each active layer. T and h are defined at the centre of each grid box, and hu, hv at the centre of the eastern and northern edge respectively—u and v, when required, are derived as hu or hv divided by the average of h at the two neighbouring points in the east-west and north-south directions respectively. This grid arrangement is optimal in reducing phase speed errors in oceanic waves, provided that the grid spacing is less than the appropriate Rossby radius (*Mesinger and Arakawa*, 1976), which it was in this case[1].

[1] Typical Rossby radii in the middle of an integration were about 330 km for the first and 240 km for the second vertical mode, compared to a grid spacing which was usually 0.5° or about 55 km.

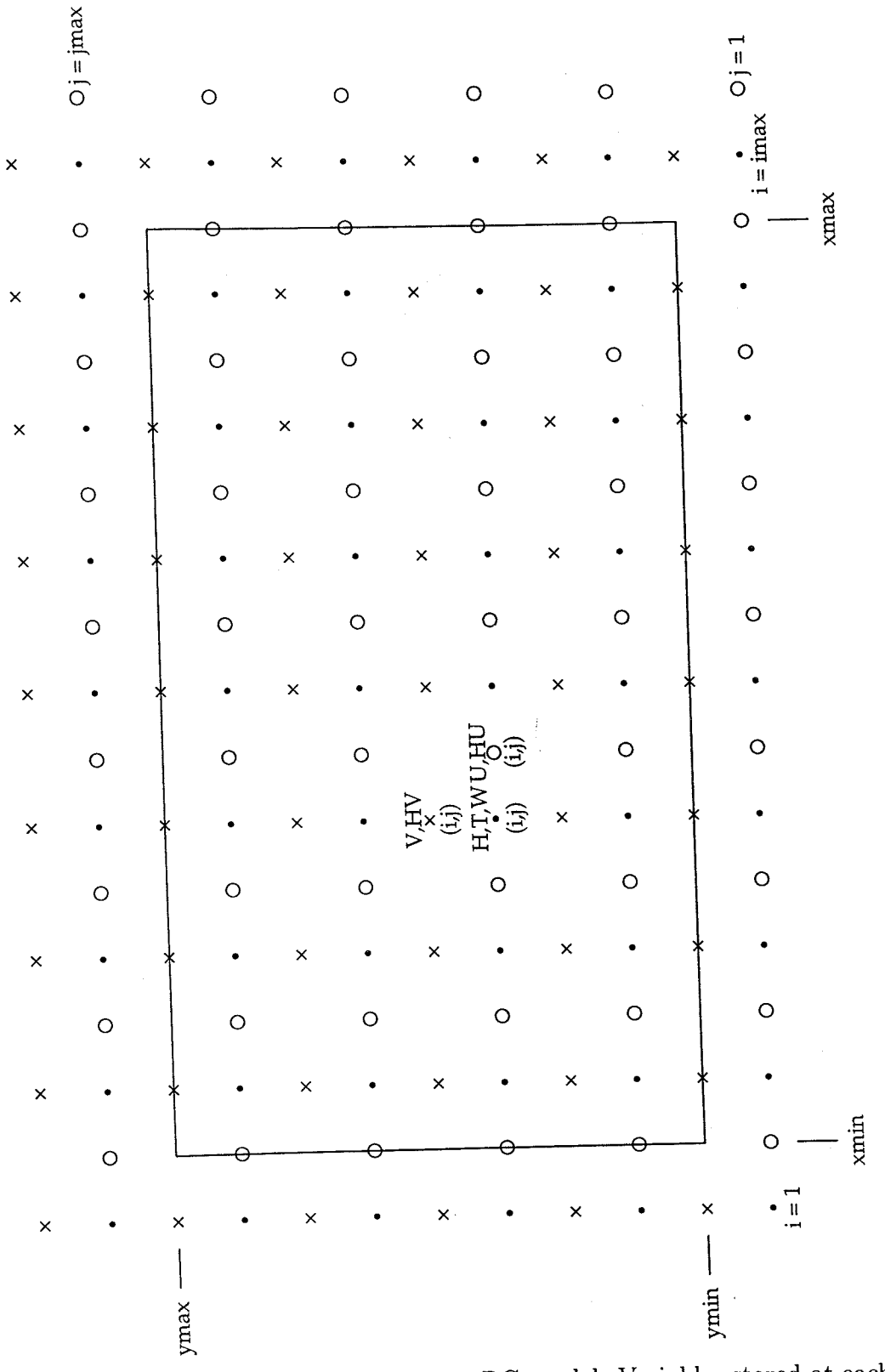

Figure C.2: Arakawa C grid as used in RG model. Variables stored at each point are indicated. The solid line represents the physical boundary of the model.

Spatial derivatives are approximated by simple centred differences (no sophisticated advection schemes such as flux-corrected transport are used, for instance). Grid spacings Δx, Δy are always used, and never twice this, so that, for example, the $\partial(uhu)/\partial x$ term in the u-momentum equation is represented by

$$\frac{u^+hu^+ - u^-hu^-}{\Delta x},$$

where for instance $u^+ = (u_{i+1,j}+u_{i,j})/2$, the interpolated value for u at the T point to the east of u point (i,j) at which the gradient is required (refer to Figure C.2 again). Second derivatives are calculated as, *e.g.*,

$$\left(\frac{\partial^2 h}{\partial x^2}\right)_{i,j} \approx \frac{h_{i+1,j} - 2h_{i,j} + h_{i-1,j}}{(\Delta x)^2}.$$

The diffusive contribution w_m to the vertical mixing introduced at page 143 is approximated by means of defining nominal temperatures at the surface and at the layer interfaces. Let $T_{0.5}$, $T_{1.5}$ and $T_{2.5}$ denote the temperatures at the surface, the interface between the two active layers, and the interface between the lower active layer and the passive layer, respectively. Then the derivatives in

$$w_m = \frac{\kappa_m T_{zz}}{T_z},$$

which are required at the layer 1–2 interface, may be approximated as follows. T_z is the gradient of T across the interface, approximately $\Delta T_1/\frac{1}{2}(h_1+h_2)$ where $\Delta T_1 = T_1 - T_2$, and T_{zz} is the similar gradient based on our assumed differences of T across each layer, *i.e.*

$$T_{zz} \approx \frac{\frac{T_{0.5}-T_{1.5}}{h_1} - \frac{T_{1.5}-T_{2.5}}{h_2}}{\frac{1}{2}(h_1+h_2)}.$$

Hence, in an obvious notation, we calculate w_m as

$$\frac{\kappa_m}{\Delta T_1}\left(\frac{\Delta T_{1.5}}{h_1} - \frac{\Delta T_{2.5}}{h_2}\right).$$

In lieu of anything better, the model in fact simply specifies $\Delta T_{1.5}$ and $\Delta T_{2.5}$ as 5 and 10°C respectively. ΔT_1 is calculated from the actual layer temperatures (although in the version of the model I obtained from Professor McCreary this too was a specified constant). Note that w_m is positive (entrainment) if $h_1/h_2 < \Delta T_{1.5}/\Delta T_{2.5}$, *i.e.* if the top layer becomes too thin compared to the lower layer, and negative (detrainment) if the sign of this inequality is reversed.

As indicated in Figure C.2, the model uses a rectangular closed boundary the north-south and east-west segments of which pass through u and v points respectively. In each layer, no-slip and no-flux boundary conditions

$$\mathbf{u} = \nabla^2(h\mathbf{u}) = T_n = (\nabla^2 T)_n = h_n = (\nabla^2 h)_n = 0,$$

where subscript n denotes a partial derivative normal to the boundary, are imposed. Values at the ghostly gridpoints outside the model domain are used where necessary, so that for example the condition of no diffusive flux of v momentum at the eastern boundary is implemented by storing $\nabla^2(hv)$ as an array, and setting the values of this variable in column IMAX to the negative of the calculated values in column IMAX−1.

A single island or land mass was introduced into the model as a rectangular block of solid earth points. On the north-south and east-west coasts of the island the boundary conditions were as above. At the corners of the island the boundary conditions were implemented as in a supplied version of the model which had sloping boundaries to represent Australia and North America. That is, h, T and the Laplacians thereof in corner grid boxes were set equal to an average of their values at the two neighbouring interior points, weighted by the reciprocal distances to these points.

A leapfrog method is used for the time stepping in the model, *i.e.* an equation

$$\frac{\partial g}{\partial t} = f$$

is integrated as

$$g^{(n+1)} = g^{(n-1)} + 2\Delta t f^{(n)},$$

where Δt is the time step and superscript (n) refers to time level $n\Delta t$.[2] High-frequency noise (time-splitting instability) is eliminated by averaging fields over two neighbouring time levels every 41 timesteps.

[2]The various mixing terms are in fact evaluated at the backward $(n-1)$ time level "to ensure numerical stability" (*McCreary and Yu*, 1992).

References

Allen, M. R., et al., Control of tropical instability waves in the Pacific, *Geophysical Research Letters*, *22*, 2581–2584, 1995.

Anderson, D. L. T., and P. B. Rowlands, The role of inertia-gravity and planetary waves in the response of a tropical ocean to the incidence of an equatorial Kelvin wave on a meridional boundary, *Journal of Marine Research*, *34*, 295–312, 1976.

Barkley, R. A., Johnston Atoll's wake, *Journal of Marine Research*, *30*, 201–216, 1972.

Barton, I. J., A. J. Prata, and R. P. Cechet, Validation of the ATSR in Australian waters, *Journal of Atmospheric and Oceanic Technology*, *12*, 290–300, 1995.

Battisti, D. S., Dynamics and thermodynamics of a warming event in a coupled tropical atmosphere-ocean model, *Journal of Atmospheric Science*, *45*, 2889–2919, 1988.

Baturin, N. G., and P. P. Niiler, Effects of instability waves in the mixed layer of the equatorial Pacific, *Journal of Geophysical Research*, *102*, 27771–27793, 1997.

Bjerknes, J., Atmospheric teleconnections from the equatorial Pacific, *Monthly Weather Review*, *97*, 163–172, 1969.

Boyer, D. L., and P. A. Davies, Flow past a circular cylinder on a beta-plane, *Philosophical Transactions of the Royal Society of London Series A – Mathematical, Physical and Engineering Sciences*, *306*, 533 *et seq.*, 1982.

Brady, E. C., Observations of wave–mean flow interaction in the Pacific equatorial undercurrent, Ph.D. thesis, Woods Hole Oceanographic Institution, 1990.

Brentnall, S. J., Geostrophic calculations near the equator, Master's thesis, University of Southampton, 1995.

Bretherton, C. S., C. Smith, and J. M. Wallace, An intercomparison of methods for finding coupled patterns in climate data, *Journal of Climate*, *5*, 541–560, 1992.

Bryden, H. L., and E. C. Brady, Diagnostic model of the three-dimensional circulation in the upper equatorial Pacific Ocean, *Journal of Physical Oceanography*, *15*, 1255–1273, 1985.

Cane, M. A., The response of an equatorial ocean to simple wind stress patterns, parts I and II, *Journal of Marine Research*, *37*, 233–299, 1979.

Cane, M. A., and Y. du Penhoat, The effect of islands on low frequency equatorial motions, *Journal of Marine Research*, *40*, 937–962, 1982.

Cane, M. A., and E. S. Sarachik, Forced baroclinic ocean motions. I. the linear equatorial unbounded case, *Journal of Marine Research*, *34*, 629–665, 1976.

Christensen, Jr., N., Observations of the Cromwell Current near the Galapagos Islands, *Deep-Sea Research*, *18*, 27–33, 1971.

Clarke, A. J., On the reflection and transmission of low-frequency energy at the irregular Western Pacific ocean boundary, *Journal of Geophysical Research*, *96*(Supplement), 3289–3305, 1991.

Coward, A. C., P. D. Killworth, and J. R. Blundell, Tests of a two-grid world ocean model, *Journal of Geophysical Research*, *99*, 22725–22735, 1994.

Davis, R. E., Predictability of sea surface temperature and sea level pressure anomalies over the north Pacific Ocean, *Journal of Physical Oceanography*, *6*, 249–266, 1976.

Dijkstra, H. A., and J. D. Neelin, Ocean-atmosphere interaction and the tropical climatology. part II: Why the Pacific Cold Tongue is in the East, *Journal of Climate*, *8*, 1343–1359, 1995.

Drazin, P. G., On the steady flow of a fluid of variable density past an obstacle, *Tellus*, *13*, 239–251, 1961.

Evans, R. H., and H. R. Gordon, Coastal zone color scanner "system calibration": A retrospective examination, *Journal of Geophysical Research*, *99*, 7293–7307, 1994.

Feldman, G., D. Clark, and D. Halpern, Satellite color observations of the phytoplankton distribution in the eastern equatorial Pacific during the 1982–1983 El Niño, *Science*, *226*, 1069–1071, 1984.

Firing, E., et al., Equatorial undercurrent disappears during 1982–83 El Niño, *Science*, *222*, 1121–1123, 1983.

Foster, M. R., Delayed separation in eastward, rotating flow on a beta-plane, *Journal of Fluid Mechanics*, *155*, 59–75, 1985.

Giese, B. S., and D. E. Harrison, Aspects of the Kelvin wave response to episodic wind forcing, *Journal of Geophysical Research*, *95*, 7289–7312, 1990.

Gill, A. E., *Atmosphere-Ocean Dynamics*, Academic Press, 1982.

Godfrey, J. S., A Sverdrup model of the depth-integrated flow for the world ocean allowing for island circulations, *Geophysical and Astrophysical Fluid Dynamics*, *45*, 89–112, 1989.

Godfrey, J. S., The effect of the Indonesian throughflow on ocean circulation and heat exchange with the atmosphere—a review, *Journal of Geophysical Research*, *101*, 12217–12237, 1996.

Halpern, D., Observations of annual and El Niño thermal and flow variations along the equator at 0° 110°W and 0° 95°W during 1980–1985, *Journal of Geophysical Research*, *92*, 8197–8212, 1987.

Halpern, D., et al., Oceanographic observations of the 1982 warming of the tropical eastern Pacific, *Science*, *221*, 1173–1175, 1983.

Haney, R. L., Surface thermal boundary conditions for ocean circulation models, *Journal of Physical Oceanography*, *1*, 241–248, 1972.

Hansen, D., and C. Paul, Genesis and effects of long waves in the equatorial Pacific, *Journal of Geophysical Research*, *89*, 10431–10440, 1984.

Hartten, L. M., Synoptic settings of westerly wind bursts, *Journal of Geophysical Research*, *101*, 16997–17019, 1996.

Hayes, S. P., et al., Hydrographic variability west of the Galápagos Islands during the 1982–83 El Niño, *Progress in Oceanography*, *17*, 137–162, 1986.

Hayes, S. P., et al., TOGA-TAO: a moored array for real-time measurements in the tropical Pacific Ocean, *Bulletin of the American Meteorological Society*, *72*, 339–347, 1991.

Hayes, S. P., and D. Halpern, Correlation of current and sea level in the eastern equatorial Pacific, *Journal of Physical Oceanography*, *14*, 811–824, 1984.

Hendry, R., and C. Wunsch, High Reynolds number flow past an equatorial island, *Journal of Fluid Mechanics*, *58*, 97–114, 1973.

Heywood, K. J., E. D. Barton, and J. H. Simpson, The effects of flow disturbance by an oceanic island, *Journal of Marine Research*, *48*, 55–73, 1990.

Heywood, K. J., D. P. Stevens, and G. R. Bigg, Eddy formation behind the tropical island of Aldabra, *Deep-Sea Research I*, *43*, 555–578, 1996.

Hogg, N. G., Steady flow past an island with applications to Bermuda, *Geophysical Fluid Dynamics*, *4*, 55–81, 1972.

Holton, J. R., *An Introduction to Dynamic Meteorology*, Academic Press, second edition, 1979.

Houvenaghel, G. T., Oceanographic conditions in the Galápagos Archipelago and their relationships with life on the islands, in *Upwelling Ecosystems*, edited by R. Boje, and M. Tomczak, pp. 181–200, Springer, 1978.

Jin, F.-F., Tropical ocean-atmosphere interaction, the Pacific Cold Tongue, and the El Niño–Southern Oscillation, *Science*, *274*, 76–78, 1996.

Jones, J. H., Surfacing of the Pacific equatorial undercurrent: Direct observations, *Science*, *163*, 1449–1450, 1969.

Jones, M. S., M. A. Saunders, and T. H. Guymer, Global remnant cloud contamination in the along-track scanning radiometer—source and removal, *Journal of Geophysical Research*, *101*, 12141–12147, 1996a.

Jones, M. S., M. A. Saunders, and T. H. Guymer, Reducing cloud contamination in ATSR averaged sea-surface temperature data, *Journal of Atmospheric and Oceanic Technology*, *13*, 492–506, 1996b.

Kasahara, A., Various vertical coordinate systems used for numerical weather prediction, *Monthly Weather Review*, *102*, 509–522, 1974.

Kessler, W. S., L. M. Rothstein, and D. Chen, The annual cycle of SST in the eastern Tropical Pacific, diagnosed in an ocean GCM, *Journal of Climate*, *11*, 777–799, 1998.

Kidwell, K. B., *NOAA Polar Orbiter Data User's Guide*, NOAA, Washington, D.C., 1995.

Killworth, P. D., et al., The development of a free surface Bryan-Cox-Semtner ocean model, *Journal of Physical Oceanography*, *21*, 1333–1348, 1991.

Kindle, J. C., and P. A. Phoebus, The ocean response to operational westerly wind bursts during the 1991–1992 El Niño, *Journal of Geophysical Research*, *100*, 4893–4920, 1995.

Knauss, J. A., Measurements of the Cromwell Current, *Deep-Sea Research*, *6*, 265–286, 1960.

Knauss, J. A., Further measurements and observations on the Cromwell Current, *Journal of Marine Research*, *24*, 205–240, 1966.

Kraus, E. B., and J. S. Turner, A one-dimensional model of the seasonal thermocline. II: The general theory and its consequences, *Tellus*, *19*, 98–106, 1967.

Kuo, H. L., Dynamic instability of two-dimensional non-divergent flow in a barotropic atmosphere, *Journal of Meteorology*, *6*, 105–122, 1949.

Lamb, H., *Hydrodynamics*, Dover, 6th edition, 1932.

LeBlond, P. H., and L. A. Mysak, *Waves in the Ocean*, Elsevier, 1978.

Leetmaa, A., et al., Hydrographic conditions in the eastern Pacific before, during and after the 1982/83 El Niño, *Progress in Oceanography*, *19*, 1–47, 1987.

Legeckis, R., Long waves in the eastern equatorial Pacific Ocean, *Science*, *197*, 1179–1181, 1977.

Lu, P., J. P. McCreary, and B. A. Klinger, Meridional circulation cells and the source waters of the Pacific Equatorial Undercurrent, *Journal of Physical Oceanography*, *28*, 62–84, 1998.

Lu, P., and J. P. McCreary, Jr., Influence of the ITCZ on the flow of thermocline water from the subtropical to the equatorial Pacific Ocean, *Journal of Physical Oceanography*, *25*, 3076–3088, 1995.

Lukas, R., The termination of the Equatorial Undercurrent in the eastern Pacific, Ph.D. thesis, University of Hawaii, 1981.

Lukas, R., The termination of the Equatorial Undercurrent in the eastern Pacific, *Progress in Oceanography*, *16*, 63–90, 1986.

Mangum, L. J., S. P. Hayes, and J. M. Toole, Eastern Pacific Ocean circulation near the onset of the 1982–1983 El Niño, *Journal of Geophysical Research*, *91*, 8428–8436, 1986.

Martin, J. H., et al., Testing the Iron Hypothesis in ecosystems of the equatorial Pacific Ocean, *Nature*, *371*, 123–129, 1994.

Mathews, J., and R. L. Walker, *Methods of Mathematical Physics*, Addison-Wesley, 1973.

McCreary, Jr., J. P., and P. Lu, Interaction between the subtropical and equatorial ocean circulations: The subtropical cell, *Journal of Physical Oceanography*, *24*, 466–497, 1994.

McCreary, Jr., J. P., and Z. Yu, Equatorial dynamics in a $2\frac{1}{2}$-layer model, *Progress in Oceanography*, *29*, 61–132, 1992.

McKee, W. D., Comments on "A Rossby wake due to an island in an eastward current", *Journal of Physical Oceanography*, *1*, 287, 1971.

McPhaden, M. J., The Tropical Atmosphere-Ocean array is completed, *Bulletin of the American Meteorological Society*, *76*, 739–741, 1995.

McPhaden, M. J., et al., The response of the equatorial Pacific Ocean to a westerly wind burst in May 1986, *Journal of Geophysical Research*, *93*, 10589–10603, 1988.

Mesinger, F., and A. Arakawa, Numerical methods used in atmospheric models, *GARP Publication 17*, World Meteorological Organisation, Geneva, 1976.

Methven, J., Offline trajectories: Calculation and accuracy, *Tech. Rep. 44*, UK Universities Global Atmospheric Modelling Program, 1997.

Moore, D. W., and S. G. H. Philander, Modelling of the tropical oceanic circulation, in *The Sea*, vol. 6, edited by E. D. Goldberg, et al., pp. 319–361, Wiley (Interscience), New York, 1977.

Munnich, M., and M. Latif, A new theory for tropical instability waves, *Tech. Rep. 268*, Max-Planck-Institut für Meteorologie, Hamburg, 1998.

Murray, J., Sea-surface temperatures from ATSR, CD-ROM, 1995, Rutherford Appleton Laboratory.

Mutlow, C. T., et al., Sea surface temperature measurements by the along-track scanning radiometer on the ERS 1 satellite: Early results, *Journal of Geophysical Research*, *99*, 22575–22588, 1994.

Pak, H., and J. R. V. Zaneveld, The Cromwell Current on the east side of the Galapagos Islands, *Journal of Geophysical Research*, *78*, 7845–7859, 1973.

Palmer, T. N., and D. A. Mansfield, Response of two atmospheric general circulation models to sea surface temperature anomalies in the tropical east and west Pacific, *Nature*, *310*, 483–485, 1984.

Pattiarachi, C., A. James, and M. Collins, Island wakes and headland eddies: A comparison between remotely sensed data and laboratory experiments, *Journal of Geophysical Research*, *92*, 783–794, 1987.

Patzert, W. C., Eddies in Hawaiian waters, *Tech. Rep. HIG–69–8*, Hawaii Institute of Geophysics, 1969.

Philander, G., et al., Long waves in the equatorial Pacific Ocean, *Eos*, *66*, 154–155, 1985.

Philander, S. G. H., Instabilities of zonal equatorial currents. I., *Journal of Geophysical Research*, *81*, 3725–3735, 1976.

Philander, S. G. H., Instabilities of zonal equatorial currents. II., *Journal of Geophysical Research*, *83*, 3679–3682, 1978.

Philander, S. G., *El Niño, La Niña and the Southern Oscillation*, Academic Press, 1990.

Ripa, P., and S. P. Hayes, Evidence for equatorial trapped waves at the Galápagos Islands, *Journal of Geophysical Research*, *86*, 6509–6516, 1981.

Rowlands, P. B., D. L. T. Anderson, and D. W. Moore, The flow of equatorial Kelvin waves and the equatorial undercurrent around islands, *Journal of Marine Research*, *40*, 915–936, 1982.

Salusti, E., and R. Santoleri, A von Kármán wake in the Ligurian Sea, *Bollettino di*

Oceanologia Teorica ed Applicata, *2*, 275–279, 1984.

Schopf, P. S., and M. J. Suarez, Vacillations in a coupled ocean-atmosphere model, *Journal of Atmospheric Science*, *45*, 549–566, 1988.

Schopf, P. S., and M. A. Cane, On equatorial dynamics, mixed layer physics and sea surface temperature, *Journal of Physical Oceanography*, *13*, 917–935, 1983.

Schopf, P. S., and D. E. Harrison, On equatorial waves and El Niño. I: Influence of initial states on wave-induced currents and warming, *Journal of Physical Oceanography*, *13*, 936–948, 1983.

Schott, G., Nachtrag zu dem Aufsatz "Die Grundlagen einer Weltkarte der Meeresströmungen", *Annalen der Hydrographie und Maritimen Meteorologie*, *71*, 282–282, 1943.

Smith, S. C., and H. Whitehead, Variations in the feeding success and behaviour of Galápagos sperm whales (*Physeter macrocephalus*) as they relate to oceanographic conditions, *Canadian Journal of Zoology*, *71*, 1991–1996, 1993.

Steger, J. M., and J. A. Carton, Long waves and eddies in the tropical Atlantic Ocean, *Journal of Geophysical Research*, *96*, 15161–15171, 1991.

Steger, J. M., C. A. Collins, and P. C. Chu, Circulation in the Archipiélago de Colón (Galapagos Islands), November, 1993, *Deep-Sea Research II*, *45*, 1093–1114, 1998.

Stevenson, M. R., and B. A. Taft, New evidence of the Equatorial Undercurrent east of the Galápagos Islands, *Journal of Marine Research*, *29*, 103–115, 1971.

Suarez, M. J., and P. S. Schopf, A delayed action oscillator for ENSO, *Journal of Atmospheric Science*, *45*, 3283–3287, 1988.

Toole, J. M., Near equatorial CTD observations at 85°W in October 1982, *Journal of Geophysical Research*, *90*, 929–933, 1985.

Tritton, D. J., *Physical Fluid Dynamics*, Oxford University Press, second edition, 1988.

Wacongne, S., Dynamical regimes of a fully nonlinear stratified model of the Atlantic equatorial undercurrent, *Journal of Geophysical Research*, *94*, 4801–4815, 1989.

Wajsowicz, R., The circulation of the depth-integrated flow around an island with application to the Indonesian throughflow, *Journal of Physical Oceanography*, *23*, 1470–1484, 1993.

Webb, D. J., An ocean model for array processor computers, *Computers and Geosciences*, *22*, 569–578, 1996.

Webb, D. J., B. A. de Cuevas, and A. C. Coward, The first main run of the OCCAM global circulation model, *Internal Document 34*, Southampton Oceanography Centre, 1998.

Webb, D. J., B. A. de Cuevas, and C. S. Richmond, Improved advection schemes for ocean models, *Journal of Atmospheric and Oceanic Technology*, *15*, 1171–1187, 1998b.

Webb, D. J., et al., A multiprocessor Ocean General Circulation Model using message passing, *Journal of Atmospheric and Oceanic Technology*, *14*, 175–183, 1997.

White, W. B., Reply (to (*McKee*, 1971)), *Journal of Physical Oceanography*, *1*, 288–289, 1971a.

White, W. B., A Rossby wake due to an island in an eastward current, *Journal of Physical Oceanography*, *1*, 161–168, 1971b.

White, W. B., An oceanic wake in the Equatorial Undercurrent downstream from the Galápagos Archipelago, *Journal of Physical Oceanography*, *3*, 156–161, 1973.

Whitehead, A., V. Papastavrou, and S. C. Smith, Feeding success of sperm whales and sea-surface temperature off the Galápagos Islands, *Marine Ecology Progress Series*, *53*, 201–203, 1989.

Wilson, D., and A. Leetmaa, Acoustic Doppler current profiling in the equatorial Pacific in

1984, *Journal of Geophysical Research*, *93*, 13947–13966, 1988.

Woodruff, S. D., et al., A comprehensive ocean-atmosphere data set, *Bulletin of the American Meteorological Society*, *68*, 1239–1250, 1987.

Wyrtki, K., The thermal structure of the eastern Pacific Ocean, *Deutsche Hydrographische Zeitschrift, Erganzungsheft Reihe A No.6*, 1964.

Yamagata, T., K. Mizuno, and Y. Masumoto, Seasonal variations in the equatorial Indian Ocean and their impact on the Lombok throughflow, *Journal of Geophysical Research*, *101*, 12465–12473, 1996.

Yoon, J.-H., Effects of islands on equatorial waves, *Journal of Geophysical Research*, *86*, 10913–10920, 1981.

Yu, Z., J. P. McCreary, and J. A. Proehl, Meridional asymmetry and energetics of Tropical Instability Waves, *Journal of Physical Oceanography*, *25*, 2997–3007, 1995.